Exploring the Mechanism of Buffer Additive Enhanced Electrochemical Performance of Aqueous Zinc-Ion Battery by Integration of Spectroscopic and Non-Spectroscopic Methods

Exploring the Mechanism of Buffer Additive Enhanced Electrochemical Performance of Aqueous Zinc Ion Battery by Integration of Spectroscopic and Non-spectroscopic Methods

By Zeyuan Liu, B. Sc.

A Thesis Submitted to the School of Graduate Studies in Partial Fulfilment of the Requirements for the Degree Master of Science

Lay Abstract

Rechargeable batteries are essential for energy storage and today's life. While today's storage form is mostly lithium-ion batteries. Their limitations are mostly cost, safety and resources. Such limitations have motivated approaches for alternatives, which are aqueous zinc-ion batteries. One of the major challenges is that their manganese dioxide cathodes tend to degrade quickly during repeated charging and discharging. This leads to capacity fading and poor long-term performance.

In this thesis, a low-cost approach for enhancing aqueous zinc ion batteries by adding buffer is explored. Buffers are common agents used to stabilize pH, and here they were investigated as a way to stabilize the chemical environment around the electrode. Through electrochemical tests and supporting characterization methods, buffer effects in enhancing capacity and stability of electrodes is observed. The results suggest that buffer additives can help control the reactions at the electrode surface, though further work is needed to fully understand the mechanisms.

This study highlights a straightforward and inexpensive strategy to enhance aqueous zinc-ion batteries. Such improvements may support the development of safer and more sustainable energy storage systems for large-scale and portable applications.

Abstract

Aqueous zinc-ion batteries (AZIBs) are a promising alternative to lithium-ion systems for grid and portable energy storage due to their low cost, intrinsic safety, and use of abundant materials. Among cathode materials, manganese dioxide (MnO_2) offers high theoretical capacity and affordability, but suffers from rapid capacity fading linked to dissolution and interfacial instability. To address these challenges, this work examines the role of buffer additives (50 mM ammonium dihydrogen phosphate with 5 mM acetic acid) in modifying the electrochemical environment and performance of MnO_2-based cathodes.

Galvanostatic cycling, cyclic voltammetry, and electrochemical impedance spectroscopy (EIS) were employed to compare buffered and unbuffered electrolytes across two commercial electrolytic manganese dioxide samples (EMD-1 and EMD-10). In unbuffered cells, capacity decayed rapidly with cycling, accompanied by the progressive growth of interfacial resistance. In buffered electrolytes, capacity retention improved significantly, with higher coulombic efficiency and smoother long-term cycling trends. Cyclic voltammetry revealed that buffer-containing electrolytes moderated charge–discharge asymmetry, while EIS spectra indicated a shift toward diffusion-dominated behavior at later stages of cycling. Although the precise mechanisms remain to be resolved, these observations suggest that buffers mitigate dissolution and stabilize the local chemical environment, thereby altering the balance between interfacial and transport processes.

Taken together, this thesis demonstrates that a simple buffer additive can enhance the durability of MnO_2 cathodes in AZIBs without compromising the intrinsic advantages of aqueous electrolytes. The findings provide an accessible route to improving the long-term stability of zinc-based batteries and highlight directions for future mechanistic study, including operando characterization and refined electrochemical modeling.

Acknowledgements

To start, I would first like to express my deepest gratitude to my supervisor, Dr. Gillian Goward, for her continuous support, guidance, and patience throughout my studies. Your compassion, warmth, and depth of knowledge have made a lasting impact on me, both academically and personally. I will always remember and value the encouragement and help you have provided during my time here. At this moment and look back, I am grateful that life has guided me to meet Gillian, absolutely no doubt, it was the right path to take, which I would always cherish.

I am also sincerely thankful to my committee members, Dr. Giuseppe Melecini and Dr. Yurij Mozharivskyj, for their support, insights, and valuable contributions.

To the Goward Group members, thank you for your help and camaraderie all the time. I will truly miss the great times spent with E. Magee, A. Quadiri, H. Patel, O. Velenosi, W. Zheng, R. Sahoo, and C. Gurwell. I also extend my appreciation to Dr. Cui and Dr. Pereira.

Special acknowledgement of guidance is due to Dr. Zoya Sadighi and Dr. Kevin Sanders, who have been incredible over the years for advice and guidance. I would also like to thank Dr. Ramesh Sahoo for his assistance in compiling this thesis.

I am grateful to my family for their unwavering support, both financial and emotional. I feel truly blessed to have parents who have always stood by me with encouragement and care. I am also especially fortunate to have my sister, Nicole, who has been by my side since the very beginning of my life. Thanks to my family, I have been able to pursue further and follow my own path without worrying about burden. Their unconditional support over the years has been a constant source of strength, and I feel deeply fortunate to have reached this point because of them.

Finally, I would like to acknowledge the presence of folk outside our lab, such as Huang, Y and with more to add. They are making my life here more enjoyable.

To finish, this is an enjoyable chapter at McMaster, analogous to a rollercoaster—you never quite know what the next step goes. The scary part is not knowing what lies ahead, but the thrilling part is exactly that uncertainty. This experience has taught me to embrace the ride fully, with the simple mindset: go big or go home (sometimes my mom said that too:)

Table of Contents

List of Figures

List of Tables

List of Abbreviations and Symbols

AZIB	Aqueous Zinc Ion Battery
CV	Cyclic voltammetry
EIS	Electrochemical impedance spectroscopy
GCD	Galvanostatic charge discharge
HAc	Acetic acid
LIB	Lithium-ion battery
NHP	Ammonium dihydrogen phosphate
NMR	Nuclear Magnetic Resonance
SEI	Solid-electrolyte interface
SEM	Scanning electron microscopy
T_1IR	T_1 Inversion-Recovery Experiment
XRD	X-Ray Diffraction
γ	Gyromagnetic ratio
τ	NMR signal intensity

Declaration of Academic Achievement

All experimental work presented in this thesis was primarily carried out by the author, unless otherwise noted. Specific contributions from collaborators are acknowledged as follows: the Mn-concentration calibration curve was performed by Kevin Sanders and Breanna Pinto; the unbuffered EMD-10 operando experiment was conducted by Annie Cheng. XRD data collection was carried out with the support of the McMaster X-ray Diffraction Facility, and data interpretation was assisted by Suha Saleem, Charlie Flinn, and Victoria Jarvis. The author especially thanks Taiana Periera for collecting SEM images and providing analysis. EIS equivalent circuit diagram interpretation was made with assistance from Dr. Ramesh Sahoo.

Chapter 1: Background and Introduction

1. Introduction

1.1. Motivation for research

The energy innovations created an electrified world, reshaping the way we work, commute and communicate. Today, everything in our daily life relies on electricity—from browsing smartphones to operating machinery and household appliances. While the production and transmission of electricity have become efficient and widespread, the challenge of storing extra electricity and releasing it during peak hours remains one of the hardest questions in electricity systems.

An invention to store electricity within small devices came in 1991 when SONY first commercialized rechargeable lithium-ion batteries (LIBs). That was a significant milestone in energy storage where a lightweight and compact device made it possible to store and release electricity whenever and wherever needed. Since then, LIBs have become dominant in portable energy storage.[15] Their popularity in electronics—like smartphones, laptops, and wearable devices—is made possible by three key factors: high energy density, long cycle life, and versatile forms. Over the years, LIB applications have expanded into electric mobility and industrial sectors, powering electric vehicles (EVs), hybrid cars, and small-scale backup systems.[15] [4]

However, despite their advantages and widespread use, LIBs have considerably expensive and have environmental impacts in production and recycling. Their production is highly resource-intensive and energy-consuming, relying on mining critical minerals such as lithium, cobalt and copper in nature. This mining is always connected with pollution, water contamination and emissions.[16] In factory production, considerable industrial waste is

generated. By estimate, for each kWh battery produced, 50~80 kg of greenhouse gases is emitted, not including mining emissions.[16] In the end of their service life, a mature recycling industry is not yet ready, resulting unprocessed waste and long-term environmental burden.

The increased demand for consumer electronics and the widespread adoption of electrified vehicles have aggregated the need for electricity production and storage. According to the International Energy Agency, almost 18 million electrified vehicles were sold globally in 2024 alone.[12] It is nearly tenfold increase from 2 million in 2018.[4] This rising demand illustrated a global trend toward electrification in transportation, industry, and residential sectors. As electricity use rises, grid stability becomes increasingly reliant on effective energy storage systems that can balance time and geographical mismatches between generation and demand.

In reality, electricity production is often constrained by geographic and temporal factors. Green energy sources—such as solar and wind—are inherently intermittent, while hydroelectricity—despite its reliability to produce electricity 24/7—can be limited by geography and seasonal weather changes. According to the International Energy Agency (IEA), more than half of Canada's electricity is generated from hydroelectric dams, contributing to the total of 600 gigawatt-hours (GWh) nationally. From this electricity generated, over half of it is used by transportation systems and industrial operations.[11] Given the nature of instability of hydroelectricity, it may not always match consumption side under seasonal changes. This disparity makes energy storage and transport systems crucial for grid resilience and long-term energy security.

Traditionally, electricity storage is achieved via conversion of electrical energy to other sources of energy such as potential energy. One of the examples in this storage is pumped hydro. Electricity is used to pump water to higher levels during periods of surplus, while releasing the water to generate power during period of high demand. While being effective, these systems are highly dependent on favorable geological conditions and large-scale infrastructure such as dam, which may not be available in all regions at all times.[17] Additionally, they can result in significant environmental disruptions, including flooding and land use conflicts. In contrast, battery storage offers a compact and efficient alternative that can be implemented in multiple settings. Their high capacity could enable storing electricity in a large scale; however, lithium-ion batteries are increasingly seen as impractical for large-scale electricity storage. This resulted from their cost, safety concerns, and vulnerability to operating conditions.

Financially speaking, storing one kilowatt-hour (kWh) of electricity using LIBs can cost up to US$ 300, an unaffordable expense when scaled to the national grid.[8] Safety risks, such as thermal runaway and fire hazards—further complicate their application in dense storage settings. The operating conditions require a well-ventilated area with proper temperature control, meaning such facilities will cause a burden on infrastructure. An uncontrolled working environment would also lead to danger such as fire hazards, or even more serious, explosion. These issues underscore the urgent need for alternative energy storage technologies that are cost-effective, environmentally sustainable, and technically scalable.

In response to challenges in energy storage, researchers are turning their attention to next-generation technologies designed to meet the demands of a rapidly electrifying world.

Conventional lithium-ion batteries (LIBs), while dominant in portable devices and electric vehicles, are encountering practical and environmental constraints when scaled for grid-level applications. These challenges have catalyzed interest in alternative systems such as flow batteries, solid-state batteries, and various hybrid configurations, each offering distinct advantages in terms of safety, scalability, and environmental impact.[2]

Flow batteries, for example, allow decoupling of energy and power ratings by storing electrolytes externally, making them promise for stationary energy storage. Solid-state batteries aim to eliminate flammable liquid electrolytes and improve energy density through novel materials.[17] Concurrently, innovations in materials science, including the discovery and optimization of earth-abundant elements, are reshaping the landscape of electrochemical energy storage

To be practically viable for grid-scale deployment, a modern energy storage system must satisfy several criteria. It must demonstrate exceptional safety to mitigate fire hazards and thermal runaway risks typically seen in batteries, possess a simplest design to ensure ease of manufacturing and maintenance, while enabling seamless scalability without imposing a significant ecological burden. In this context, aqueous zinc-ion battery (AZIB) technology has gained substantial interest due to its attractive electrochemical properties and alignment with sustainability goals.[7] Aqueous zinc-ion batteries operate using zinc as the anode and a water-based electrolyte, significantly reducing flammability concerns associated with organic solvents in LIBs. Zinc is abundant, inexpensive, and environmentally clean compared to lithium or cobalt, making it an ideal candidate for large-scale stationary storage systems. A more detailed discussion is presented in the following sections.[3]

In summary, while lithium-ion batteries have undoubtedly revolutionized portable power applications, their limitations become increasingly pronounced at the scale required for grid stabilization and large-scale energy dispatch. Issues such as resource scarcity, high cost, and safety risks present formidable barriers to LIB-based systems in supporting future energy infrastructure. As global electrification accelerates—with rising electricity demand across residential, industrial, and transportation sectors, it is imperative to identify and implement energy storage solutions that are both technologically robust and environmentally sustainable. Aqueous zinc-ion batteries emerge as a compelling alternative in this context, offering a promising route toward energy equity, economic viability, and climate resilience.

1.2. Zinc-Ion Batteries

Zinc-ion batteries (ZIBs), a class of aqueous rechargeable batteries, have emerged within the past 10 years as an attractive alternative due to their intrinsic safety, environmental compatibility, and low manufacturing costs. ZIBs share a similar structural design with LIBs: an anode, a cathode, a separator, and conductive electrolytes in between. While the overall cell architecture resembles LIB technology, the chemistry within ZIBs is fundamentally different in both behavior and implications. Instead of lithium ions migrating between hosts in an organic electrolyte, zinc ions shuttle through an aqueous medium—drastically reducing the risks associated with flammable components and thermal runaway. A comparison of the two systems is shown in Figure 1.

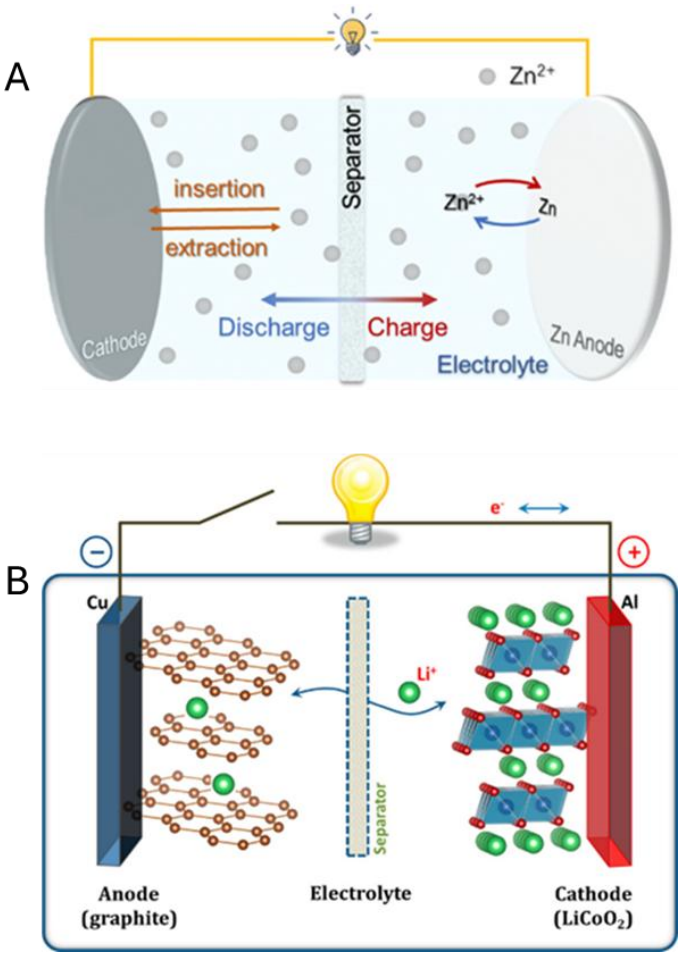

Figure 1. A comparison of ZIB with its counterparts LIB. A: Schematic illustration of general ZIB assembly. Reprinted with permission from J. Mater. Chem. A 2023, 11, 11987–12001. Copyright © The Royal Society of Chemistry 2023. B. Schematic illustration of the first Li-ion battery. Reprinted with permission form J. Am. Chem. Society, 2013, 135, 1167 – 1176. Copyright © 2013, American Chemical Society.

This transition from lithium to zinc-based electrochemistry is not simply a shift in elemental choice, but a strategic rethinking of energy storage for stationary applications. Zinc, as a post-transition metal with stable electrochemical properties, is both chemically favorable and environmentally available. It exhibits a redox potential (1.1-1.8 V) suitable for aqueous media, enabling efficient and reversible plating/stripping reactions—core to charge and discharge processes.[9] Importantly, zinc-based chemistries support high

volumetric capacity and are naturally resilient to air and moisture, unlike lithium, which requires a highly controlled environment (air and moisture) preventing reactivity and degradation.[13]

Economically speaking, zinc beats lithium by a wide margin. As a naturally abundant element, zinc is mined and refined with significantly lower energy input, while mineral ores are globally available. Its global production surpassed lithium by nearly two orders of magnitude, and the market is relatively controlled due to diverse supply sources. In monetary terms, refined zinc costs approximately U$ 3,000 per metric ton, while lithium carbonate and its analogs—commonly used in LIB production—could exceed U$ 46,000 per metric ton.[20] This dramatic cost disparity reflects directly in the actual cost of energy storage: grid-scale ZIBs are estimated to store electricity at less than $150 per kWh, compared to more than $350 per kWh for analogous LIB systems.[8]

Aqueous electrolytes play a crucial role in the environmental and operational advantages of ZIBs. Unlike LIBs, which rely on organic solvents such as ethylene carbonate and diethyl carbonate, flammable, hazardous and extremely toxic. AZIBs operate within water-based solutions. Water, being non-toxic, non-flammable, and widely available, greatly simplifies system design and safety protocols, while enhancing workers' safety in production at minimal costs.[13] Electrolyte stability at ambient temperatures allows for passive thermal management, reducing infrastructure demand and enhancing deployment flexibility. In addition, aqueous systems bear high ionic conductivity comparable to LIBs, while eliminating most risks associated with organic solvents, enabling simplified treatment and recycling at their end-of-life.

Beyond material advantages, AZIBs show promising electrochemical performance. Zinc metal anodes enable high theoretical capacities (820 mAh/g) and excellent reversibility,[13] while cathode materials such as manganese dioxide, vanadium oxides, or Prussian blue analogs offer tunable morphologies and intercalation kinetics.[1] Recent developments in surface engineering—such as coatings that suppress dendrite formation or nanostructured composites—have helped address common challenges in zinc-based systems, extending cycle life and improving Coulombic efficiency.

Furthermore, AZIBs are particularly well-suited for modular and scalable designs in grid applications. Their inherent safety profile allows dense packing without sophisticated systems, and their compatibility with ambient-pressure manufacturing reduces costs across fabrication, transport, and installation. The aqueous nature of the system minimizes environmental risks during operation and disposal, enabling a more circular lifecycle compared to the disposal-sensitive architecture of LIBs.

In broader energy systems modeling, ZIBs offer stability and adaptability that match real-world usage profiles. They can be tuned for high-rate discharge in peak shaving, or long-duration storage across intermittent renewables. Their resilience to hot climates and low infrastructure requirements positions them as viable solutions for both dense urban grids and remote microgrid systems.

In summary, zinc-ion batteries represent a scientifically and strategically sound alternative to conventional lithium-ion technology for stationary energy storage. Their favorable materials profile, operational safety, and cost-efficiency reflect a new design paradigm that aligns with the needs of sustainable energy infrastructure. As deployment scales and

ongoing research addresses performance bottlenecks, AZIBs are poised to play a defining role in next-generation energy storage ecosystems.

1.3. Cathode and Anode Materials

Aqueous zinc-ion batteries (AZIBs) offer an affordable alternative to conventional lithium-ion systems, particularly for stationary energy storage where safety, cost efficiency, and sustainability matter most.

The anode in AZIBs is typically metallic zinc, selected for its low redox potential, high theoretical capacity (820 mAh/g), and favorable kinetics for aqueous systems. In aqueous systems, zinc ions reversibly plate and strip from the anode under ambient conditions during cycling.[7] [9] [1]

Despite these benefits, challenges exist. Dendrite growth, inhomogeneous zinc deposition, formation of passivation layers, and hydrogen evolution reactions can limit anode performance. [13] To address these issues, various strategies have been developed, including surface treatments, zinc alloying, substrate texturing, atomic layer deposition, and the use of electrolyte additives. These approaches have shown promise in improving zinc utilization, coulombic efficiency, and cycle life.

In aqueous systems with metal zinc anodes, the energy storage mechanism on the cathode side can generally be categorized into three types[13] : (1) zinc-ion intercalation, (2) water/H^+ co-insertion or extraction, and (3) conversion reactions. In the first mechanism, energy is stored via direct Zn^{2+} intercalation into cathode structures. The second and third involve additional side reactions, such as proton insertion or irreversible phase transformations. These mechanisms are schematically illustrated in Figure 2 and form the basis for evaluating cathode material performance.

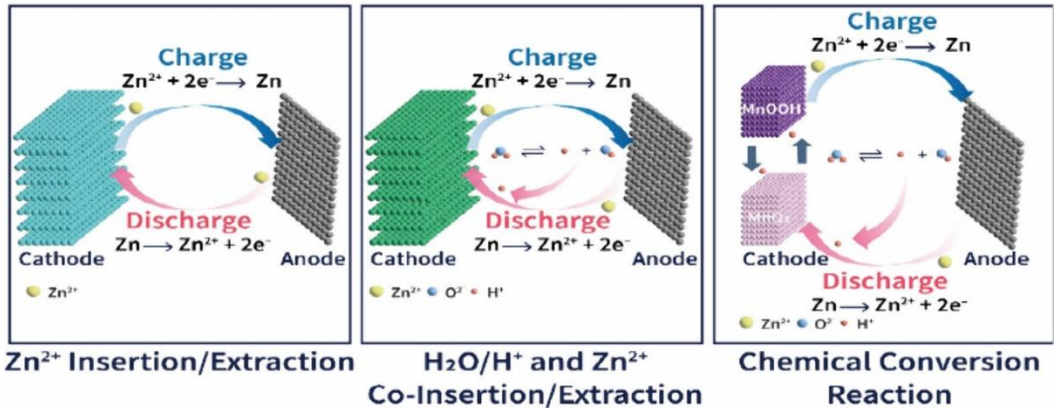

Figure 2 Explanation of reaction mechanisms in AZIB, illustrating three different pathways zinc ions reacts. Reprinted from ACS Appl. Energy Mater. 2025, 8, 11, 6806–6828 with permission. Copyright © 2025 American Chemical Society.

The selection of cathode materials is central in determining the performance and durability of AZIBs. Among the various candidates, transition metal oxides—such as vanadium oxides (e.g., V_2O_5), iron oxides (Fe_3O_4), and manganese oxides (MnO_2)—have received significant attention due to their natural abundance, structural stability, and favorable electrochemical characteristics. Additionally, metal-organic frameworks (MOFs) have been explored for their porous architectures and tunable redox properties.[1] [13]

These inorganic materials are particularly attractive because of their tunnel or layered structures, which facilitate the reversible intercalation of zinc ions. Their unique geometries support fast ion transport, high structural integrity, and good electrochemical reversibility. They work effectively within the narrow working voltage window of AZIBs, though specific capacities vary widely depending on composition and crystal phase, as shown in Figure 3 and Figure 4.

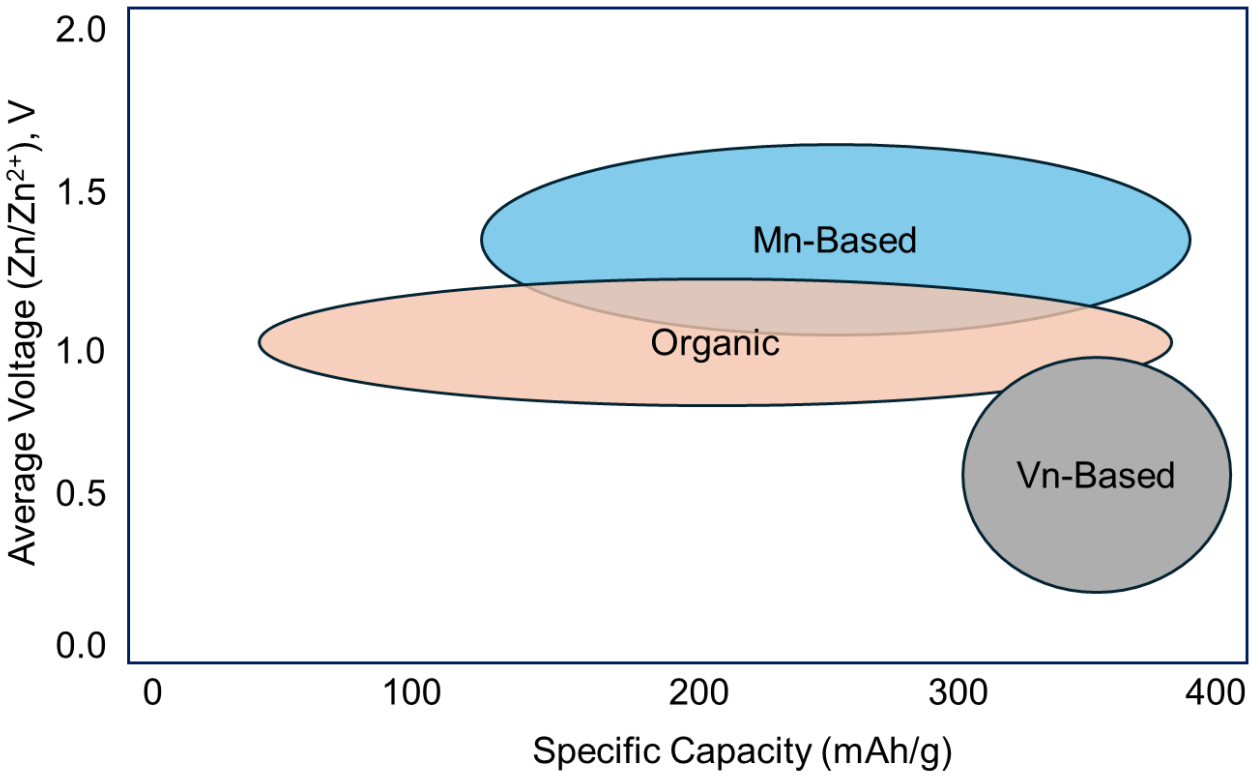

Figure 3 Illustration of various class of inorganic complexes and their capacities. Figure adapted and redrawn from ACS Appl. Energy Mater. 2025, 8, 11, 6806–6828 with permission. Copyright © 2025 American Chemical Society.

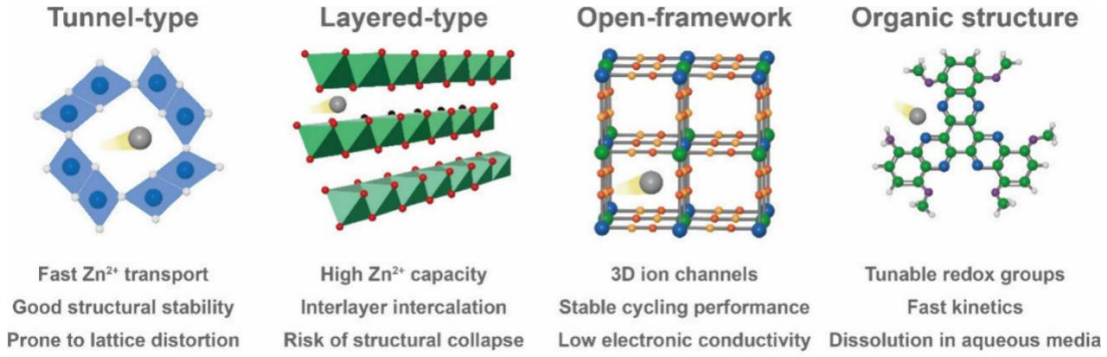

Figure 4. Illustration of different structures in the materials. Each structure is unique that are contributing to AZIB performance. Reprinted from ACS Appl. Energy Mater. 2025, 8, 11, 6806–6828 with permission. Copyright © 2025 American Chemical Society.

Among them, manganese dioxide (MnO_2) stands out as a leading material for grid-scale applications. It is not only cost-effective and environmentally benign, but also readily available through scalable industrial processes. MnO_2 naturally exists in multiple

polymorphs—α, β, γ, and δ (shown in Figure *5*), each with distinct crystal structures that influence zinc ion diffusion pathways. Additionally, synthesis methods such as electrolytic deposition and chemical precipitation affect the morphology and particle size of MnO_2, often ranging from 1 to 100 μm. While such physical variations do not alter the material's chemical structure and nature, they can influence surface area, conductivity, and reaction kinetics.

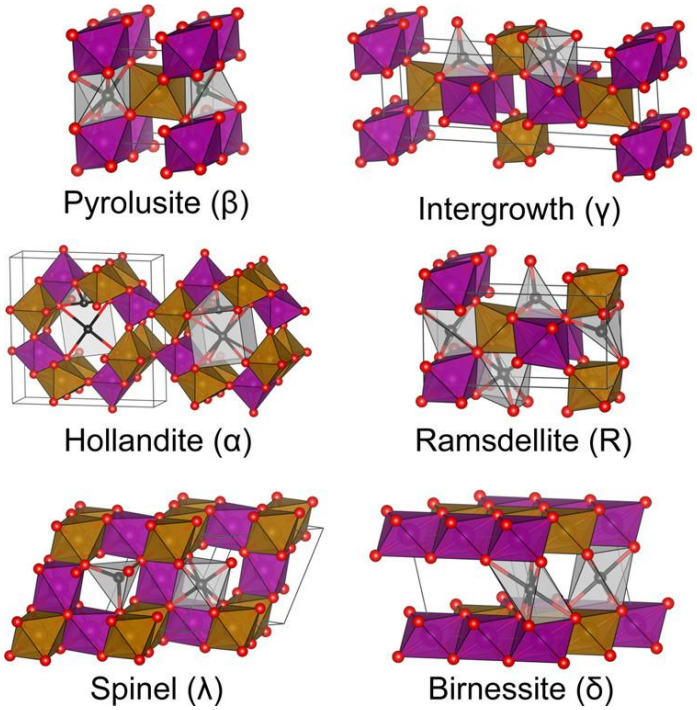

Figure 5 Various phases of manganese dioxide explained, adapted from J. Am. Chem. Soc. 2017, 139, 7, 2672–2681, reprinted with permission, Copyright © 2017 American Chemical Society

An important advantage of Mn-based cathodes is their low toxicity, which reduces the danger to humans at production stage and environmental impact at the end of battery life. Minimal post-treatment requirements make them attractive for sustainable energy systems.[18] [22] Taken together, MnO_2 combines structural suitability, environmental safety, and industrial viability—making it a strong candidate for large-scale energy storage despite ongoing limitations in cycling stability.

Despite their many advantages, inorganic cathodes—particularly transition metal oxides are having limitations. Structural degradation and by-product formation during cycling remain major challenges to long-term performance.[13] For example, in mildly acidic aqueous electrolytes, vanadium oxides are prone to dissolution and rapid capacity fading. Similarly, MnO_2 suffers from capacity loss due to Mn^{3+}-induced Jahn–Teller distortion and gradual manganese dissolution, especially under extended uses.[14] These degradation pathways compromise both energy density and lifespan and can contribute to issues such as zinc dendrite formation.

In response to these challenges, organic cathode materials have emerged as a promising alternative. Unlike metal-based systems, organic materials function through redox-active molecular centers, offering a distinct electrochemical pathway.[13] A wide range of organic compounds—including quinones, imines, and conjugated polymers—have been studied for their ability to reversibly coordinate with zinc ions through functional groups such as carbonyl (C=O) or imine (C=N) bonds.[10]

One of the most significant advantages of organic cathodes is their inherently low solubility in aqueous media. This minimizes the loss of active material during cycling and helps maintain structural integrity. However, their application in grid-scale energy systems is more limited than their inorganic counterparts. Organic cathodes often suffer from relatively low practical capacities, poor performance, and limited cycling life.[10] [13] Moreover, the cost of synthetic organic materials remains higher than that of naturally occurring inorganic minerals, although ongoing advancements in molecular design and scalable synthesis may gradually mitigate these concerns.

In conclusion, both inorganic and organic cathode materials bring unique strengths and inherent trade-offs to the development of AZIB. Inorganic oxides, particularly MnO_2, offer excellent structural stability, low cost, and proven scalability, but face challenges related to degradation and capacity retention. Organic materials, by contrast, exhibit promising electrochemical tunability and cycling stability due to their molecular design flexibility and low solubility, yet remain constrained by cost, energy density, and immature manufacturing processes.

A holistic approach that balances performance, safety, cost, and sustainability is therefore essential. Continued research into material innovation, structural engineering, and electrolyte optimization may help bridge the performance gap between these two classes. Ultimately, the advancement of cathode materials, both inorganic and organic, will be critical to realizing the full potential of AZIBs as a next-generation energy storage solution for a carbon-neutral future.

1.4. Challenges and Improvements

As discussed in Section 1.3, challenges in AZIBs exist across the entire electrochemical system—from the anode and cathode to the electrolyte or interface after extended cycling.[13] Structural distortions in cathode materials and irregular zinc deposition or dendrite formation at the anode can result in premature cell failure. Additionally, the decomposition of aqueous electrolytes—often due to hydrogen and oxygen evolution reactions—may compromise cell safety and, in some cases, lead to pressure build-up or explosion. In response, researchers have developed integrated strategies to mitigate these issues, including anode surface engineering to suppress dendrite growth and passivation

layer formation, and cathode stabilization techniques aimed at preserving structural integrity.

Among the various cathode materials explored for AZIBs, manganese dioxide (MnO_2) stands out as the most commercially feasible due to its abundance, low cost, environmental friendliness, and industrial scalability. Its multiple polymorphs and favorable electrochemical behavior make it particularly attractive for grid-scale applications. However, despite its advantages, MnO_2-based cathodes still face unresolved challenges that are under-addressed in the current literature. Notably, cycling stability remains a primary bottleneck, largely driven by dissolution of Mn^{3+} species and structural distortion via the Jahn–Teller effect, as explained in Figure 6. While studies have proposed surface coatings or electrolyte additives as mitigation strategies, many focus on short-term performance or rely on non-scalable methods such as excess Mn^{2+} supplementation.[13] [19] Furthermore, the scalability of MnO_2 synthesis methods—with regard to cost, uniform morphology control, and phase purity—requires deeper exploration to enable real-world deployment. Addressing these gaps is critical for MnO_2 to transition from a promising laboratory material to a reliable industrial solution in energy storage.

In practice, we hypothesize that the persistent solubility of Mn^{2+} in aqueous zinc-ion batteries arises from stability of Mn^{2+} and the instability of Mn (III) intermediates. Once electrochemical reduction forms Mn (III) oxyhydroxide, it undergoes disproportionation to Mn (IV) and Mn^{2+}. The Mn^{2+} ion is thermodynamically favored in aqueous solution across acidic to near-neutral pH and remains stable over a wide electrochemical window, as shown in manganese Pourbaix diagrams. In addition, the relatively high hydration energy of Mn^{2+} and its ability to coordinate with common anions (e.g., sulfate, acetate,

triflate) promote its persistence as a soluble species, rather than reprecipitating as $Mn(OH)_2$ under typical electrolyte conditions. Therefore, the dissolution pathway is not only initiated by disproportionation but also maintained by the aqueous speciation and stability of Mn^{2+}, which explains why Mn loss from the cathode a nearly universal phenomenon in Mn-based zinc batteries. The detailed process is described in Equation 1 and Equation 2.

$$MnO_2(s) + H^+ + e^- \leftrightarrow MnOOH\ (s)$$

Equation 1 Electrochemical reduction of Mn (IV) to Mn (III) during the discharge of MnO_2 cathodes in aqueous Zn-ion batteries.

$$2MnOOH(s) \rightarrow MnO_2(s) + Mn^{2+}(aq) + 2OH^-$$

Equation 2 Chemical disproportionation of Mn(III) oxyhydroxide, leading to partial regeneration of MnO_2 and dissolution of Mn^{2+} into the electrolyte.

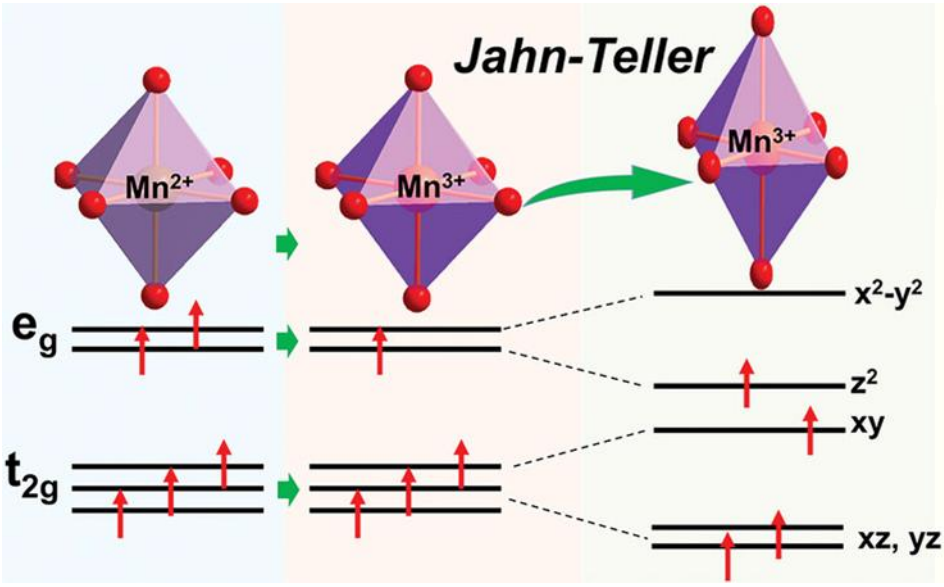

Figure 6 Schematic of Mn redox and Jahn–Teller distortion in MnO_2. Upon reduction from Mn^{4+} to Mn^{3+}, elongation of Mn–O bonds occur due to Jahn–Teller distortion. The accumulated strain

makes Mn^{3+} unstable and prone to disproportionation into Mn^{2+} and Mn^{4+}. The Mn^{2+} species readily dissolve into the aqueous electrolyte, leading to active material loss and phase transitions, which accelerate capacity fading. Figure adapted from Adv. Funct. Mater. 2023, Vol 34, 4, 2310057.

In comparison, organic material derived cathodes—while offering molecular tunability by functional group modification and cycling resilience—remain limited by their cost, complex synthesis, and relatively low energy density, making them less practical for commercialization.

The dissolution of manganese can be directly observed *in situ* using spectroscopic techniques. Among them, nuclear magnetic resonance (NMR) spectroscopy offers valuable insight into the behavior of Mn^{2+} ions during electrochemical cycling for the first time ever. Due to the paramagnetic nature of Mn^{2+}, its presence alters the spin-lattice relaxation times of nearby solvent protons, namely, water.[6] The detailed methodology is described in Chapter 2. This capability makes Mn-based systems particularly well-suited for mechanistic studies of degradation pathways. By enabling real-time monitoring of electrolyte composition, NMR provides critical information that supports the development of strategies to mitigate dissolution-related failure. One of the most promising approaches, informed by these insights, involves targeted electrolyte design. Given that AZIB operation is highly dependent on aqueous conditions, even minor perturbations—such as shifts in pH or changes in ionic strength—can lead to systematic changes in performance. In this context, electrolyte modification offers a practical and scalable route for improving battery stability.

Electrolyte engineering has thus emerged as a cost-effective and efficient strategy to enhance AZIB performance while maintaining chemical and electrochemical compatibility. Beyond conventional electrochemical testing, electrolyte formulations

should also be assessed with complementary tools such as in situ XRD to follow phase transitions, operando NMR to monitor Mn dissolution, and spectroscopic probes to examine Zn^{2+} solvation and interphase stability. Such multi-faceted evaluation can more directly connect electrolyte chemistry with cycling behavior and long-term performance. While alternatives such as viscous or polymer-based electrolytes can suppress side reactions and gas evolution, they often introduce higher complexity and cost. A more accessible approach is the use of electrolyte additives—particularly buffering agents—since the redox behavior and stability of Mn-based electrodes are strongly influenced by pH.[21] Even slight deviations in acidity can trigger dramatic shifts in dissolution rate, redox kinetics, or side reaction pathways, for example, in a complete cell with Zn and MnO_2 the possible species exist could be illustrated by the Pourbaix diagram in Figure 7.

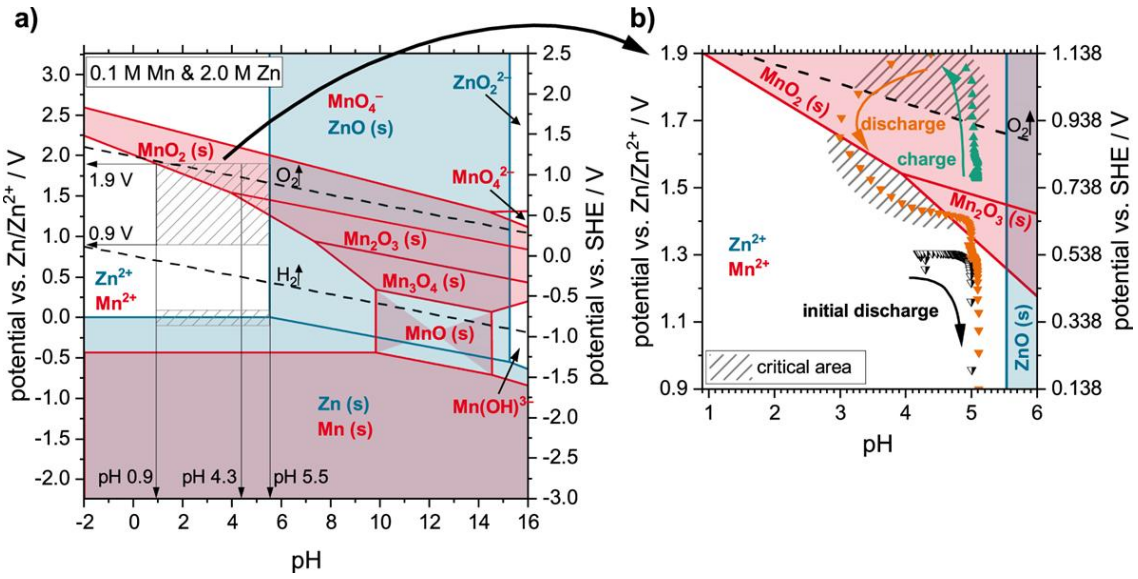

Figure 7 Pourbaix diagram of Zn/Mn system in a typical aqueous zinc ion cell. Given various voltage and pH the favored species could be determined. Panel A indicated a full scale of voltage vs pH while panel B shows enlarged view in the critical region where AZIB system mostly works. Figure reproduced from: Bischoff, C. F.; Fitz, O. S.; Burns, J.; Bauer, M.; Gentischer, H.; Birke, K. P.; Henning, H.-M.; Biro, D. J. Electrochem. Soc. 2020, 167 (2), 020545. Reproduced under the terms of the Creative Commons CC BY-NC-ND 4.0 license. No modifications were made.

Buffering systems, typically consisting of a weak acid and its conjugate base, regulate pH by neutralizing additional acid or base during cycling. Buffers function by (1) releasing protons (H^+) when the pH rises and (2) consuming protons when the pH drops, thereby stabilizing the electrolyte environment. [21] Appropriate buffer selection allows for control over the pH near electrode surfaces, helping maintain operation within a desirable electrochemical window. Buffering agents commonly explored in aqueous AZIBs include phosphate, acetate, and ammonium-based systems.[5] By tuning buffer composition and concentration, the electrolyte can be optimized to suppress Mn dissolution and improve long-term cycling performance.

However, many published studies rely on the addition of excess Mn^{2+} salts, such as manganese sulfate ($MnSO_4$), to artificially suppress further Mn dissolution during testing.[19] While this approach may improve apparent stability, it deviates significantly from real-world applications, where adding large concentrations of metal salts is impractical and potentially detrimental. Spiked Mn ions can alter the electrolyte composition while redeposition of these Mn-species back to cathode during discharge may be uncontrolled, causing phase deviation than desired. This method introduces variables that complicate scalability and regulatory compliance for grid-scale energy storage.

Based on buffer chemistry and insights from recent literature, this study adopts a phosphate-based buffer system with added acetic acid to investigate the effectiveness of pH control in the absence of external Mn^{2+} supplementation.[5] [23] The goal is to simulate native conditions and evaluate how intrinsic buffering strategies can preserve cathode integrity and sustain long-term performance. Specifically, the electrolyte used in this work

consists of ammonium dihydrogen phosphate (NHP) with 5 mM acetic acid. Full details of the formulation and experimental procedures are provided in Chapter 2.

1.5. Thesis Outline

This thesis is composed of five chapters. Chapter 1 introduces the background, motivation, and objectives of the study, providing the overall context for the development of aqueous zinc-ion batteries and the importance of Mn-based cathodes. Chapter 2 describes the experimental methodologies and underlying theoretical principles used in this work, including electrode fabrication, electrochemical testing, and materials characterization. Chapter 3 presents the major experimental observations regarding the influence of buffer additives on electrochemical performance, highlighting the differences between buffered and unbuffered systems. Chapter 4 focuses on mechanistic interpretation, where detailed analyses are conducted to identify the origins of the observed phenomena and to evaluate the contributing factors to degradation and stabilization processes. Finally, Chapter 5 concludes the thesis by summarizing the principal findings and discussing their implications, while also proposing directions for future research in electrolyte engineering and diagnostic strategies for aqueous zinc-ion batteries.

1.6. References

[1] Ajay Rakkesh, R.; Shalini, S.; Tharani, S.; Durgalakshmi, D.; Balakumar, S. Possibilities and Challenges of Cathode Materials for Zn-Ion Batteries. *Energy Advances* **2024**, *3* (4), 676–688.

[2] Alsym Energy. *Non Lithium Battery Alternatives* [Blog]; Alsym Energy: [Location if known, e.g., San Diego, CA], August 3, 2023. https://www.alsym.com/blog/alternatives-to-lithium-batteries/ (accessed August 31, 2025).

[3] Anqi Guo, Zhenghao Wang, Liang Chen, Weizao Liu, Kailong Zhang, Liping Cao, Bin Liang, and Dongmei Luo. A Comprehensive Review of the Mechanism and Modification Strategies of V2O5 Cathodes for Aqueous Zinc-Ion Batteries. *ACS Nano* 2024 18 (40), 27261-27286

[4] Balali, Y.; Stegen, S. Review of Energy Storage Systems for Vehicles Based on Technology, Environmental Impacts, and Costs. *Renewable and Sustainable Energy Reviews* **2020**, *135*, 110185.
[5] Bischoff, C. F.; Fitz, O. S.; Burns, J.; Bauer, M.; Gentischer, H.; Birke, K. P.; Henning, H.-M.; Biro, D. Revealing the Local Ph Value Changes of Acidic Aqueous Zinc Ion Batteries with a Manganese Dioxide Electrode during Cycling. *Journal of The Electrochemical Society* **2020**, *167* (2), 020545.
[6] Britton, M. M. Measurement of the Concentration of Mn2+and Mn3+in the Manganese-Catalyzed 1,4-Cyclohexanedione−acid−bromate Reaction Using Redox-Triggered Magnetic Resonance Spectroscopy. *The Journal of Physical Chemistry A* **2006**, *110* (49), 13209–13214.
[7] Fang, G.; Zhou, J.; Pan, A.; Liang, S. Recent Advances in Aqueous Zinc-Ion Batteries. *ACS Energy Letters* **2018**, *3* (10), 2480–2501.
[8] Gourley, S.; Higgins, D. *Analysis: How zinc-ion batteries may solve our renewable energy storage problem*. Brighter World-McMaster University September 13, 2023.
[9] Guo, X.; He, G. Opportunities and Challenges of Zinc Anodes in Rechargeable Aqueous Batteries. *Journal of Materials Chemistry A* **2023**, *11* (23), 11987–12001.
[10] Huang, L.; Li, J.; Wang, J.; Lv, H.; Liu, Y.; Peng, B.; Chen, L.; Guo, W.; Wang, G.; Gu, T. Organic Compound as a Cathode for Aqueous Zinc-Ion Batteries with Improved Electrochemical Performance via Multiple Active Centers. *ACS Applied Energy Materials* **2022**, *5* (12), 15780–15787.
[11] IEA (2022), Canada 2022, IEA, Paris https://www.iea.org/reports/canada-2022, Licence: CC BY 4.0
[12] IEA (2025), Global EV Outlook 2025, IEA, Paris
[13] Kim, A.; Park, Y.; Choi, J.; Yu, S.-H.; Nam, K. W. A Comprehensive Review of Cathode Materials for Advanced Aqueous Zinc-Ion Batteries. *ACS Applied Energy Materials* **2025**, *8* (11), 6806–6828.
[14] Kitchaev, D. A.; Dacek, S. T.; Sun, W.; Ceder, G. Thermodynamics of Phase Selection in Mno2 Framework Structures through Alkali Intercalation and Hydration. *Journal of the American Chemical Society* **2017**, *139* (7), 2672–2681.
[15] Li, J.; Fleetwood, J.; Hawley, W. B.; Kays, W. From Materials to Cell: State-of-the-Art and Prospective Technologies for Lithium-Ion Battery Electrode Processing. Chemical Reviews 2021, 122 (1), 903–956.
[16] Llamas-Orozco, J. A.; Meng, F.; Walker, G. S.; Abdul-Manan, A. F.; MacLean, H. L.; Posen, I. D.; McKechnie, J. Estimating the Environmental Impacts of Global Lithium-Ion Battery Supply Chain: A Temporal, Geographical, and Technological Perspective. *PNAS Nexus* **2023**, *2* (11).
[17] Mitali, J.; Dhinakaran, S.; Mohamad, A. A. Energy Storage Systems: A Review. *Energy Storage and Saving* **2022**, *1* (3), 166–216.
[18] Pan, H.; Shao, Y.; Yan, P.; Cheng, Y.; Han, K. S.; Nie, Z.; Wang, C.; Yang, J.; Li, X.; Bhattacharya, P.; Mueller, K. T.; Liu, J. Reversible Aqueous Zinc/Manganese Oxide Energy Storage from Conversion Reactions. *Nature Energy* **2016**, *1* (5).

[19] Qiu, C.; Zhu, X.; Xue, L.; Ni, M.; Zhao, Y.; Liu, B.; Xia, H. The Function of Mn2+ Additive in Aqueous Electrolyte for Zn/δ-MnO2 Battery. *Electrochimica Acta* **2020**, *351*, 136445.

[20] **U.S. Geological Survey.** *Mineral Commodity Summaries*; U.S. Department of the Interior: Washington, DC, January 2024.

[21] Zhang, D.; Miao, L.; Song, Z.; Zheng, X.; Lv, Y.; Gan, L.; Liu, M. Electrolyte Additive Strategies for Safe and High-Performance Aqueous Zinc-Ion Batteries: A Mini-Review. *Energy & Fuels* **2024**, *38* (14), 12510–12527.

[22] Zhang, N.; Cheng, F.; Liu, J.; Wang, L.; Long, X.; Liu, X.; Li, F.; Chen, J. Rechargeable Aqueous Zinc-Manganese Dioxide Batteries with High Energy and Power Densities. *Nature Communications* **2017**, *8* (1).

[23] Zhang, W.; Dai, Y.; Chen, R.; Xu, Z.; Li, J.; Zong, W.; Li, H.; Li, Z.; Zhang, Z.; Zhu, J.; Guo, F.; Gao, X.; Du, Z.; Chen, J.; Wang, T.; He, G.; Parkin, I. P. Highly Reversible Zinc Metal Anode in a Dilute Aqueous Electrolyte Enabled by a pH Buffer Additive. *Angew. Chem., Int. Ed.* **2022**, *62* (5), e202212695.

Chapter 2: Experimental Details and Theories

2. Experiments and Theories

2.1. Introduction

This chapter outlines the experimental methodologies and theoretical foundations used in this study. It covers buffer chemistry, electrochemical testing, impedance spectroscopy, cyclic voltammetry, surface characterization, and nuclear magnetic resonance (NMR) analysis, with the aim of evaluating the performance and stability of buffered aqueous zinc-ion batteries (AZIBs).

2.2. Cell Assembly and Testing

Two cell configurations were employed: (1) coin cells (CR2032) for ex-situ electrochemical testing, and (2) custom-designed cartridge cells for in situ/operando measurements. The cathode is prepared as following procedures.

A composite electrode slurry was prepared using commercial-grade MnO_2 powder (Salient Inc., mixed phase as supplied), poly (vinylidene fluoride) (PVDF, Sigma-Aldrich) binder, and carbon black (Salient Inc.). These components were combined in a mass ratio of 50:10:40 (MnO_2: PVDF: carbon black). The dry powders were added directly to a pre-mixed isopropanol (IPA) and deionized water solution with a volume ratio of 3:1 (IPA:H_2O).

The mixture was stirred thoroughly at room temperature using a mechanical shaker to form homogeneous and viscous slurry. The slurry was then cast onto carbon paper substrates (Fuel Cell Store) using a doctor blade with a 250 μm gap (wet thickness). The

coated electrodes were dried in an oven at 70 °C for 1 hour under ambient atmosphere. After drying, the electrodes were stored in sealed bags at room temperature until use.

Circular cathode and anode electrodes (zinc metal) were prepared using a ½-inch (1.27 cm^2) metal punch. Glass fiber separators (Whatman, grade GF/D) were punched to ¾-inch diameter to ensure full coverage of the electrodes. CR2032-type coin cells were assembled in ambient atmosphere using standard crimpers. A total of 100 µL of electrolyte was added to each cell using a calibrated volumetric pipette. The cell completed are followed by cycling test on Arbin Electrochemical Workstation.

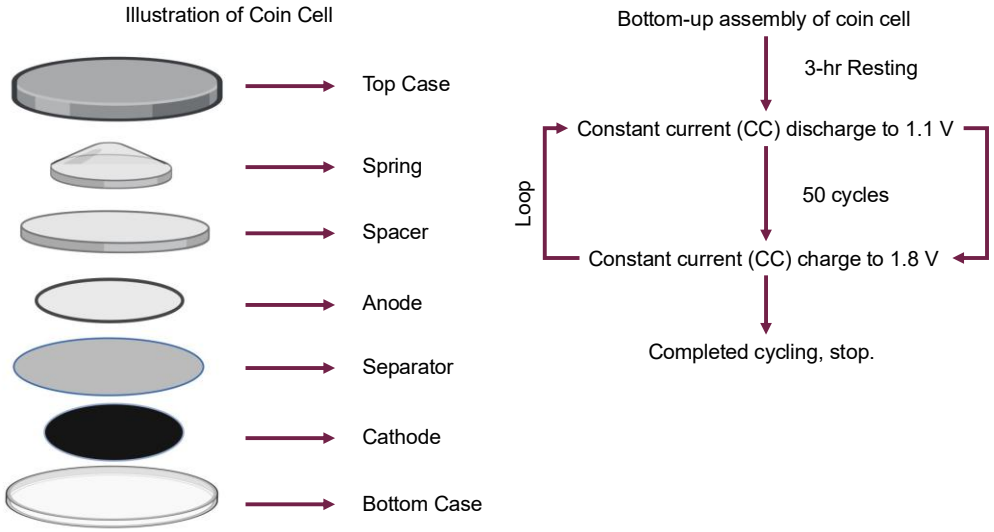

Figure 8 Illustration of coin cell structural design (Left) and electrochemical testing protocols associated with.

Coin cells are incompatible with the standard in-situ NMR probe due to their structure and metal interference. Therefore, custom-designed Teflon cartridge cells are employed. The cartridge cells follow a similar structural analog to coin cells, but the cathode and anodes are cut in accordance with the shape of the cell. An illustration is used here to explain the cartridge cell anatomy. Final assembled cells are wiped clean and cycled in the method described in 2.4.1. The assembled coin and cartridge cells are shown in Figure 10.

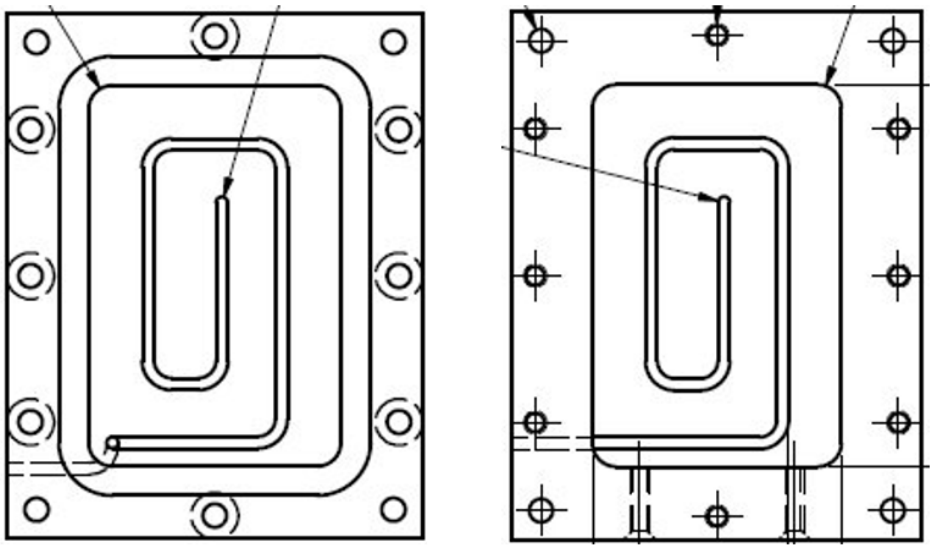

Figure 9 CAD design graph of cartridge cell with screw holes for fixing. Graph prepared by K. J. Sanders et al. actual assembly to be presented in later sections.

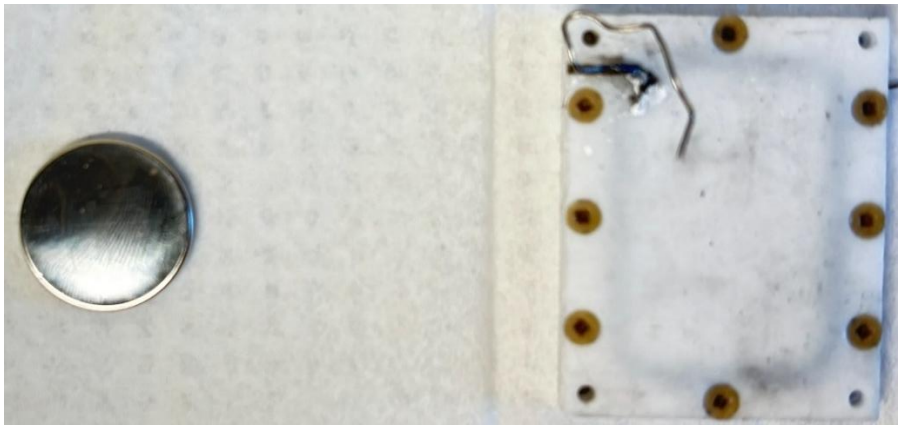

Figure 10 Illustration of assembled coin cell (L) and cartridge cell (R)

2.3.Buffer Chemistry and Electrolyte Formulation

Broadly speaking, buffers are a group of compounds that could resist significant pH changes upon acidification or alkalinization in aqueous solutions. By definition, buffers are combinations of a weak acid and its conjugate base. As discussed in Chapter 1, various buffers can be used as electrolyte additives to improve the performance of AZIBs. [34] Essentially, buffering groups or ions can dissociate in aqueous solutions forming either hydronium (H_3O^+) or hydroxide ions (OH^-), contributing to pH control via equilibrium.

The pH buffering range is primarily governed by the acid dissociation constant (pKa) of the buffer system. A properly chosen buffer with pK_a values could optimize the performance of the aqueous electrolyte.

The pH of a buffer could be determined via Henderson-Hasselbach equation, which can be illustrated in Equation 3. [25]

$$pH = pK_a + log\left(\frac{[A^-]}{[HA]}\right).$$

Equation 3 Henderson Hasselback Equation, pKa is the acidic dissociation constant of the buffer group, $[A^-]$ is the concentration of conjugate base, [HA] is the concentration of weak acid in solution.

In AZIBs, maintaining a stable electrolyte pH is critical to control side reactions. Acidification, often caused by H^+ generation during MnO_2 redox cycling or Zn plating/stripping, promotes manganese dissolution and compromises the structural integrity of the cathode.[21] Severe acidification may also lead to anode dissolution, which potential uncontrolled reaction may occur. Conversely, localized alkalinization can result in the precipitation of zinc hydroxide species or formation of layered hydroxysulfates, leading to increased impedance due to these complexes may not dissolve over time. Even worse, insoluble Mn-complexes may form as an irreversible result.[22] Accumulation of insoluble complexes may eventually lead to unusually high internal impedance, causing premature failure of the cell.

Both acidification and alkalinization could contribute to electrolyte decomposition, forming gases contribute to cell swelling. Therefore, pH fluctuations undermine both energy efficiency and capacity retention over extended cycling. To address these challenges, buffering agents are commonly used to stabilize the electrolyte's pH.[35]

Among various buffers, phosphate buffers are particularly appealing due to their appropriate pKa values, compatible with aqueous electrolytes and stability over a broad range of pH. Phosphate buffers are typically multi-functional, meaning they can release more than one proton in response to system changes. This is primarily due to their multi-step dissociation which can be illustrated as follows Equation 4 using phosphoric acid as a demonstration. [36]

$$H_3PO_4 \leftrightarrow H_2PO_4^- + H^+ \leftrightarrow HPO_4^{2-} + H^+ \leftrightarrow PO_4^{3-} + H^+$$

Equation 4. Illustration of dissociation of typical phosphate-based buffers, using phosphoric acid as an example.

In this study, a customized buffer system based on previous research[36] was designed using 50 mM ammonium dihydrogen phosphate ($NH_4H_2PO_4$, NHP) and 5 mM acetic acid. This buffered solution is dissolved in the 1 M $ZnSO_4$ electrolyte and used in AZIB. NHP contributes both NH_4^+ and $H_2PO_4^-$ buffering groups, offering a dual-action buffer capable of stabilizing pH across acidic and near-neutral ranges. The addition of acetic acid enhances buffering and may suppress early-stage Mn dissolution. Compared to the unbuffered electrolyte, 1 M $ZnSO_4$ solution in water, this buffered solution is tested for its longevity and improvements to the aqueous system in AZIB. [36]

The pKa of each group are: 9.25 (NH_4^+), 2.15 ($H_2PO_4^-$), 7.20 (HPO_4^{2-}), and 12.32 (PO_4^{3-}). However, the proper range for AZIB to function extreme can be adjusted based on the voltage potential applied. Evaluating the buffering capacity of prepared electrolytes can be achieved via external titration experiments, utilizing volumetric titration to assess the effectiveness of the prepared electrolyte. In this research, a comprehensive discussion of the buffer applied in experimental results are in following chapters.

Buffering capacity was evaluated by acid-base titration, in which aliquots of strong acid (HCl) or base (NaOH) were incrementally added to the electrolyte while monitoring pH response. The flatness of the titration curve reflects the buffer's resistance to pH change. In this study, volumetric titration was used to evaluate relevant buffering capacity.

2.4.Electrochemical Testing and Impedance

2.4.1. Galvanostatic Charge and Discharge

Galvanostatic charge/discharge testing was used to evaluate cell capacity, rate capability, and cycling stability. Cells were charged and discharged at a fixed current of a C-rate ($^{C}/_{4}$) between voltage cutoffs of 1.1 V and 1.8 V.[35] The theoretical capacity of MnO_2 was referenced as 308 mAh/g.[33] The C-rate is defined as relative to the theoretical capacity of the active material. A $^{C}/_{4}$ rate corresponds to a full charge or discharge in 4 hours.

During the charge phase, the battery is charged at a constant current until it reaches a desired voltage, and during the discharge phase, the battery is discharged at the same constant current until the voltage drops to the cutoff value. The amount of charge or discharge is recorded during each cycle to calculate the cell's capacity, which is expressed in milliampere-hours (mAh) or ampere-hours (Ah). This test allows for the evaluation of key performance parameters, such as capacity, cycle life, and rate capability. For this test, the theoretical capacity of MnO_2 is 308 mAh/g as a reference value, with designated C-rate to be $\frac{C}{4}$ and cut off voltage is 1.1 V and 1.8 V.

By monitoring the capacity retention over successive cycles, it provides an insight into the durability and long-term stability of the battery, including how electrolyte additives, such as buffers, influence cycling performance. The constant current charge and discharge test

is crucial for determining the practical viability of a battery system in real-world applications.

2.4.2. Electrochemical Impedance Spectroscopy (EIS)

One of another important parameters in the batteries is called impedance. Impedance in the battery can arise from multiple sources, such as electrode materials, the assembly or cell aging. Various parts of the cell may have different impedances with respect to each other. The overall contributed impedance as well as individual parts is not measurable by macroscopic multimeter, rather measurable by electrochemical workstation.

EIS was employed to investigate the internal resistance and interfacial properties of AZIBs. Impedance was measured using a Gamry Interface 5000 potentiostat. EIS functions by applying a small alternating current (AC) signal to the system and measuring the resulted response voltage across a range of frequencies.[19] By analyzing the impedance response at different frequencies, EIS plots an overall picture of various electrochemical processes, such as charge transfer, ion diffusion, and capacitance, which is critical in understanding the process of the battery and internal structures.

EIS work based on the fundamental that various chemical processes happen at different timescales, corresponding to the different frequencies of the applied signal. For example, in electrolytes, electrons move faster than ions or molecules, especially the bulky ones. By taking this into account, high frequency measurement primarily plots the impedance of the electrolyte and internal resistance. On the contrary, low-frequency measurements offer information of slower process, such as ion movement or diffusion, or the interface process between electrolyte and electrode. Given this property, this gives EIS an overall excellent tool for measuring cell stability, performance and internal changes. Three

important parameters are determined from the Nyquist plot in a typical EIS output, R_s (also written as R_u), R_{ct}, and Z_w. R_s is the bulk electrolyte resistance (intercept at high-frequency end), while R_{ct} is charge transfer resistance (diameter of semicircle) and $\mathrm{Z_w}$ is the Warburg impedance, derived from the slope at low frequencies.[19] [9]

A standard and ideal EIS plot are seen as the picture Figure 11. On the left, a semicircle indicated region of kinetic control at high frequency, which the intersection with Z' indicated bulk resistance. On the climax of semicircle, the value of vertical axis corresponds to the maximum imaginary impedance, it also corresponds to the the best point to analyze the interfacial dynamics. On the right part of the graph, a 45° line indicated the Warburg region, where dynamics control plays a role, or in other words, the diffusion-dominated area. [19]

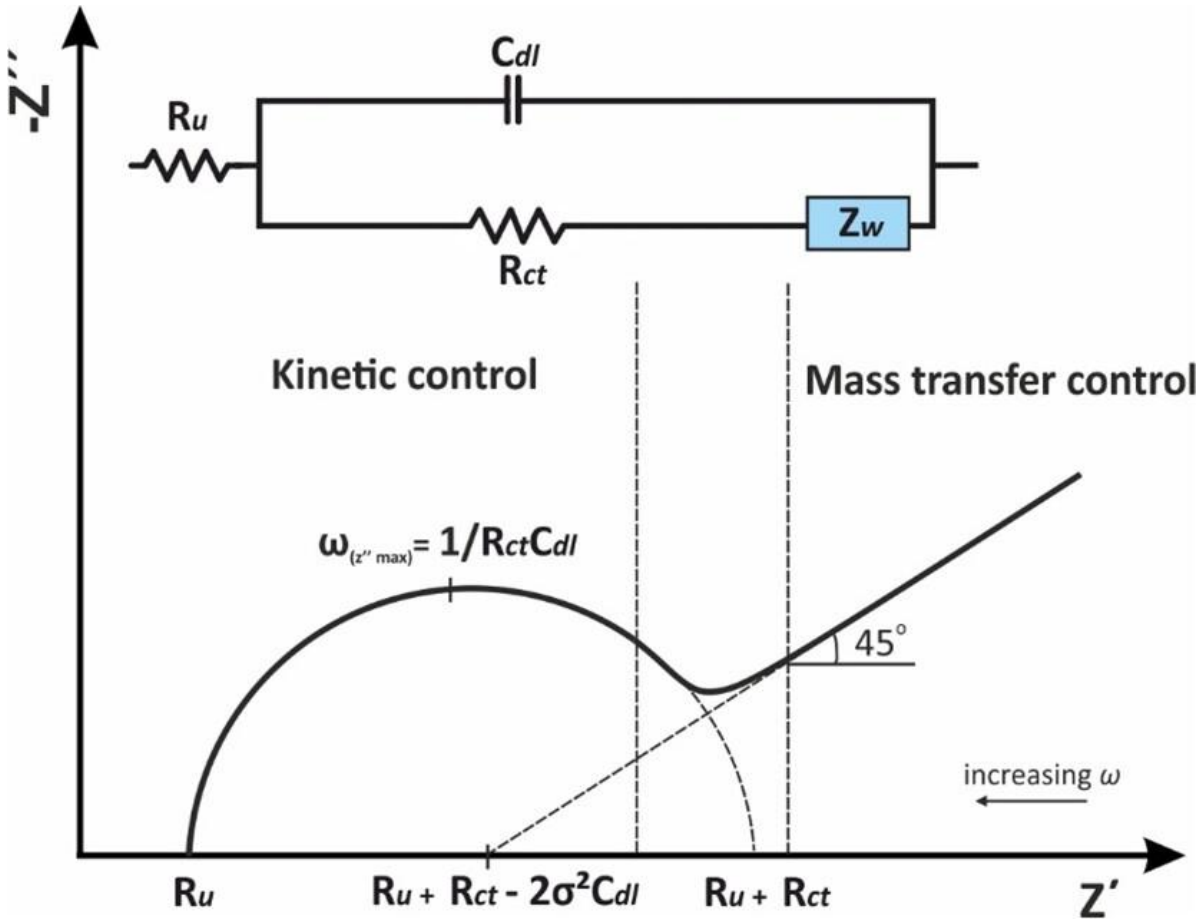

Figure 11 A reference EIS spectra with a semicircle and warburg tail. The equivalent circuit modelling as a Randles circuit is shown.[19] Reprinted with permission, Copyright © 2023.

For aqueous zinc-ion batteries (AZIBs), EIS is particularly valuable in evaluating the effects of electrolyte additives, such as buffers, on the overall performance. We are also able to know if buffer plays a role in internal structure in the long-term.

The technique allows for the determination of key parameters like the charge transfer resistance, which can be influenced by ionic strength in the electrolyte. We may also be able to check the Warburg factor, a metric for diffusion-dominated process. By providing a detailed picture of the battery's internal resistance and impedance changes over time, EIS helps in understanding degradation mechanisms, including the build-up of resistive layers, if possible, electrode degradation, and the impact of electrolyte composition on the

cell's cycling stability. This makes EIS an essential tool in the development and optimization of AZIBs, where the long-term stability and efficiency of the electrolyte and electrodes are critical to their overall performance.

To quantitatively interpret the EIS results, equivalent circuit modeling was employed using a modified Randles circuit. This circuit typically consists of a series resistance (R_s), representing the bulk electrolyte (also known as R_u) and contact resistance; a charge-transfer resistance (R_{ct}) in parallel with a double-layer capacitance (C_{dl}), representing the kinetics of the electrode–electrolyte interface; and a Warburg impedance (Z_w), modeling the diffusion of ions through the electrode or electrolyte. In some cases, the C_{dl} element is replaced by a constant phase element (CPE) to account for surface roughness or non-ideal capacitive behavior. Fitting was performed using Gamry EchemAnalyst Software, and extracted parameters were used to compare interfacial properties of buffered and unbuffered cells. This modeling approach is widely adopted in battery research and has been applied in various electrochemical systems such as LIBs to monitor electrode degradation, SEI formation, and ionic conductivity changes during cycling.[11]

2.5.Cyclic Voltammetry

Cyclic voltammetry (CV) is a widely used electroanalytical technique for probing redox behavior, reaction kinetics, and electrochemical reversibility of electrode materials. In this work, CV was employed to investigate the redox activity of MnO_2 cathodes in AZIBs and to evaluate the influence of buffer-modified electrolytes on electrochemical properties.

The principle of CV involves measuring the current response of an electrode as a function of the applied potential, which is cycled linearly between positive and negative

directions.[10] As the potential varies, oxidation and reduction reactions occur at the electrode surface, generating characteristic peaks that are plotted as a voltammogram. Peak position reflects redox potential; peak separation and current ratios indicate reversibility and kinetic control.[12]

In AZIBs, CV is used to assess the chemical kinetics within coin cell configurations as two-electrode systems. In this setup, MnO_2 acts as the working electrode where electrochemical reactions happen, and metallic Zn serves as both counter and quasi-reference electrode. As such, all potentials are referenced to Zn^{2+}/Zn.

Experimental factors such as scan rate, step size, and starting voltage influence the resolution and shape of the cyclic voltammogram.

Scan rate is a critical parameter determining CV profiles. Faster scan rates enhance current response but may broaden peaks and distort redox resolution, while slower scan rates provide greater detail on reversible kinetics. In this study, the scan rate is determined from various screening experiment balancing quality of spectra while enable efficient collection, the determined scan rate is finalized as 2.5 mV/s.[13]

In AZIBs, where MnO_2 is the primary cathode material, the key redox reactions involve manganese. MnO_2 undergoes multi-step redox reactions during cycling, involving transitions between Mn (IV), Mn (III), and Mn (II) species.[12] During charging, Mn (IV) may dissolve into the electrolyte forming Mn^{2+} via disproportionation. Discharge reverses this, enabling redeposition of Mn-based species.[29] These multi-step processes result in multiple cathodic and anodic peaks in the CV curve.

Electrolyte additives, such as buffer agents, can also influence the electrochemical processes within the cell, and these effects can be observed in the cyclic voltammogram. For example, buffer groups may shift the redox peaks or improve the reversibility of certain reactions, providing further insights into how the electrolyte composition affects the overall electrochemical behavior and efficiency of the cell.

CV is also valuable for evaluating the charge-discharge kinetics of the battery system. By analyzing the voltammogram, it is possible to determine whether the electrochemical process is primarily controlled by kinetic factors, such as electron transfer or ion diffusion, or by thermodynamic factors, such as equilibrium conditions.[10] If the current response is limited by the rate of electron transfer or ion diffusion, the process is considered to be kinetics-controlled, while a rapid attainment of equilibrium suggests thermodynamic control.

The voltammogram can be further analyzed for additional insights into the electrochemical system. The separation between the oxidation and reduction peaks reflects the reversibility of the redox reactions. By integrating the area under the peaks and comparing it to the baseline, it is possible to assess whether the reaction has reached equilibrium and evaluate its reversibility. The peak current, which is related to the current density, offers additional information on the electrochemical activity and capacity of the material. Higher current densities indicate that the material can accommodate a higher rate of electron transfer, which is crucial for efficient battery performance.[10] [13] [29]

To ensure the reliability and stability of the data, CV is typically performed over multiple cycles. This repetition helps stabilize the data and allows for the observation of peak shifts

or intensity changes over time. Such changes may indicate degradation of the material or shifts in the electrochemical behavior of the cell.

CV experiments in this work served as a diagnostic probe to monitor electrochemical performance, reversibility, and degradation over multiple cycles in both buffered and unbuffered electrolyte systems.

Other information could be extracted from CV using detailed analysis, such as capacitance and charges involved in the reaction.

Capacitance values were derived from cyclic voltammetry measurements performed at a fixed scan rate. To ensure consistency, all curves were baseline-corrected using a horizontal reference line at 0.00 A. The area enclosed by the CV curve, both above and below this baseline, was numerically integrated to quantify the total charge transferred during one full voltage cycle.

Capacitance was extracted from cyclic voltammetry collected at a fixed scan rate $v(\mathrm{V} * \mathrm{S}^{-1})$ All CVs were baseline-corrected to $I = 0\ A$. The capacitance observed in one full cycle was obtained by numerically integrating the enclosed area of the CV:

$$C = \frac{\int I(V)dV}{2\ v\ \Delta V}$$

Equation 5 Determine capacitance from CV, equations from [3]

The numerator parameter ($\int I(V)dV$) is the integrated current area, defined in C (Coulombs), while the v term is the scan rate in volts per second. The ΔV term is the potential window in volts. Factor 2 in the denominator is accounted for forward and backward sweeps. Total capacitance is defined in Farad (F).

Given that all experiments are scanned under identical scan rates, scan rate normalization is not required. Thus, determined capacitance will be expressed in areal capacitance $C_A = \frac{C}{A}(F\ cm^{-2})$.[13] [10] [29]

2.6.Surface Characterization

During repetitive charge/discharge cycling, electrode materials undergo structural and chemical transformations that affect battery performance. Surface characterization provides insight into these processes, particularly MnO_2 dissolution/redeposition and interactions with electrolyte components. Post-mortem analysis of cycled electrodes allows for the visualization and quantification of degradation phenomena, which are not accessible through routine electrochemical measurements.[35] [30] In the case of the AZIB system, the structure of the electrode may not remain consistent throughout cycling. To comprehensively understand these structural changes, cathode samples are collected before and after cycling and analyzed using microscopy.

Cathode samples were retrieved from disassembled coin cells using a hydraulic crimper. After removal, electrodes were wetted with deionized water to remove glass fiber separator. The remaining cathode was left air-dried in a sealed container for 24 hours prior to imaging. Surface morphology and microstructure were analyzed using scanning electron microscopy (SEM, FEI Magellan 400) at the Canadian Centre for Electron Microscopy (CCEM). Imaging was performed under high vacuum with a varying voltage independent to samples. SEM utilizes electrons as source of probe with varying voltage and current density, enabling dynamic screening of surface morphology.

To fully understand the composition of the materials used, X-ray diffraction (XRD) was conducted on pristine MnO_2 powder using a Rigaku diffractometer with Cu Kα radiation ($\lambda = 1.5406$ Å) over a 2θ range of 10°–80°.

SEM and XRD results were used to correlate structural degradation with capacity fading and impedance growth observed during electrochemical testing. MnO_2 cathodes after extended cycling were evaluated for signs of structural distortion, surface morphology, or surface passivation

2.7.NMR Theory

Nuclear magnetic resonance (NMR) spectroscopy is a versatile and powerful analytical tool widely used to study the structure, dynamics, and molecular interactions of various substances. In recent years, NMR has been widely used in battery science, particularly for the observation of internal changes of battery cells during operation. This approach, known as operando NMR, provides real-time insights into the chemical and physical processes occurring within a battery while it is cycling.[24] Unlike conventional post-mortem techniques, NMR allows non-invasive, in situ tracking of ion migration, phase transitions, and interactions between dissolved species and the electrolyte. The ability to perform in-situ measurements enables researchers to study processes such as ion migration, phase transitions, and electrolyte stability directly, without the need to disassemble the cell.

However, one of the challenges in performing operando NMR experiments in battery systems is the conventional design of battery cells, which may not be directly compatible with NMR probes. The geometry of typical battery cells, along with the need for sealing and high conductivity, often prevents the straightforward integration of NMR spectrometers with standard cell configurations. Overcoming this limitation requires

specialized cell designs or modifications that allow NMR-compatible materials and electrodes to be used, enabling the in-situ measurement of electrochemical processes. In recent years, a special cell setup with relevant parallel plate resonator design enables the in-situ experiment. The parallel-plate resonator design ensures magnetic field homogeneity across the region of interest.[2] Materials of the cell covering can also be optimized to minimize interference. For example, for interests in H nuclei, a Teflon cartridge can be applied, with no external H interference.

One of the fundamental principles of NMR is the interaction of atomic nuclei with an external magnetic field. In a magnetic field, nuclei with non-zero spin (e.g., ^{1}H, ^{7}Li) absorb radiofrequency energy at a resonance frequency determined by their local electronic environment. This frequency shift, or chemical shift, provides insights into molecular structure and interactions.[32] [5] In battery systems, ^{1}H nuclei (protons) are abundant in aqueous systems and highly sensitive in NMR, making them ideal for monitoring electrolyte dynamics. Water, as the primary component of many aqueous electrolytes, contributes significantly to the NMR spectra, providing valuable information about the ionic environment.

The success of NMR measurements in battery systems also heavily relies on nuclear spin properties. Most nuclei detected in NMR, such as hydrogen and lithium, possess a spin of ½, making them suitable for detection.[32] In lithium-ion batteries (LIBs), for example, lithium ions are commonly tracked using NMR to study ion movement and diffusion. In aqueous zinc-ion batteries (AZIBs), hydrogen nuclei (^{1}H) are critical for studying the electrolyte and the interactions with other species, especially under varying electrochemical conditions.

In NMR, the relaxation of nuclear spins is strongly influenced by the presence of nearby unpaired electrons. This effect is rooted from electrons bearing much larger magnetic moments than the protons, which is known as the gyromagnetic ratio (γ). The gyromagnetic ratio for electron ($\gamma_e \approx 1.76 \times 10^{11}$ rad·s^{-1}·T^{-1}) is hundreds of times greater than that of the proton ($\gamma_h \approx 2.68 \times 10^{8}$ rad·s^{-1}·T^{-1}). [14] [1] Since the dipolar coupling constant that dominates electron–nuclear spin interactions scales with the product $\gamma_e\gamma_n$, even small concentrations of paramagnetic centers can have a disproportionately large influence on nuclear relaxation. [17] [20]

As a result, unpaired electrons generate strong fluctuating local magnetic fields that possibly trigger nuclear spin flips, thereby accelerating both longitudinal (T_1) relaxation and transverse (T_2) relaxation. This phenomenon explains the markedly shortened proton relaxation times and broadened resonance lines observed in systems containing paramagnetic ions such as Mn, Fe, or Cu. Such effects are highly relevant in aqueous zinc–manganese dioxide batteries, where Mn redox activity leads to environments with strong electron–nuclear interactions. [6] [8] [28] [7]

Paramagnetic species are atoms or ions that have unpaired electrons, such as Mn (II) in this context. The presence of these unpaired electrons allows interactions with nuclear spins, particularly those with a spin of ½, leading to unique spectral features.[12] [23] One of the consequences of these interactions is the broadening of NMR peaks, which can shift from high-field to low-field. In some cases, this broadening can obscure smaller peaks next to the major ones, making it challenging to distinguish subtle spectral features. Due to such effect, measuring H NMR signals in aqueous electrolyte becomes difficult as spectra obtained is being distorted. [23] [3]

In addition to peak broadening, paramagnetic effects also influence the relaxation times of nuclei in the system. Relaxation refers to the time required for the nuclei to return to their equilibrium state after being disturbed by a radiofrequency pulse. There are two primary types of relaxation times: spin-lattice relaxation (T_1) and spin-spin relaxation (T_2). Usually, the relaxation time parameters are fixed for the same nuclei in molecule across systems, however, paramagnetic species impact both relaxation processes, but the effect on T_1 is particularly important in this study.[23] [16] The spin-lattice relaxation time (T_1) reflects the speed of nuclear spins return to equilibrium. Its inverse, $R_1 = 1/T_1$, increases in the presence of paramagnetic species, providing a quantitative indicator of Mn^{2+} concentration. This relationship has been validated as a reference.[4] This relationship helps in understanding the extent of paramagnetic effects on the system, offering valuable insights into the presence and behavior of paramagnetic species, such as Mn (II), within the sample. In AZIBs, paramagnetic Mn^{2+} ions ($3d^5$, high spin) strongly interact with nuclear spins through dipolar coupling, resulting in broadened NMR peaks and altered relaxation behavior. Recently, utilization of this property gives quantitative information of Mn (II) evolution for the first time in our lab. The details on correlation and interpretation is explained in Chap. 4.

2.8.Review

This chapter outlined the theoretical background and experimental methodologies used to investigate the stability and performance of aqueous zinc-ion batteries (AZIBs) under native and buffered electrolyte conditions.

A phosphate and acetate-based buffer system was developed to mitigate adverse reactions during cycling, aiming to suppress side reactions and excessive precipitation. The

electrolyte's chemical buffering behavior was characterized via titration and theoretical dissociation analysis.

Electrochemical testing, including galvanostatic charge/discharge, cyclic voltammetry (CV), and electrochemical impedance spectroscopy (EIS), was applied to assess ability retention, reaction kinetics, and internal resistance evolution. Surface characterization by scanning electron microscopy (SEM) and X-ray diffraction (XRD) provided morphological and crystallographic insights into electrode degradation mechanisms. Additionally, operando nuclear magnetic resonance (NMR) spectroscopy was used to monitor real-time electrolyte behavior, with a focus on Mn^{2+} accumulation and proton environment changes.

These complementary methods form a comprehensive experimental platform for understanding the effects of buffer additives on electrochemical performance and long-term cycling behavior. The following chapter presents the results and analysis derived from this integrated approach.

2.9.References

[1] Abragam, M. *The Principles of Nuclear Magnetism*; Claredon Press, 1961.

[2] Aguilera, A. R.; Sanders, K. J.; Goward, G. R.; Balcom, B. J. The Parallel-PLATE RESONATOR: An RF Probe for MR and MRI Studies over a Wide Frequency Range. *Magnetic Resonance Letters* **2023**, *3* (4), 306–318.

[3] Allen, J. P.; Grey, C. P. Solution NMR of Battery Electrolytes: Assessing and Mitigating Spectral Broadening Caused by Transition Metal Dissolution. *The Journal of Physical Chemistry C* **2023**, *127* (9), 4425–4438.

[4] Allen, J. P.; O'Keefe, C. A.; Grey, C. P. Quantifying Dissolved Transition Metals in Battery Electrolyte Solutions with NMR Paramagnetic Relaxation Enhancement. *The Journal of Physical Chemistry C* **2023**, *127* (20), 9509–9521.

[5] Berkson, Z. J.; Cao, W.; Gioffrè, D.; Kaul, C. J.; Lätsch, L.; Kakiuchi, Y.; Yakimov, A.; Copéret, C. NMR Signatures of Transition-Metal Nuclei: From Local Environments and Electronic Structures to Reactivity Descriptors in Molecular and Heterogeneous Catalysis. *JACS Au* **2025**, *5* (7), 2911–2931.

[6] BLOEMBERGEN, N.; PURCELL, E. M.; POUND, R. V. Relaxation Effects in Nuclear Magnetic Resonance Absorption. *Resonances* **1990**, 411–444.
[7] Bloembergen, N.; Purcell, E. M.; Pound, R. V. Relaxation Effects in Nuclear Magnetic Resonance Absorption. *Physical Review* **1948**, *73* (7), 679–712. DOI:10.1103/physrev.73.679.
[8] Chem. Rev. 1987, 87, 5, 901–927
[9] Cui, X.; Li, Y.; Zhang, Y.; Sun, Z.; Liu, Y.; Zhang, J.; Xie, E.; Fu, J. Unraveling the Electrochemical Charge Storage Dynamics of Defective Oxides-Based Cathodes toward High-Performance Aqueous Zinc-Ion Batteries. *Chemical Engineering Journal* **2023**, *478*, 147197.
[10] Elgrishi, N.; Rountree, K. J.; McCarthy, B. D.; Rountree, E. S.; Eisenhart, T. T.; Dempsey, J. L. A Practical Beginner's Guide to Cyclic Voltammetry. *Journal of Chemical Education* **2017**, *95* (2), 197–206.
[11] Hu, W.; Peng, Y.; Wei, Y.; Yang, Y. Application of Electrochemical Impedance Spectroscopy to Degradation and Aging Research of Lithium-Ion Batteries. *The Journal of Physical Chemistry C* **2023**, *127* (9), 4465–4495.
[12] Jung, M. S.; Hoang, D.; Sui, Y.; Ji, X. Impact of Air Exposure on the Performance of the MNO2 Cathode in Aqueous Zn Batteries. *ACS Energy Letters* **2024**, *9* (9), 4316–4318.
[13] Khalafi, L.; Cunningham, A. M.; Hoober-Burkhardt, L. E.; Rafiee, M. Why Is Voltammetric Current Scan Rate Dependent? Representation of a Mathematically Dense Concept Using Conceptual Thinking. *Journal of Chemical Education* **2021**, *98* (12), 3957–3961.
[14] Kibble, B. P.; Hunt, G. J. A Measurement of the Gyromagnetic Ratio of the Proton in a Strong Magnetic Field. *Metrologia* **1979**, *15* (1), 5–30.
[15] Kolonko, E. M.; Kolonko, K. J. Introducing NMR Spectroscopy Using Guided Inquiry and Partial Structure Templating. *Journal of Chemical Education* **2019**, *96* (5), 912–919.
[16] Kowalewski, J.; Mäler, L. In *Nuclear spin relaxation in liquids: Theory, experiments, and applications*; CRC Press, 2018.
[17] Kowalewski, J.; Mäler, L. *Nuclear Spin Relaxation in Liquids: Theory, Experiments, and Applications*; CRC Press, 2018.
[18] Krachkovskiy, S. A.; Reza, M.; Aguilera, A. R.; Halalay, I. C.; Balcom, B. J.; Goward, G. R. Real-Time Quantitative Detection of Lithium Plating by in Situ NMR Using a Parallel-Plate Resonator. *Journal of The Electrochemical Society* **2020**, *167* (13), 130514.
[19] Lazanas, A. Ch.; Prodromidis, M. I. Electrochemical Impedance Spectroscopy─a Tutorial. *ACS Measurement Science Au* **2023**, *3* (3), 162–193.
[20] Lindon, J. C.; Tranter, G. E.; Holmes, J. L. *Encyclopedia of Spectroscopy and Spectrometry. Set*; Academic Press Imprint, Elsevier Science & Technology Books, 2000.
[21] Liu, M.; Wang, P.; Zhang, W.; He, H.; He, G.; Xu, S.; Yao, L.; Miller, T. S. Strategies for Ph Regulation in Aqueous Zinc Ion Batteries. Energy Storage Materials 2024, 67, 103248.

[22] Luo, M.; Li, T. C.; Wang, P.; Zhang, D.; Lin, C.; Liu, C.; Li, D.-S.; Chen, W.; Yang, H. Y.; Zhou, X. Dynamic Regulation of the Interfacial pH for Highly Reversible Aqueous Zinc Ion Batteries. Nano Letters 2023, 23 (20), 9491–9499.

[23] Novotny, J.; Komorovsky, S.; Marek, R. Paramagnetic Effects in NMR Spectroscopy of Transition-Metal Complexes: Principles and Chemical Concepts. *Accounts of Chemical Research* **2024**, *57* (10), 1467–1477.

[24] Pecher, O.; Carretero-González, J.; Griffith, K. J.; Grey, C. P. Materials' Methods: NMR in Battery Research. *Chemistry of Materials* **2016**, *29* (1), 213–242.

[25] Po, H. N.; Senozan, N. M. The Henderson-Hasselbalch Equation: Its History and Limitations. *Journal of Chemical Education* **2001**, *78* (11), 1499.

[26] Ran, Y.; Dong, F.; Sun, S.; Lei, Y. Aqueous Zinc-based Batteries: Active Materials, Device Design, and Future Perspectives. Advanced Energy Materials 2025.

[27] Sanders, K. J.; Ciezki, A. A.; Berno, A.; Halalay, I. C.; Goward, G. R. Quantitative *Operando* 7Li NMR Investigations of Silicon Anode Evolution during Fast Charging and Extended Cycling. *Journal of the American Chemical Society* **2023**, *145* (39), 21502–21513.

[28] Solomon, I. Relaxation Processes in a System of Two Spins. *Physical Review* **1955**, *99* (2), 559–565.

[29] Tang, Y.; Liu, H.; Zhu, X.; Liu, M.; Tang, W.; Wei, G.-X.; Feng, Y.-H.; Xiao, B.; Wang, P.-F. Restraining the Jahn–Teller Distortion in MN-Based Layered Cathodes toward High-Performance Potassium-Ion Batteries. *ACS Nano* **2025**, *19* (22), 21118–21129.

[30] Wang, R.; Chen, W.; Zhang, C.; Zhao, R.; Wang, X. Electrochemically Active MN2+ Enabling High-Performance Aqueous Zinc Ion Batteries. *Energy & Fuels* **2024**, *38* (14), 13436–13443.

[31] Wei, R.; Dickson, C. L.; Uhrín, D.; Lloyd-Jones, G. C. Rapid Estimation of *t*1 for Quantitative NMR. *The Journal of Organic Chemistry* **2021**, *86* (13), 9023–9029.

[32] Wink, D. J. Spin-Lattice Relaxation Times in 1H NMR Spectroscopy. *Journal of Chemical Education* **1989**, *66* (10), 810.

[33] Zhang, B.; Dong, P.; Yuan, S.; Zhang, Y.; Zhang, Y.; Wang, Y. Manganese-Based Oxide Cathode Materials for Aqueous Zinc-Ion Batteries: Materials, Mechanism, Challenges, and Strategies. *Chem & Bio Engineering* **2024**, *1* (2), 113–132.

[34] Zhang, B.; Yao, J.; Wu, C.; Li, Y.; Liu, J.; Wang, J.; Xiao, T.; Zhang, T.; Cai, D.; Wu, J.; Seh, Z. W.; Xi, S.; Wang, H.; Sun, W.; Wan, H.; Fan, H. J. Electrolyte Design for Reversible Zinc Metal Chemistry. Nature Communications 2025, 16 (1).

[35] Zhang, N.; Cheng, F.; Liu, J.; Wang, L.; Long, X.; Liu, X.; Li, F.; Chen, J. Rechargeable Aqueous Zinc-Manganese Dioxide Batteries with High Energy and Power Densities. Nature Communications 2017, 8 (1).

[36] Zhang, W.; Dai, Y.; Chen, R.; Xu, Z.; Li, J.; Zong, W.; Li, H.; Li, Z.; Zhang, Z.; Zhu, J.; Guo, F.; Gao, X.; Du, Z.; Chen, J.; Wang, T.; He, G.; Parkin, I. P. Highly Reversible Zinc Metal Anode in a Dilute Aqueous Electrolyte Enabled by a Ph Buffer Additive. *Angewandte Chemie* **2022**, *135* (5).

Chapter 3: Electrochemical Results

3. Electrochemical Evaluation of Buffered Electrolytes in AZIBs

3.1. Introduction of Background

This chapter investigates the electrochemical behavior of buffered and unbuffered aqueous zinc-ion battery systems using the methodologies established in Chapter 2. Comparative testing was conducted to assess the buffering effects on cycling stability, capacity retention, and overall performance.

The findings from galvanostatic charge/discharge, cyclic voltammetry, and impedance spectroscopy form the basis of this analysis. These results not only demonstrate the functional benefits of buffer additives but also provide experimental justification for the mechanistic interpretations discussed in Chapter 4.

3.2. Buffer Validation and Electrolyte Characterization

3.2.1. Buffer Composition and Capacity Definition

The buffered electrolyte, as mentioned in Chapter 2, consists of 50 mM NHP and 5 mM acetic acid dissolved in 1 M $ZnSO_4$ electrolyte. In comparison of buffered electrolyte, higher and lower concentrations of NHP were tested. A comparison of each electrolyte is shown as in Figure 12. Despite variation in NHP concentration, all electrolytes with buffer additive show no visible difference.

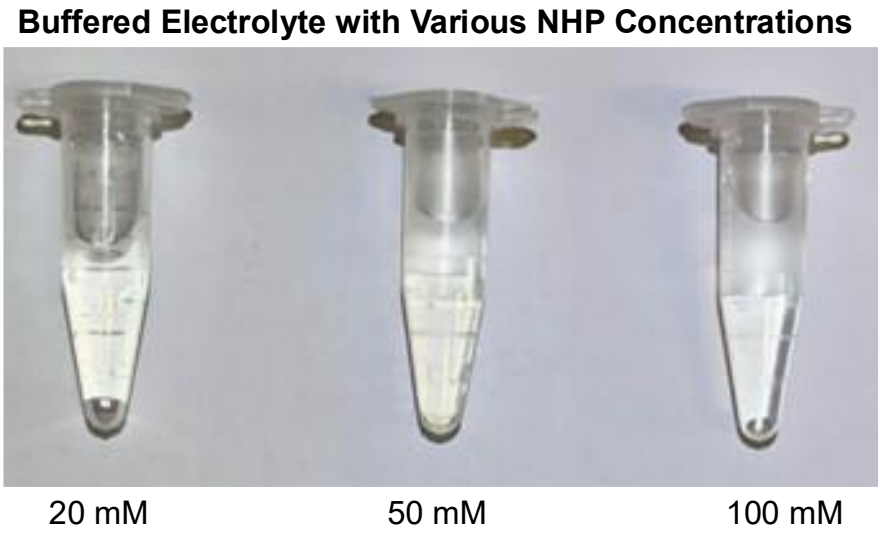

Figure 12 Comparison of Various Concentration of Buffered Electrolyte. All electrolytes are composed of 5 mM acetic acid and NHP dissolved in 1 M $ZnSO_4$ solution.

Each of the prepared buffered electrolyte, along with regular electrolyte with no additives were employed to examine their effect on cell performance using GCD testing. The testing comparison results are shown in the following sections.

3.2.2. pH Dependency of Buffers and Relevant Metrics

The pH of buffered electrolyte was influenced by NHP concentration. The pH measurement of buffered and unbuffered electrolyte is summarized in the table below. pH measurement was conducted using calibrated ThermoFisher AB315 pH meter.

Table 1 Characteristics of Buffered Electrolyte

Electrolyte Type	Measured pH
Unbuffered electrolyte (1 M $ZnSO_4$ aq)	4.80±0.02
Buffered with 20 mM NHP, 5 mM HAc	3.11±0.02
Buffered with 50 mM NHP, 5 mM HAc	2.82±0.02
Buffered with 100 mM NHP, 5 mM HAc	2.61±0.02

Observed pH difference among buffered and unbuffered electrolytes were prominent, which enables each cell to start at a different stage. To examine the buffering capacity of buffered electrolytes, the volumetric titration experiments were performed on buffered electrolyte with intermediate buffer concentration (50 mM NHP and 5 mM HAc). The graph below shows physical changes along alkalinization. Titrant prepared was standardized NaOH solution, mimicking increasing alkalinization the cell would go through in regular electrochemical cycling. Solution appearance along base addition is shown in Figure 13, with the detailed titration plot shown in

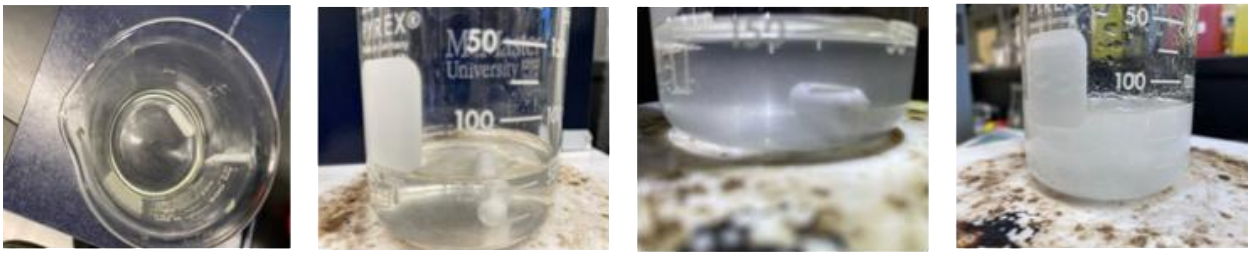

Figure 13 Analytical titration progress of buffered electrolyte. Electrolyte appeared to be clear initially, with minor precipitation occurred during base addition. Forming excessive cloudy cluster

in latent stages. The product formed was mostly zinc hydroxysulphate. Solid formed are reversible upon acidification.

As illustrated in the titration plot and solution phases, the buffering capacity of the prepared electrolyte is most effective around pH ≈ 3, which closely aligns with the initial pH of the buffered systems. Within this pH region, as referenced in the Mn–Zn Pourbaix diagram (Figure 14), the dominant redox processes involve the interconversion between Mn^{2+} ions and solid MnO_2. This zone supports reversible Mn-based redox activity without favoring dissolution into soluble or inactive forms such as MnO.

Zinc, under the same pH and electrochemical conditions, predominantly exists as Zn^{2+} ions in solution, with no evidence of insoluble byproduct formation such as zinc hydroxide or layered zinc salts. Furthermore, the electrochemical potential range used in this study (1.1–1.8 V vs. Zn/Zn^{2+}) remains outside the water instability window (~0.5 V and 1.9 V) under mildly acidic conditions, effectively avoiding parasitic side reactions such as oxygen evolution reaction (OER) and hydrogen evolution reaction (HER).

This established that the buffer system is effective in terms of pH control, while sustain a thermodynamically favorable environment for Zn^{2+} and MnO_2 cycling, thereby could support enhanced electrochemical performances.

3.2.3. Target pH range and MnO_2 redox relevance

The measured pH of the buffered and unbuffered electrolytes is evaluated in the context of the relevant redox reactivity of manganese and zinc species in aqueous

environments. As shown in the Pourbaix diagram (Figure 14), the electrochemical stability of Mn-based cathodes is highly sensitive to pH, particularly under the operational voltage window of 1.1–1.8 V vs. Zn/Zn^{2+}.

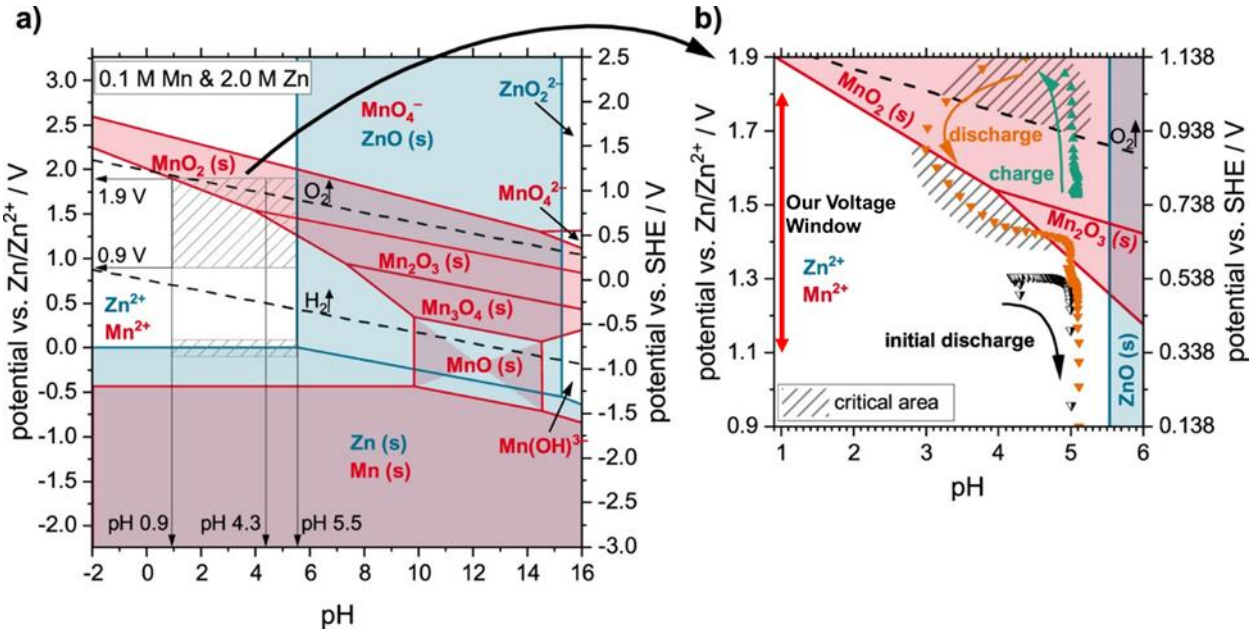

Figure 14 Pourbaix diagram of MnO_2 and Zn based on pH and relevant voltage. Figure adapted from reference[1] The desired pH range within our voltage window (1.1 V-1.8 V) should be 3-5, avoiding oxygen evolution and irreversible Mn-oxides formation.

Within this voltage range, MnO_2 undergoes multiple redox transitions, which are pH-dependent, as shown in Equation 6.

$$\mathrm{Mn(IV)} \rightleftharpoons \mathrm{Mn(III)} \;\&\; \mathrm{Mn(III)} \rightleftharpoons \mathrm{Mn(II)}$$

Equation 6 Mn Transitions of Various Oxidation States

In lower pH environments, Mn (II) can be highly soluble, potentially leading to irreversible manganese dissolution from the cathode. On the contrary, insoluble complexes of Mn and Zn, such as hydroxides or hydroxysulphates, could

precipitate, leading to an overall internal resistance increase and structural instability. Therefore, a proper pH must be controlled for optimal performance and suppressing parasitic side reactions and ensure reversibility of the MnO_2 redox processes.

To validate whether the buffered system effectively stabilizes the redox-active environment during cycling, we next examine the charge–discharge behavior of the cells under galvanostatic conditions. By comparing capacity retention, voltage profiles, and coulombic efficiency across buffered and unbuffered systems, we can assess whether pH stabilization translates into improved electrochemical performance.

3.3. Galvanostatic Charge-Discharge Testing

3.3.1. Initial GCD testing results

To evaluate the electrochemical performance of buffered and unbuffered systems, initial galvanostatic charge–discharge (GCD) tests were conducted under identical cycling conditions. The objective was to assess the impact of electrolyte buffering on specific capacity and capacity retention over early cycles. As established in previous sections, buffering is expected to mitigate pH-driven degradation mechanisms, potentially leading to enhanced reversibility and stability of the MnO_2 cathode.

All cells were cycled between 1.1 V and 1.8 V vs. Zn/Zn^{2+} at a constant current corresponding to C/4 (based on a theoretical MnO_2 capacity of 308 mAh/g). The results presented here reflect the first 25 cycles, offering a baseline comparison

before long-term degradation becomes significant. Capacity notation was converted to unit capacity providing a cross-comparison format. Material tested and presented were EMD 10 and EMD 1 based cathodes.

The initial testing on EMD 10 based cathodes is shown as follows.

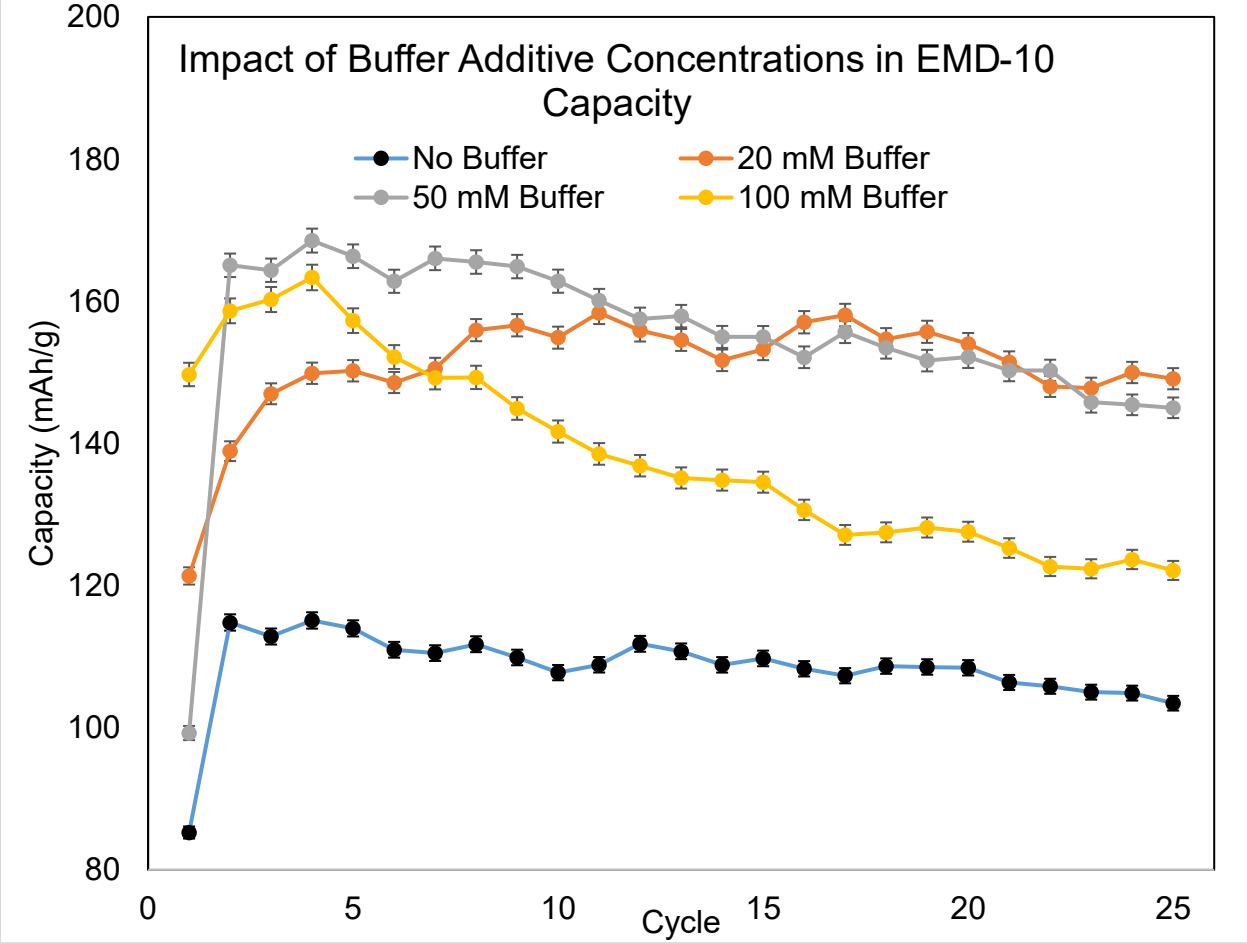

Figure 15 GCD test results for EMD-10 cells. Buffered (50 mM NHP & 5 mM HAc) electrolyte groups and unbuffered electrolyte cells were compared. Repetitive experiments were conducted with identical trends. Illustrated using discharge capacity.

As shown in Figure 15, the unbuffered electrolyte group exhibited the lowest specific capacity across all tested cells. In contrast, buffered systems demonstrated significant improvement, with all buffered groups delivering capacities at least 30%

higher than their unbuffered counterparts during the initial cycles. Although capacity fading was observed across all groups over prolonged cycling, buffered cells consistently retained higher capacity, indicating improved electrochemical stability.

Among the buffered groups, the electrolyte containing 50 mM buffer showed superior performance in the early stage's relative to both lower (20 mM) and higher (100 mM) concentrations. This concentration-dependent trend suggests that excessive or insufficient buffering may impair electrochemical kinetics or ionic conductivity. Based on this screening, the 50 mM buffered electrolyte was selected for further investigation in subsequent experiments. This concentration is comparable to literature values, ranging from 25 mM to 100 mM. [1] [4]

Similarly, buffer-spiked experiments were conducted on a similar cathode material, EMD-1, to examine if a similar response is visible. Here we have the plot of discharge and charge capacity, in relation to buffer concentrations.

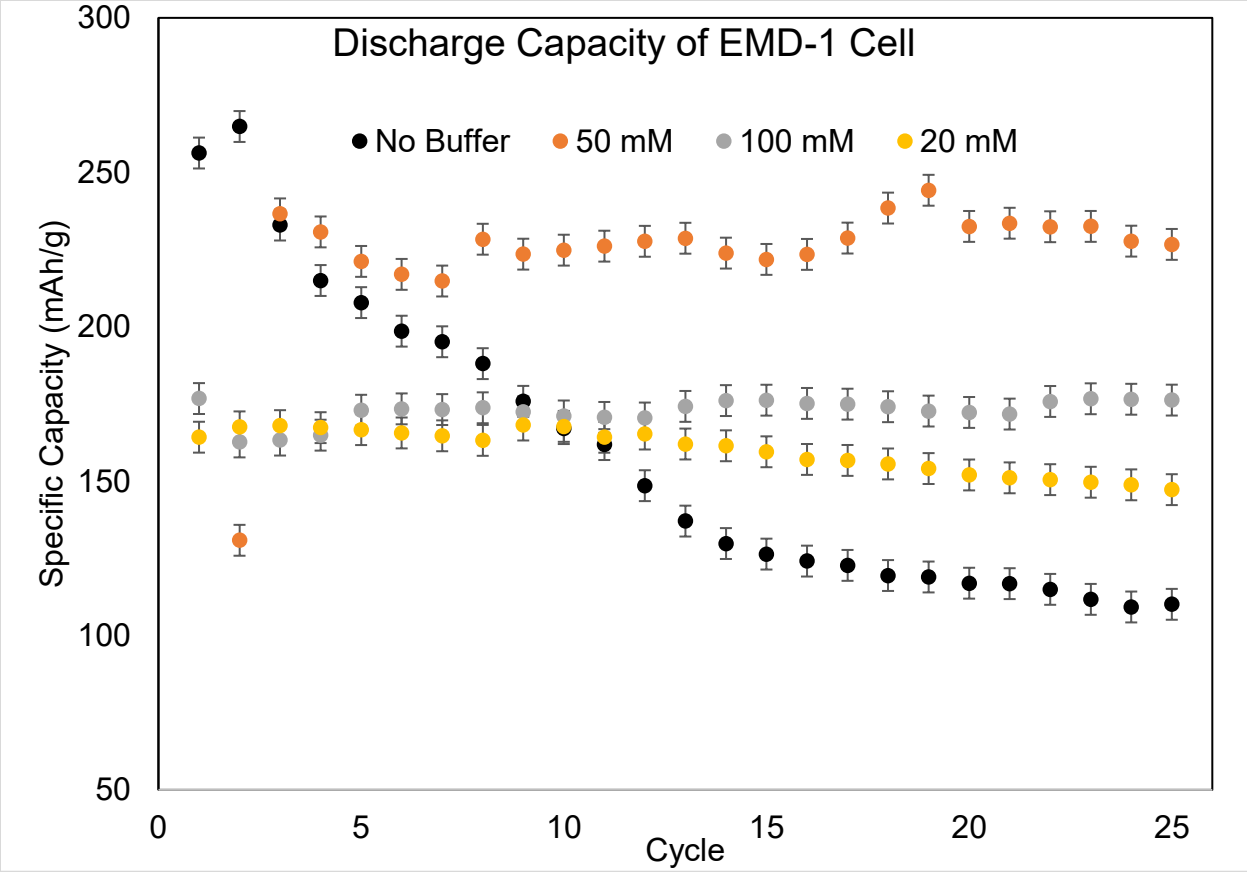

Figure 16 GCD testing of EMD-1 cell discharge capacity. Buffered (50 mM NHP & 5 mM HAc) groups exhibited steady capacity retention and stability than unbuffered groups.

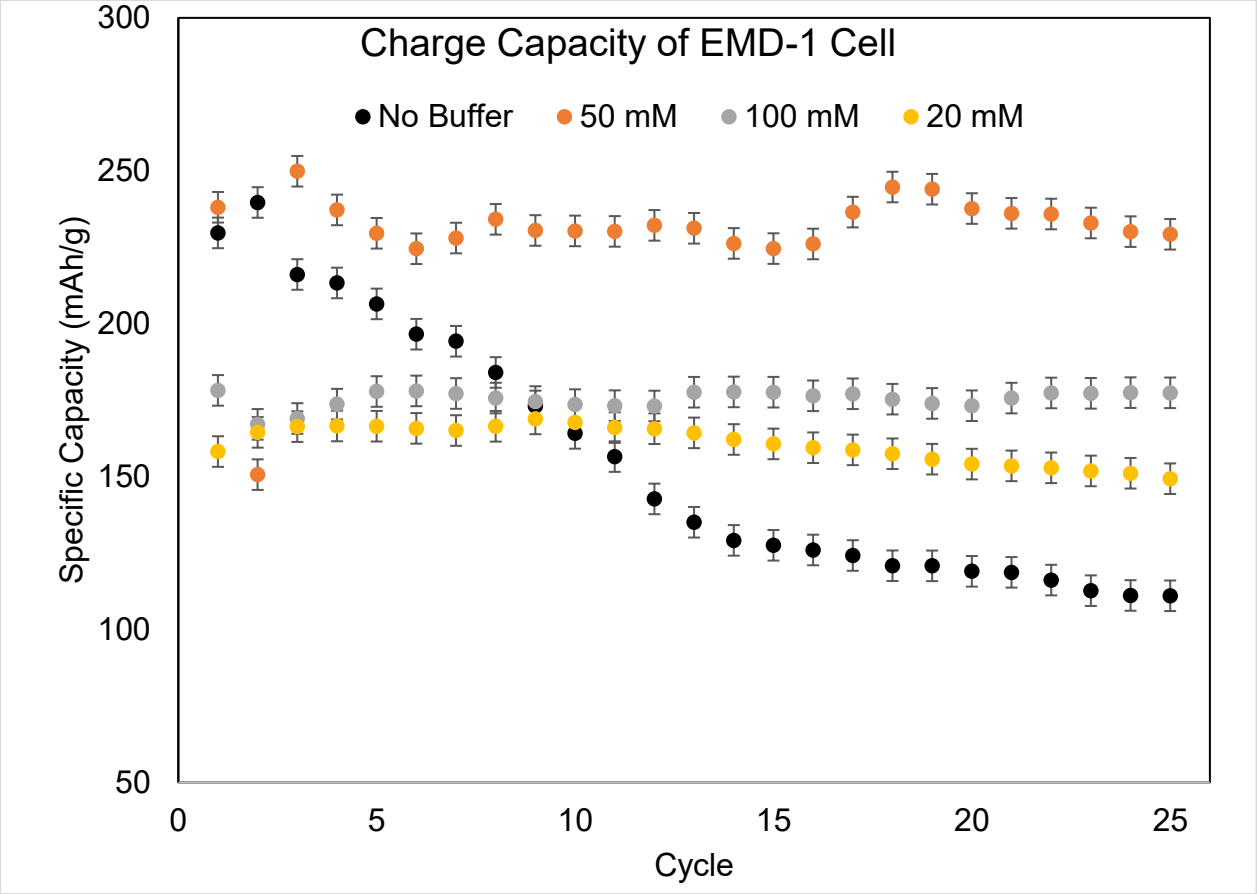

Figure 17 GCD testing of EMD-1 charge capacity, buffered (50 mM NHP & 5 mM HAc) group exhibited similar trend as seen in discharge capacity.

These figures indicated that presence of buffer additives in the cell improved early-stage cell performance in terms of capacity and retention. The capacity fade was observed by comparing buffered groups to unbuffered groups. Presence of buffer additives enhanced capacity by minimum 20% or higher in EMD-1 groups.

3.3.2. Results discussion

In summary, the capacity experiment determined that the presence of buffer additives enabled overall capacity enhancement, while the retention remains higher in buffered groups. The enhancement achieved is higher than 20% while we all

observed some capacity decay in the cell. These experiments validated the effect of buffers in aqueous electrolytes.

3.4. CV

3.4.1. Cyclic Voltammetry Overview and Redox Behavior of MnO_2

Cyclic voltammetry (CV) was performed on assembled cells to evaluate the redox behavior of the active MnO_2 material. To evaluate the influence of scan rate on cyclic voltammetry (CV) response, measurements were performed on a selected functional EMD-1 cell cycled for 25 times across a range from 0.1 to 10 mV s^{-1}. The detailed scanned results are shown in **Figure *18***.

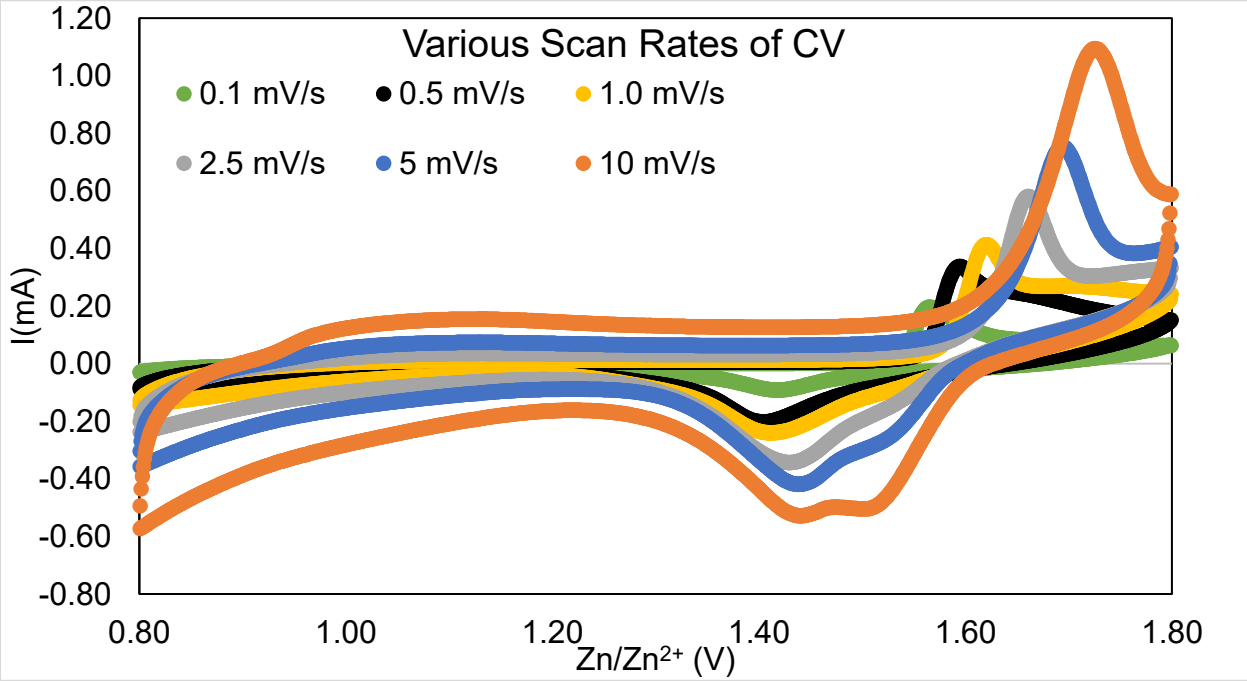

Figure 18 Rate-impacted CV scan of a reference EMD-1 cell (after 25 complete cycles).

As expected, the scan rate imposed a significant effect on current intensity and peak separation. Higher scan rates produced proportionally larger current responses, consistent with scaling with sweep speed. However, this high rate-scan also introduced distortion in the tail regions of the voltammograms and broadened peak features, reflecting increasing kinetic limitations and partial suppression of diffusion-controlled processes. Conversely, very low scan rates yielded well-defined but weak current responses, extended experimental times, and greater relative error in numerical integration when capacitance was calculated.

Despite these differences in peak intensity and resolution, no additional redox couples were observed across the tested scan rates, confirming that the scan-rate difference would not induce peak splitting or peak converging, nor would it alter redox couples in the system. Thus, the main consideration in scan rate selection was to balance clarity, quantitative reliability, and practical acquisition time.

Based on these factors, a scan rate of 2.5 mV s^{-1} was adopted as the standard condition for all subsequent CV experiments. This intermediate rate provides sufficient signal-to-noise ratio for robust charge integration while minimizing distortions associated with either extremely fast or slow scans. Moreover, the chosen rate falls within the range commonly reported for aqueous battery systems (0.2–5 mV s^{-1}) [2] , ensuring consistency with established literature practices. Application of a single scan rate across all measurements further ensures direct comparability of capacitance and cycling trends between buffered and unbuffered cells. Cyclic voltammetry was then conducted on EMD-10-based cells using the optimized scan rate. Both buffered and unbuffered systems were tested immediately

after assembly to evaluate their initial redox responses. The resulting voltammograms are presented below:

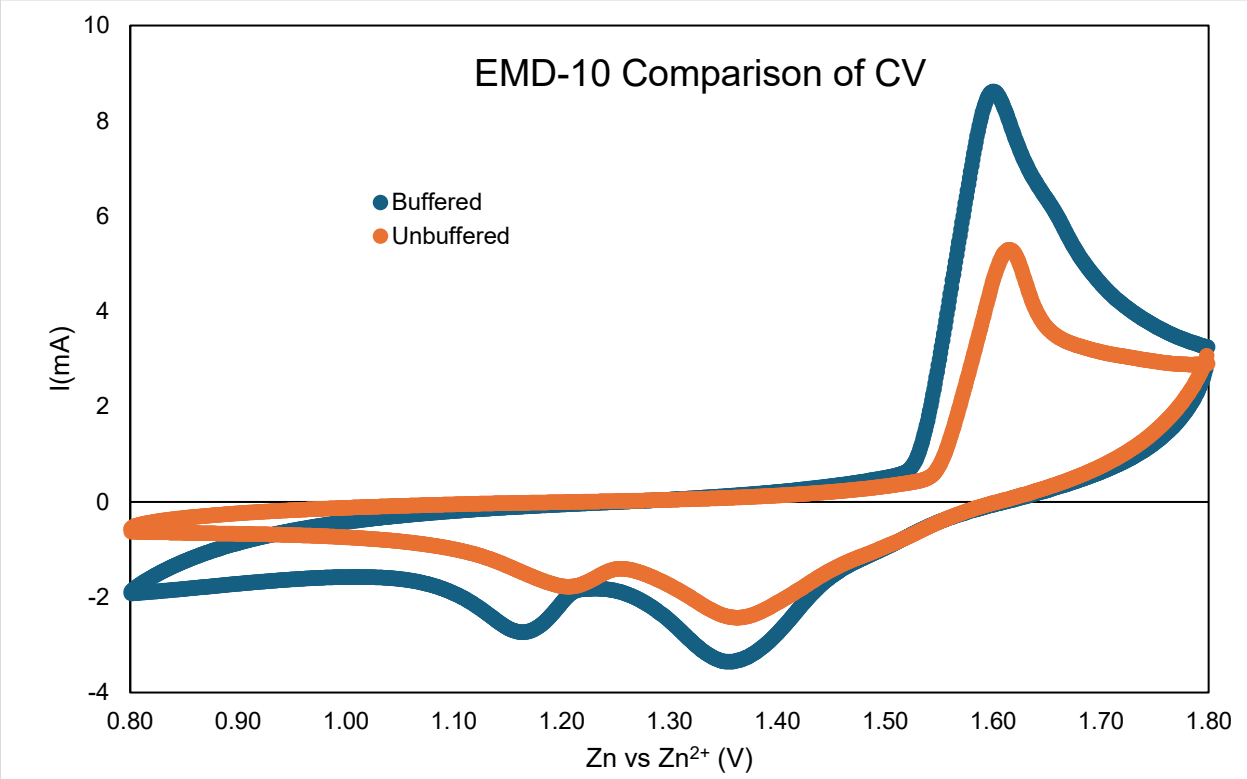

Figure 19 CV comparison of EMD-10 cells at pristine state, before cycling. Data collected under identical conditions. Cathodic peak shift of Mn (IV) to Mn (III) has changed significantly, while other cathodic and anodic peak shift remains very small. The peak separation remains clear, despite ΔV changes among buffered and unbuffered cells. Data collected under identical assembly with same loading provided.

Table 2 Summarized ΔV for EMD-10 Cells

EMD-10 Peaks [4]	Buffer	No Buffer	ΔV
Peak 1 (Mn (III)→Mn (IV) Oxidation)	1.60 V ± 0.05 V	1.62 V ± 0.05 V	0.02 V
Peak 2 (Mn (IV)→Mn (III) Reduction)	1.35 V ± 0.05 V	1.36 V ± 0.05 V	0.01 V

Peak 3 (Mn (IV)→Mn (III) Reduction with Mn (III) Disproportionation → Mn (II))	1.16 V ± 0.05 V	1.21 V ± 0.05 V	0.15 V

The observed redox peaks correspond to known MnO_2 transitions. The broad peak near **1.60 V** is attributed to the oxidation process, while reduction peaks centered around **1.2 V** and **1.4 V** reflect sequential Mn (III)/Mn (II) transitions. These features are consistent with the multi-step redox behavior of MnO_2 as described in Chapter 2. The presence of well-defined and symmetric peaks in both groups indicates successful electrode activation and no evidence of major assembly defects or short circuiting. The observed peak shift indicated that potential difference in ionic strength in the buffered and unbuffered environment may already resulted in early Mn dissolution.

A parallel set of CV experiments was performed on EMD-1-based cells using the same measurement conditions. Similar trends are observed compared to EMD-10 cells. The results are shown below:

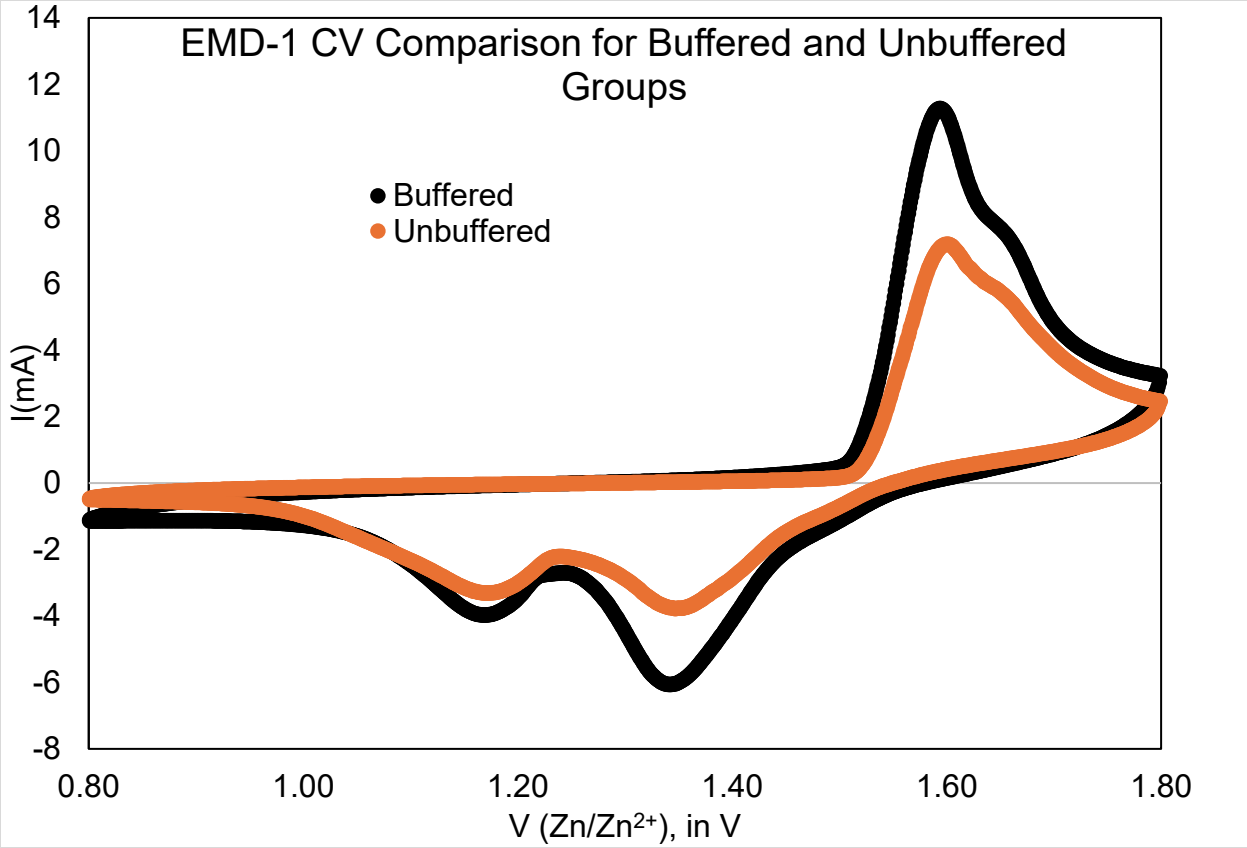

Figure 20 CV comparison of EMD-1 cells at pristine state, before cycling. Data collected under identical conditions with comparable loadings. The table below showed each ΔV.

Table 3 Summarized ΔV for EMD-1 Cells

EMD-1 Peaks [4]	Buffer	No Buffer	ΔV
Peak 1 (Mn (III)→Mn (IV) Oxidation)	1.59 V ± 0.05 V	1.60 V ± 0.05 V	0.01 V
Peak 2 (Mn (IV)→Mn (III) Reduction)	1.34 V ± 0.05 V	1.35 V ± 0.05 V	0.01 V
Peak 3 (Mn (IV)→Mn (III) Reduction with Mn (III) Disproportionation → Mn (II))	1.17 V ± 0.05 V	1.16 V ± 0.05 V	0.01 V

The voltammograms show similar redox features to the EMD-1 group, though peak intensity and separation may vary due to differences in electrode formulation or morphology. These measurements confirm that both buffered and unbuffered cell

types exhibit functional Mn-based redox activity and establish a basis for further comparison of kinetic and capacitive behavior. Given the figures, it can be inferred that buffer additive is functional in electrochemical terms.

The aqueous zinc–manganese dioxide (Zn–MnO_2) battery relies on the complementary electrochemical processes of Zn metal deposition/dissolution at the anode and Mn-based redox transformations at the cathode. Each part of the cell undergoes reactions separately. [5]

In anode (metallic Zn), the reaction responsible for cycling is mostly zinc reversible reactions, demonstrated in *Table 4*.

Table 4 Anode reaction of aqueous Zinc-ion battery

	Discharge	Charge
Anode	$Zn(s) \xrightarrow{Discharge} Zn^{2+} + 2e^-$	$Zn^{2+} + 2e^- \xrightarrow{Charge} Zn(s)$

For cathode, reaction follows a multiple-step process. The discharge leads to an overall reduction of Mn. Charge process reversed it. The multi-step process is illustrated in Table 5.

Table 5 Tabulated reaction in aqueous zinc ion battery

	Discharge	Charge
Step 1	$MnO_2(s) + H^+(aq) \rightarrow MnOOH(s)$ [proton-coupled electron transfer]	$ZnMnO_2(s) \rightarrow MnOOH(s) + Zn^{2+}(aq) + e^-$ [Reversing Zn intercalation]
Step 2	$MnOOH(s) + Zn^{2+} + e^- \rightarrow ZnMnO_2(s) + H^+(aq)$ [further reduction of Mn with Zn intercalation]	$MnOOH(s) \rightarrow MnO_2(s) + H^+(aq) + e^-$ [Oxidation to Mn^{4+}]
Side Reaction	$2Mn^{3+} \rightarrow Mn^{2+} + Mn^{4+}$ [Mn^{3+} disproportionation]	N/A
Overall	$Zn + MnO_2(s) \rightarrow ZnMnO_2(s)$	$ZnMnO_2(s) + Zn^{2+} \rightarrow 2Zn\ (s) + MnO_2(s)$

Notably, zinc hydroxysulphate, a significant byproduct is likely to form during discharge when local OH^- concentration rises (due to Mn redox and/or HER) and reacts with Zn^{2+} and SO_4^{2-}. Accumulation of such product may passivate the cell and lead to decrease of capacity. This formation is very pH-dependent as some of it will be reversible. [5] The formation formula is attached as below.

Equation 7 Formation of zinc hydroxysulphate under basic condition.

$$4Zn^{2+} + SO_4^{2-} + 6OH^- + xH_2O \rightarrow Zn_4(OH)_6SO_4 \cdot xH_2O$$

3.4.2. Redox Interpretation of MnO_2

The cyclic voltammograms above based on MnO_2 electrodes show multiple redox peaks corresponding to the stepwise redox transitions of manganese species. A prominent anodic peak observed near 1.60 V (vs. Zn/Zn^{2+}) is attributed to the oxidation of Mn (III) to Mn (IV), while the corresponding cathodic peak near 1.20–1.30 V indicates the reduction of Mn (IV) to Mn (III). A second cathodic feature around 1.35–1.40 V is commonly associated with the Mn (III) to Mn (II) transition, reflecting further reduction processes that may occur under deeper discharge.

These redox processes are characteristic of electrochemically active MnO_2 in aqueous electrolytes, where the Mn oxidation states shift reversibly during charge–discharge. The changes in voltage shift (ΔV) and peak separation provide insight into the reaction kinetics and reversibility: narrower peak separations suggest faster charge transfer, while broader or shifted peaks may indicate diffusion-limited behavior or irreversible reactions.

The peaks intensity indicated that in both materials tested, buffer increases the intensity of cathodic and anodic sweep. This may function as an indicator to track reaction activities, dissolution and disproportionation,

3.4.3. Peak reversibility

Peak reversibility in cyclic voltammetry is a critical indicator of electrochemical reaction efficiency and stability. Well-defined and symmetric anodic and cathodic peaks, with minimal peak separation (ΔV), suggest fast electron transfer and high redox reversibility. In contrast, broad or shifted peaks may reflect sluggish kinetics, irreversible side reactions, or structural degradation. In the context of MnO_2-based systems, improved peak reversibility implies more stable redox cycling of manganese species, reduced dissolution, and enhanced reaction fidelity—especially in buffered environments where interfacial pH is better controlled. Given that Mn oxidation transition is not coupled, observed peaks would differ in terms of position and numbers.

3.5. Summary of key findings.

These results suggest buffer improved long-term stability and capacity. The redox chemistry remains similar among buffered and unbuffered groups, leading to a mechanistic investigation in Chapter 4.

3.6. References

[1] Christian Friedrich Bischoff *et al* 2020 *J. Electrochem. Soc.* **167** 020545

[2] Nano Lett. 2018, 18, 3, 1758–1763

[3] Conway, B. E. Electrochemical Supercapacitors; Springer Nature, 2013.

[4] Zhang, W.; Dai, Y.; Chen, R.; Xu, Z.; Li, J.; Zong, W.; Li, H.; Li, Z.; Zhang, Z.; Zhu, J.; Guo, F.; Gao, X.; Du, Z.; Chen, J.; Wang, T.; He, G.; Parkin, I. P. Highly Reversible Zinc Metal Anode in a Dilute Aqueous Electrolyte Enabled by a Ph Buffer Additive. *Angewandte Chemie* **2022**, *135* (5).

[5] Pan, H.; Shao, Y.; Yan, P.; Cheng, Y.; Han, K. S.; Nie, Z.; Wang, C.; Yang, J.; Li, X.; Bhattacharya, P.; Mueller, K. T.; Liu, J. Reversible Aqueous Zinc/Manganese Oxide Energy Storage from Conversion Reactions. *Nature Energy* **2016**, *1* (5).

Chapter 4: Mechanistic Understanding of Buffer-Enhanced Electrochemical Performance

4. Attempt to Unravel Mechanistic Explanation

4.1. Capacity Enhancement may Occur due to Suppressed Dissolution of Cathode

The discharge capacity of aqueous Zn–MnO_2 cells is primarily governed by the available amount of electrochemically active MnO_2 retained within the cathode. A consistent observation across cycling is that cells containing buffered electrolytes exhibit higher specific capacity and better retention than their unbuffered counterparts. One plausible explanation is that cathode dissolution is suppressed by the presence of buffering additives.

This approach of mechanistic explanation may be counterintuitive due to the fact that buffering effectively increases the acidity of electrolyte. From Pourbaix diagram, it is inferred that MnO_2 is thermodynamically instable and more soluble at lower pH. From this point, dissolution control of active materials may not be the major cause of capacity enhancement and retention.

Experimentally, direct measurement of the cathode's residual MnO_2 during operation is not feasible, as the electrode undergoes continuous transformation in situ. However, the extent of dissolution can be inferred indirectly by quantifying Mn^{2+} concentrations in the electrolyte. To achieve this, NMR relaxometry offers a suitable probe. Properly calibrated one-dimensional nuclear magnetic resonance (1-D NMR) experiments allow back-calculation of the dissolved Mn fraction, thus reflecting the material lost from the solid cathode.

Before applying NMR relaxometry, validation of method effectiveness had to be established, that the differences in the buffered additive spiked electrolyte and baseline no buffer electrolyte may result variations in NMR responses. As a result, comparative baseline experiments of buffer solution, spiked electrolyte and unbuffered electrolyte were conducted with the results showing that buffer do not alter chemical shift of proton in water in the electrolyte prepared (50 mM NHP, 5 mM HAc dissolved in 1 M $ZnSO_4$ (aq)). Thus, in-situ and operando experiments can be conducted with no interference or internal reference standard.

The major technique to correlate Mn concentration to NMR observation is completed by applying T_1 inversion–recovery (T_1IR) experiments. The experiment follows a flow chart as below.

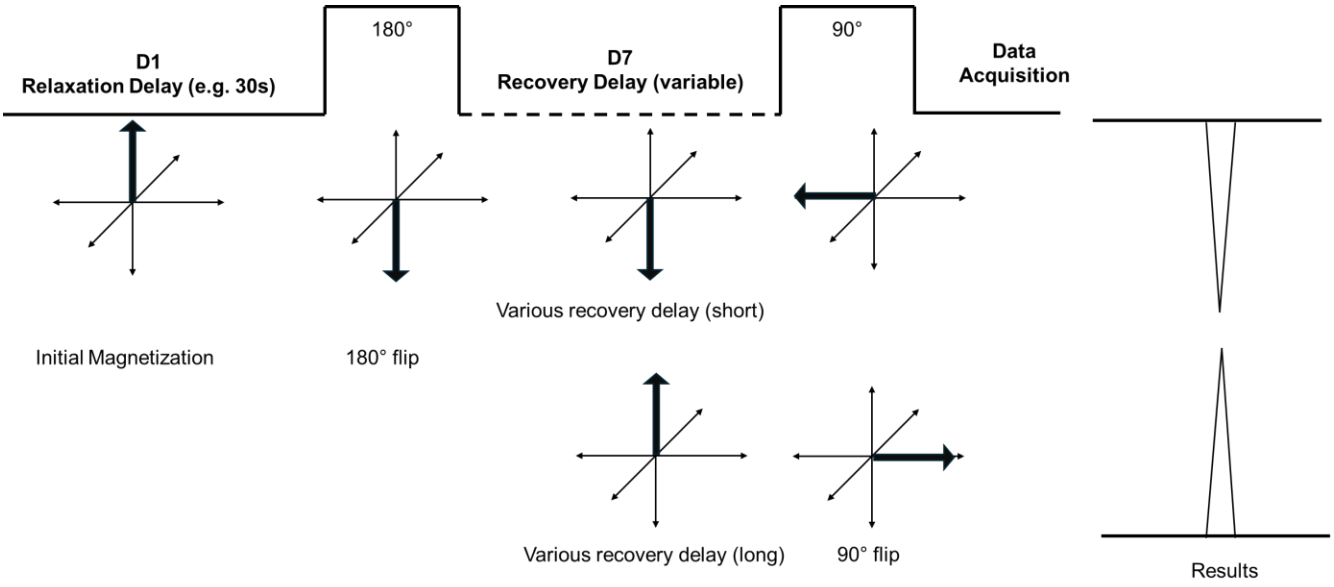

Figure 21 Mechanistic illustration of T_1IR experiment. A special pulse sequence is applied to the sample causing an 180° flip in magnetization. Various delays are applied to the sample, causing it to naturally recover to magnetization. The following 90° pulse is applied against the sample after various length of recovery delay, leaving it on a 90° flip. Spectral acquisition is completed after that. Depending on the recovery delay applied, the

spectra would have various shapes. The data processing to obtain T_1 is demonstrated in following paragraph. Figure created with respect to reference[10] [6]

Following various delay times applied, the determination of T_1 follows the equations listed below. The signal detected after variable delay obeys the equation below.[10] [6]

$$M_z(\tau) = M_0(1 - 2e^{-\frac{\tau}{T_1}})$$

Equation 8 The description of signal after variable delay. $M_z(\tau)$ is the longitudinal magnetization at time τ. M_0 is the equilibrium magnetization. T_1 is the longitudinal relaxation time, while the τ is the various delay time applied between 180° and 90° pulses.[10] [6]

After the 90° pulses, signal decay is fitted into equation as follows to extrapolate the T_1.

$$I(\tau) = A(1 - 2e^{-\frac{\tau}{T_1}})$$

Equation 9 Fitting equation for extrapolating T_1 time. $I(\tau)$ is the signal intensity, while A is the scaling constant. Computation takes signal intensity by manual integration.[10] [6]

T_1 is not direct solvable factor to the concentration of Mn in electrolyte, in experiment, its inverse, R_1 is used.

$$R_1 = \frac{1}{T_1}$$

Equation 10 Determining R1 from T_1.

Utilizing the equations and principles, relaxation experiments were performed on a Bruker Avance 300 MHz NMR spectrometer. The observed spin–lattice relaxation times were correlated with Mn^{2+} concentrations using experimentally determined calibration curves (Figure 26). The determination of percentage of Mn dissolution follows the flow chart demonstrated in Figure 27.

The experiments began with cell-building. A two-piece Teflon cartridge cell with plastic screw was obtained. Each cell component (cathode, anode and separator) was cut using

rectangular mold. Then, each piece is assembled into a complete cartridge cell following the same method of assembly as coin cell.

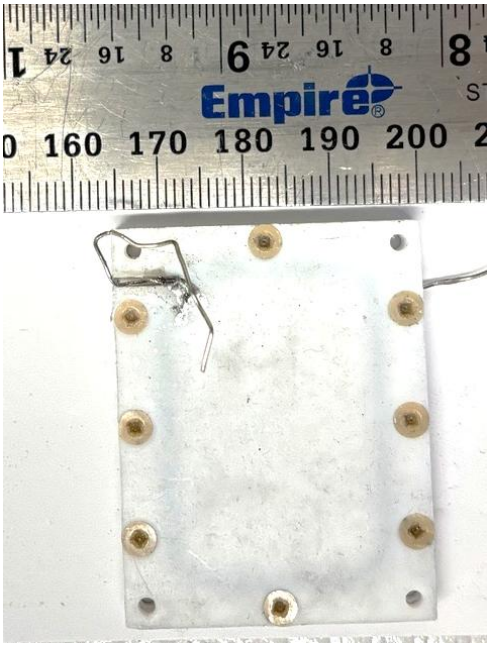

Figure 22 Figure of assembled cartridge cell.

After that, the cell is installed to probe, mounted using titanium wire. Experiment begins collecting spectra. The detailed experimental outlook is shown as in Figure 23.

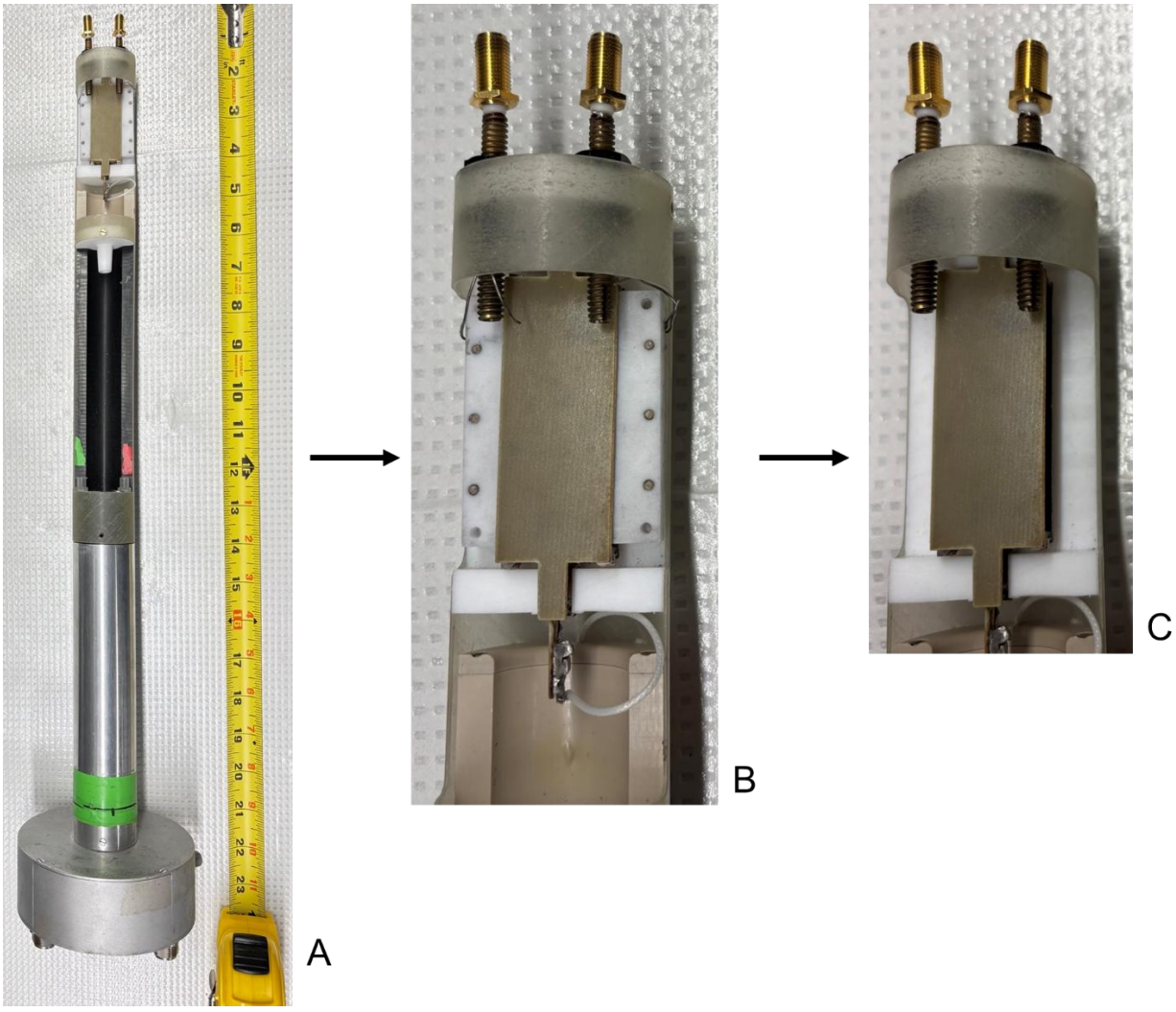

Figure 23 Illustration of NMR probe installation. (A) an overview of the probe being used. (B) and (C) showed the zoomed-in view of the cell installation. Assembled cartridge cells are installed between two parallel plate resonators hitched by titanium wires.

Over time, the 1-D 1H NMR of the electrolyte in the operando cell had spectra broadening and peak splitting, indicated that some irreversible Mn-dissolution occurred in the cell. The snapshot of 1D results is attached in Figure 24.

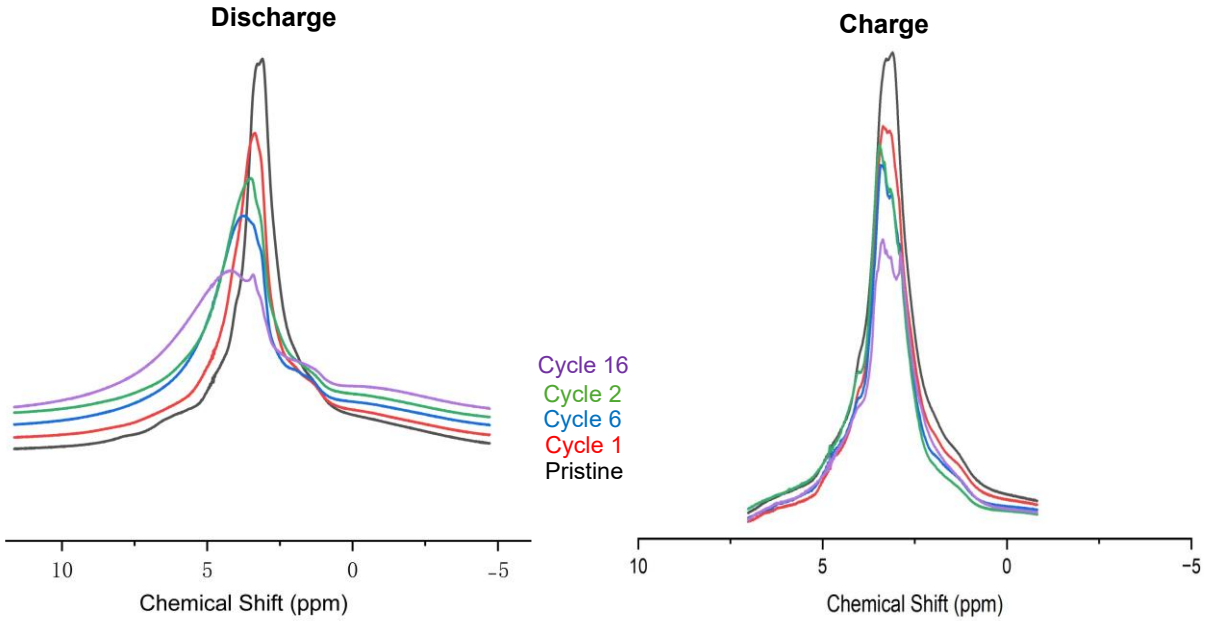

Figure 24 The 1-D snapshot of electrolyte after charge and discharge. The peak broadening and splitting indicated irreversible Mn dissolution into electrolyte.

The 1-D NMR spectra of cell are collected periodically, to observe if any changes occurred.

From the 1-D spectra, T_1 calculation is conducted as Equation 9, fitting using Bruker Topspin software. An exemplary fitting on software is shown as in Figure 25.

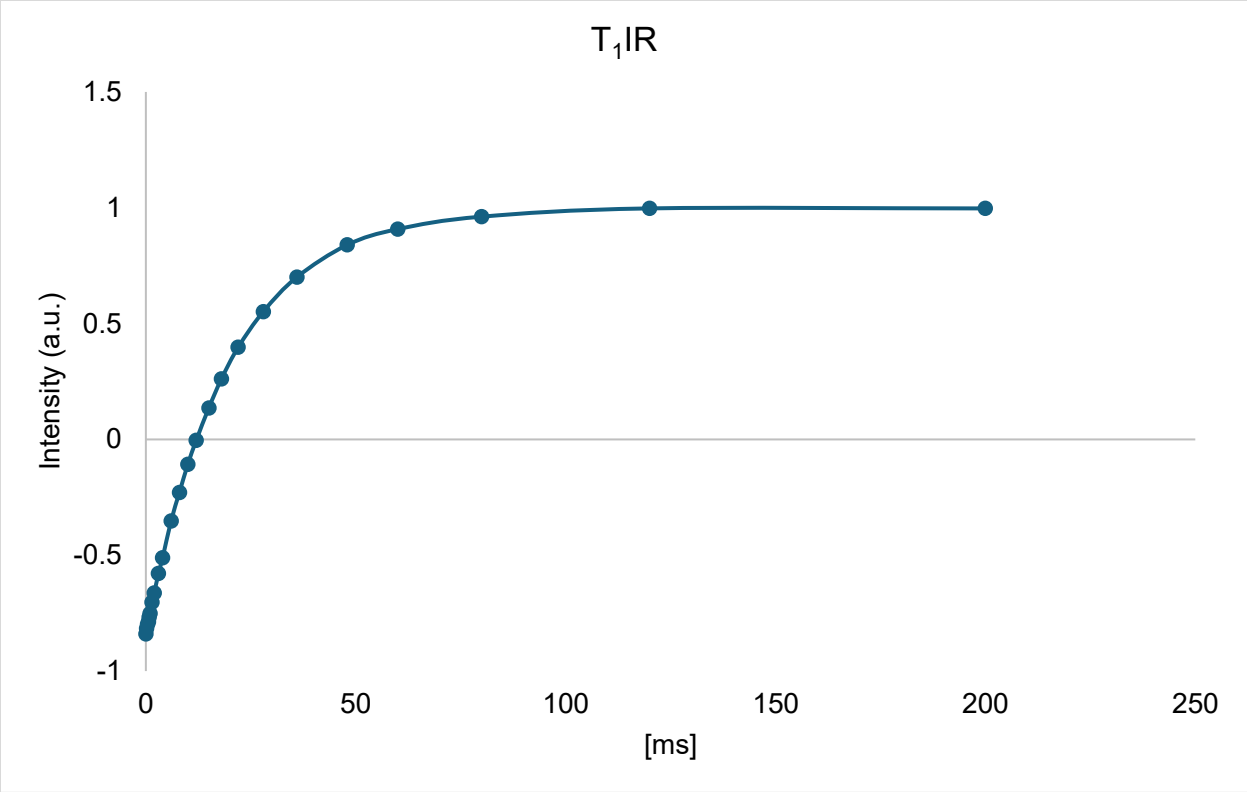

Figure 25 An example of T_1IR fitting to extrapolate T_1 relaxation time using **Equation 9**.

From the calculated T_1, R_1 is determined, and the concentration of $[Mn^{2+}]$ is calculated using previously established calibration curve, as shown in Figure 26.

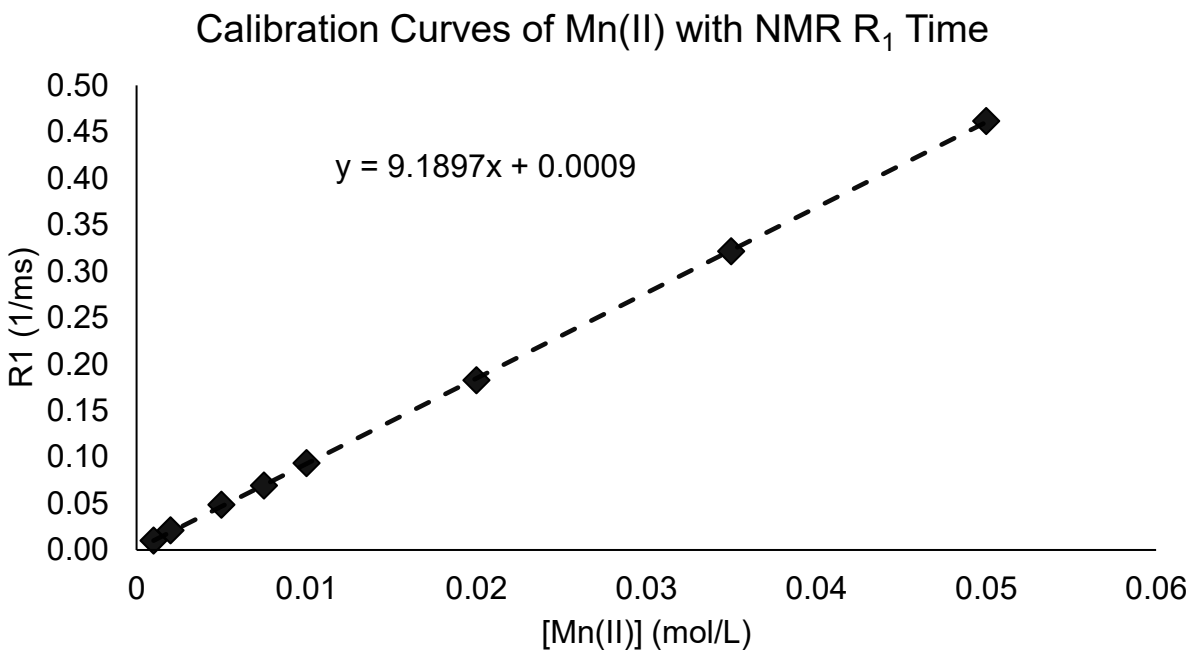

Figure 26 Experimentally determined calibration curve of Mn concentration with R_1.

Based on the concentration determined from Figure 26, the percentage of Mn dissolution from cathode is determined using flow chart illustrated in Figure 27.

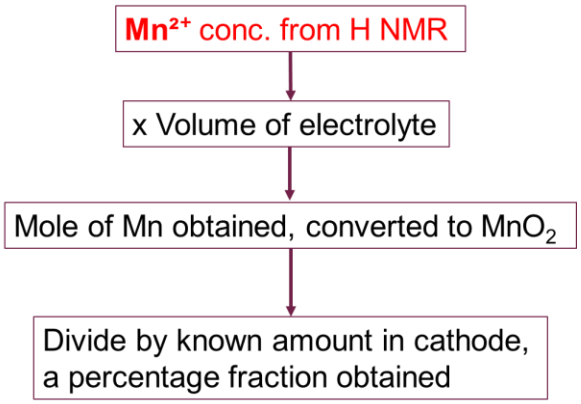

Figure 27 The flowchart of determining percentage of Mn dissolution from electrode.

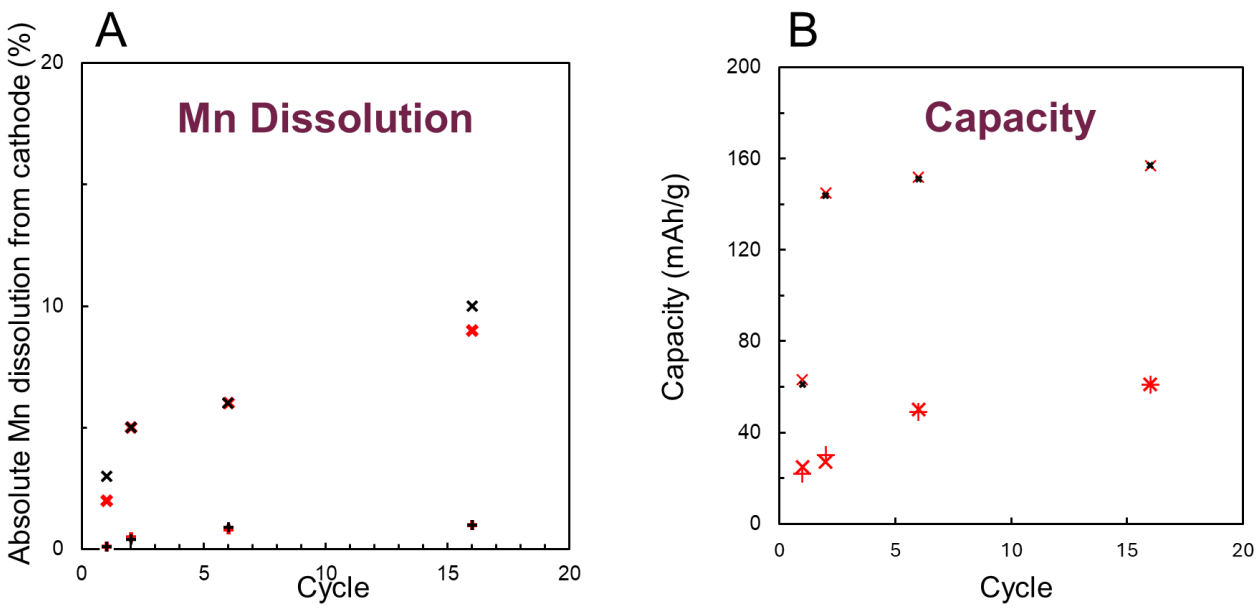

Figure 28 (A) Mn dissolution percentage as a function of cycle number. (B) Cell capacity as a function of cycle number. In both panels, **charge** (solid symbols "+") and **discharge** (cross symbols "×") are shown for **buffered cells** (black) and **unbuffered cells** (red).

Based on the flowchart, percentage of Mn dissolution and individual cycle-dependent capacity is determined between buffered and unbuffered cells, while the results showed that the percentage of Mn on cathode leaching into electrolyte remains similar among buffered and unbuffered groups, but capacity enhancement is significant. The capacity plot resembles similar experiment done in GCD testing.

Although no dedicated dissolution-control experiment was performed, the buffered vs. unbuffered comparison reveals that buffering does not have any effect on reducing Mn leaching. Mechanism of charge and discharge appeared to be similar in both buffered and unbuffered cell, while capacity enhancement and performance improvement possibly arise from anode improvement [16], while other experiments would help understanding the root causes.

4.2. Morphological Information from Cathode

As discussed in section 4.1, no strong evidence indicates that suppressed cathode dissolution contributed to the capacity enhancement observed in buffered cells. Therefore, alternative approaches were taken to investigate cathode changes in terms of morphology and structural features. Cells were disassembled to separate the electrodes, and cathodes were collected and air-dried before analysis. SEM imaging was carried out at the Canadian Centre for Electron Microscopy (CCEM) using the FEI Magellan 400 instrument, with individual imaging parameters provided in the corresponding result figures.

The pristine cathode of EMD-10 (Figure 29) and EMD-1 (Figure 30) were collected for imaging analysis prior to cycling.

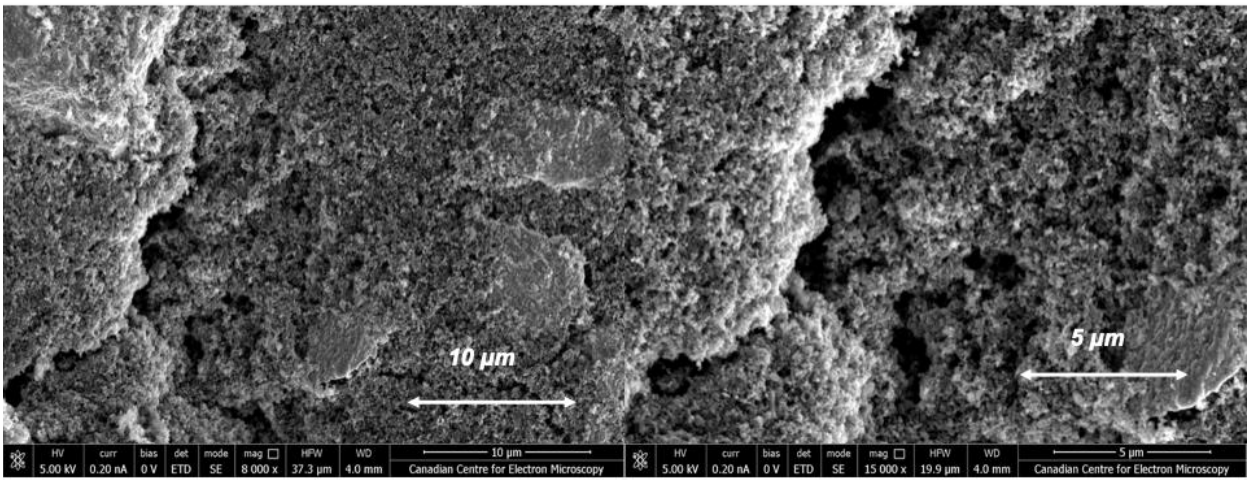

Figure 29 SEM image of pristine EMD-10 based cathode, global (L) and local view (R).

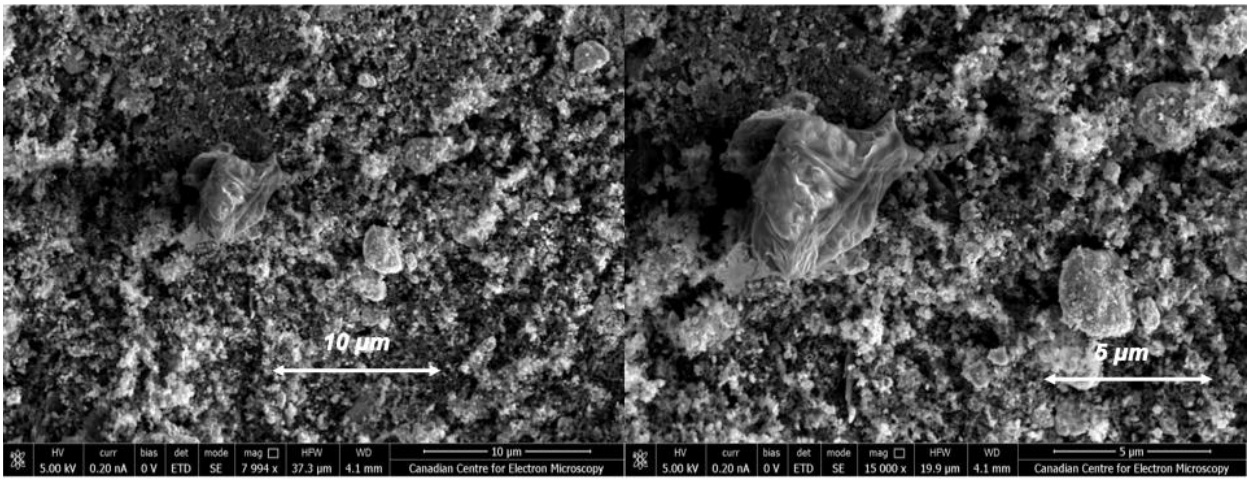

Figure 30 SEM image of pristine EMD-1 based cathode on global (L) and local (R) view.

An overview of morphology of both cathodes exhibited a relatively uniform surface with no observed distortion. This observed morphology serves as the baseline reference for evaluating structural changes induced by electrochemical cycling.

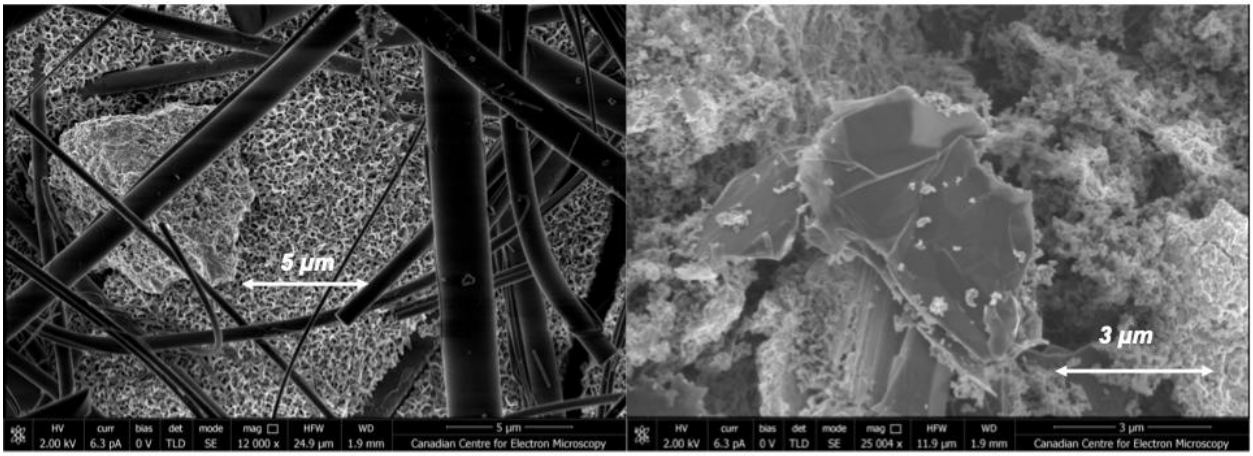

Figure 31 SEM imaging of EMD-10 based cycled cathode (50 cycles) in buffered electrolyte. Snapshot of smaller scaled to 5 and 3 μm. Images collected under identical conditions. The rod-shaped fiber on the left panel was glass fiber unable to be removed.

The SEM image of buffered cathode after cycling of EMD-10 is shown in Figure 31. The observed morphology indicated more open porosity and less deposited complex. This may correspond to lower internal resistance over time as well as stable reaction pathway. While

some mineral deposits are still observed, they did not obstruct active compared with the unbuffered sample. While some degree of surface alteration appeared evident, the overall structural integrity is more stable, accounting for possible capacity retention and enhancement.

Comparatively, unbuffered cells were collected for imaging analysis, with the results shown on Figure 32.

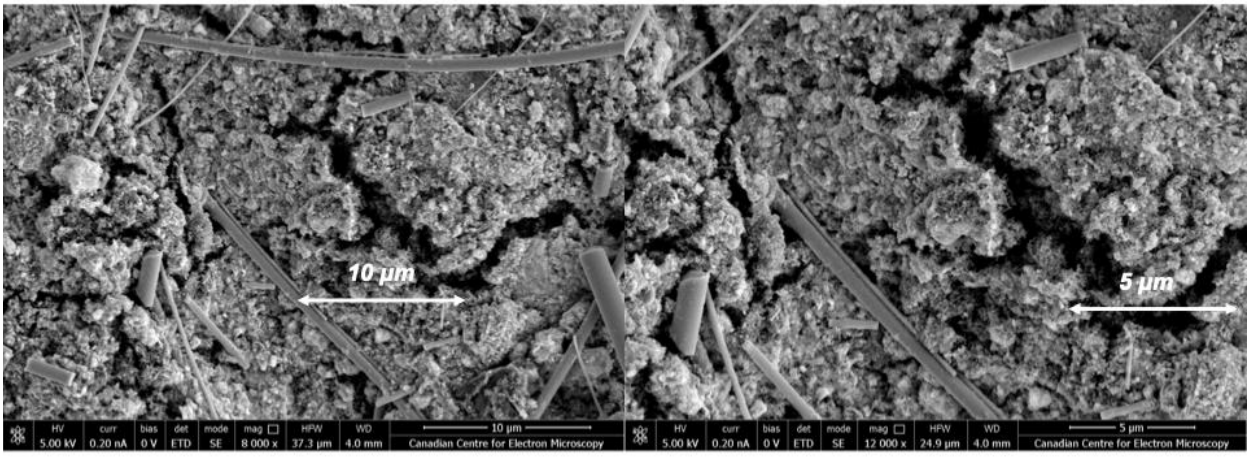

Figure 32 SEM image of EMD-10 based cycled cathode (50 cycles) in unbuffered electrolyte. Snapshots of smaller scaled to 10 and 5 μm. Images collected under identical conditions. The rod-shaped fibers were glass fibers unable to be removed.

Similarly, EMD-1 cathodes cycled under different electrolyte were collected images for analysis, the results are presented in Figure 33 (buffered groups) and Figure 34 (unbuffered groups). The appearance of EMD-1 cathodes differed from that of the EMD-10 materials, possibly as a result due to average particle sizes. The EMD-1 cathodes cycled in unbuffered electrolytes appeared to have patchy surface with less porosity retained as the buffered groups. That may account for the capacity difference between the two.

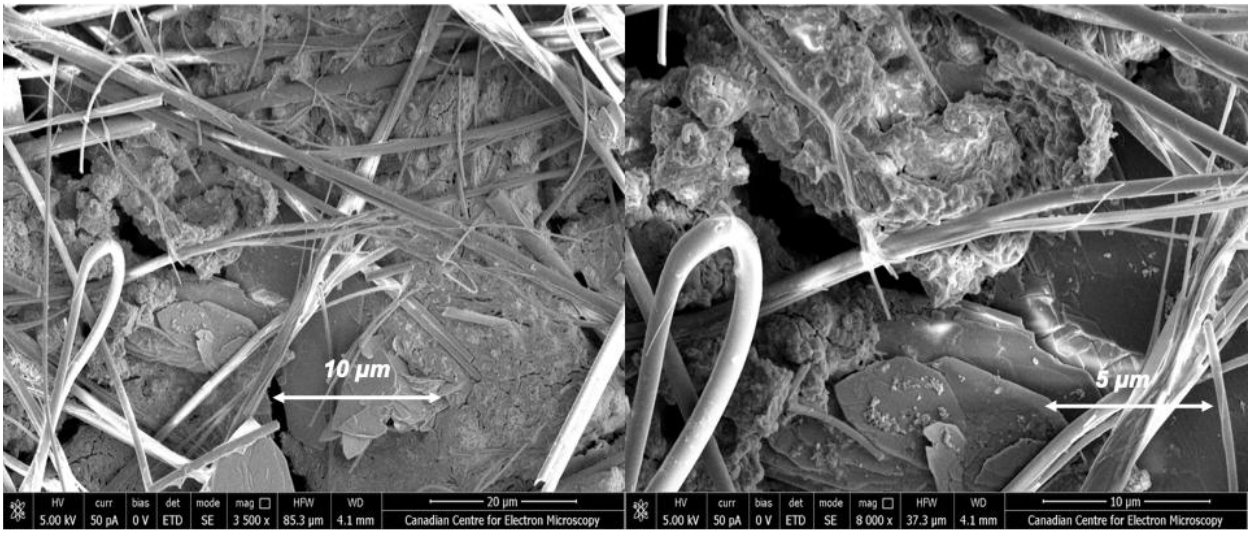

Figure 33 SEM image of EMD-1 based cycled cathode (50 cycles) in buffered electrolyte. Snapshots of smaller scaled to 10 and 5 μm. Images collected under identical conditions. The rod-shaped fibers were glass fibers unable to be removed.

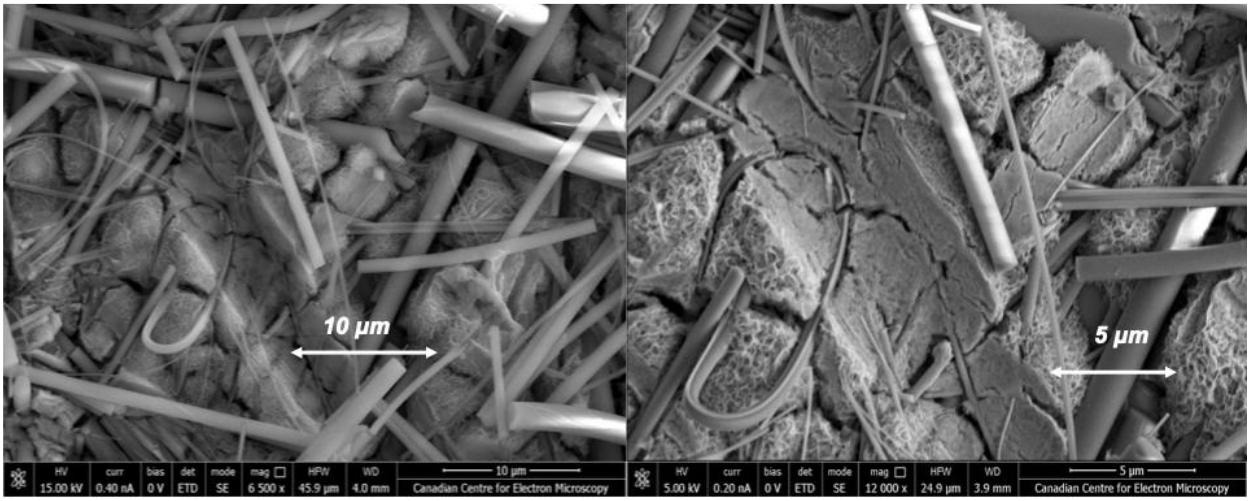

Figure 34 SEM image of EMD-1 based cycled cathode (50 cycles) in unbuffered electrolyte. Snapshots of smaller scaled to 10 and 5 μm. Images collected under identical conditions. The rod-shaped fibers were glass fibers unable to be removed.

In summary, SEM analysis suggests that the improved performance of buffered cells arises not from suppression of MnO_2 dissolution, but from the preservation of cathode morphology during cycling. By maintaining more favorable surface and structural conditions, buffered electrolytes enable continued accessibility of active material and more stable ion pathways, which collectively enhance electrochemical performance.

Morphological information obtained can only partially explain capacity enhancement, the development of capacity enhancement requires further exploration of early-stage cell evolution. Due to that, electrochemical characterizations were conducted to fully unravel the mechanisms.

4.3. Electrochemical Characterization

4.3.1. Capacity-Voltage Information during Cycling

To understand capacity enhancement due to presence of buffer, it is essential to analyze the cycle-dependent evolution of capacity in relation to the corresponding voltage profiles. Under constant-current charging and discharging conditions, the capacity–voltage curve serves as an indicator of the underlying electrochemical processes. Distinct plateau regions are typically associated with Zn^{2+} intercalation into MnO_2 frameworks, whereas gradual slopes may reflect surface adsorption or conversion-type reactions. The stability and shape of the curves across multiple cycles indicate the stability of electrode in electrochemical reactions. The shifts of shape or abrupt turns may indicate some possible side reaction, structural distortion or degradation of electrode.

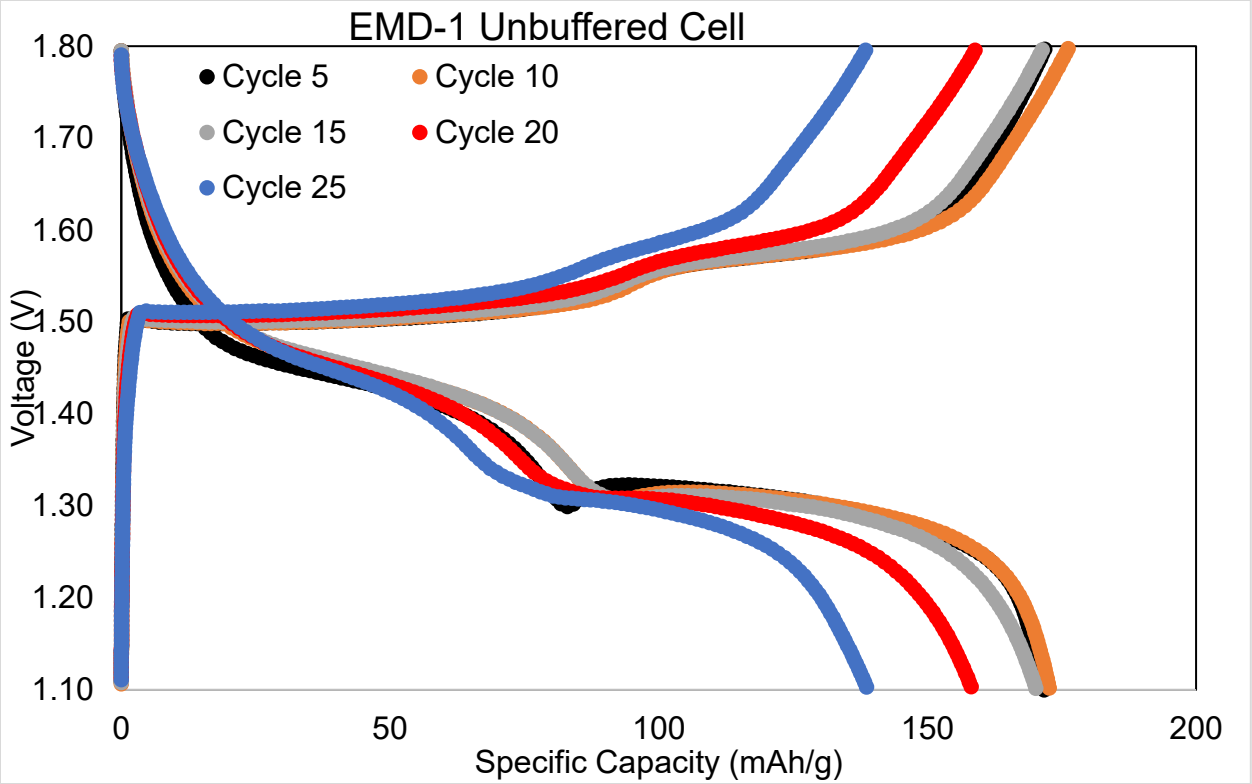

Figure 35 GCD plot of EMD-1 cell in unbuffered electrolyte.

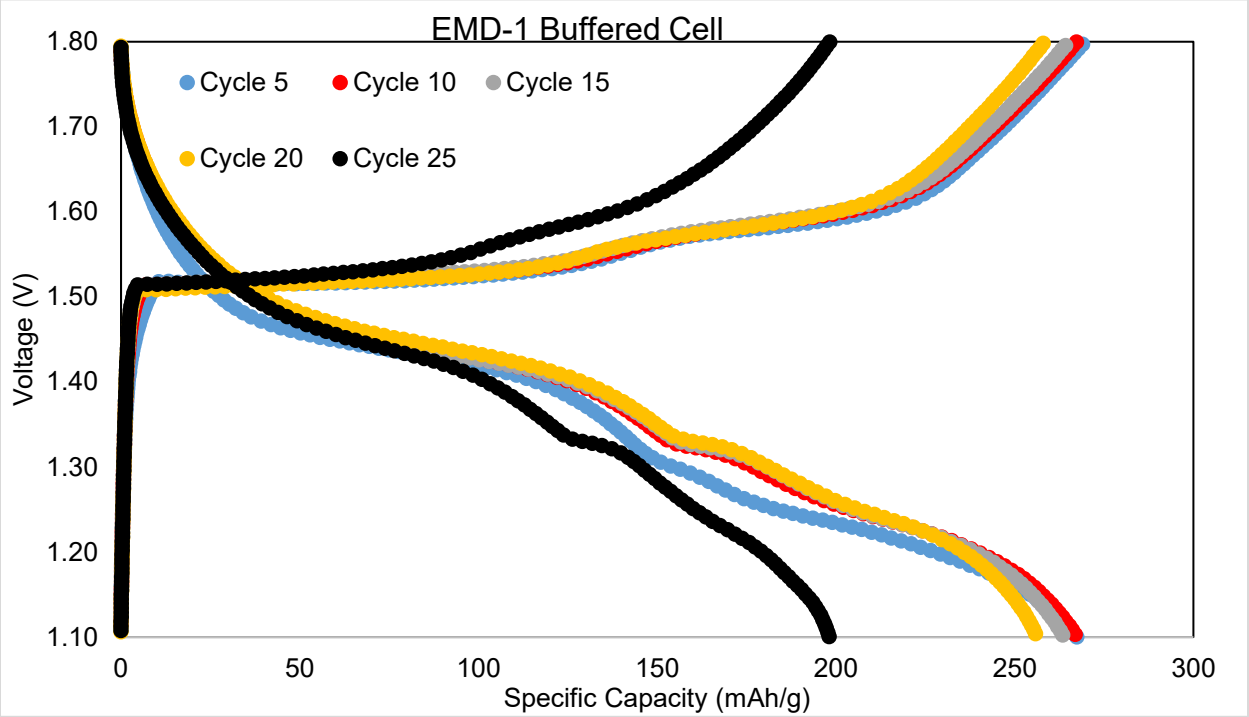

Figure 36 GCD plot of EMD-1 cell in buffered electrolyte.

The capacity–voltage curves of EMD-1 cells showed distinct electrolyte-dependent behaviors. Polarization was quantified as the voltage gap between charge and discharge curves at a fixed capacity point. In the unbuffered group, polarization increased from 0.38 V at 137 mAh g^{-1} (cycle 20) to 0.67 V at the same capacity in cycle 25. In contrast, the buffered group showed a smaller rise, from 0.24 V at 157 mAh g^{-1} (cycle 20) to 0.37 V in cycle 25. These results demonstrate that polarization grows with cycling in both systems, but the increase is mitigated in buffered electrolytes. The lower and more stable polarization observed in buffered cells indicates reduced overpotential buildup and improved interfacial kinetics, consistent with enhanced Mn^{3+} stabilization and suppressed Mn^{2+} dissolution. This highlights the role of buffering in maintaining electrochemical reversibility during extended cycling. The results also showed that charge–discharge plateaus remain

flatter and polarization increases only modestly with cycling. In contrast, unbuffered cells show progressively sloped plateaus and a sharp rise in polarization

This behavior aligns with reported literature where electrolyte buffering reduces local pH fluctuation, suppresses Mn dissolution, and extends the cycle life of aqueous Zn–MnO_2 batteries. [12] [15] [3]

Similarly, the same processing was conducted on EMD-10 samples. The results are shown in Figure 37 and Figure 38.

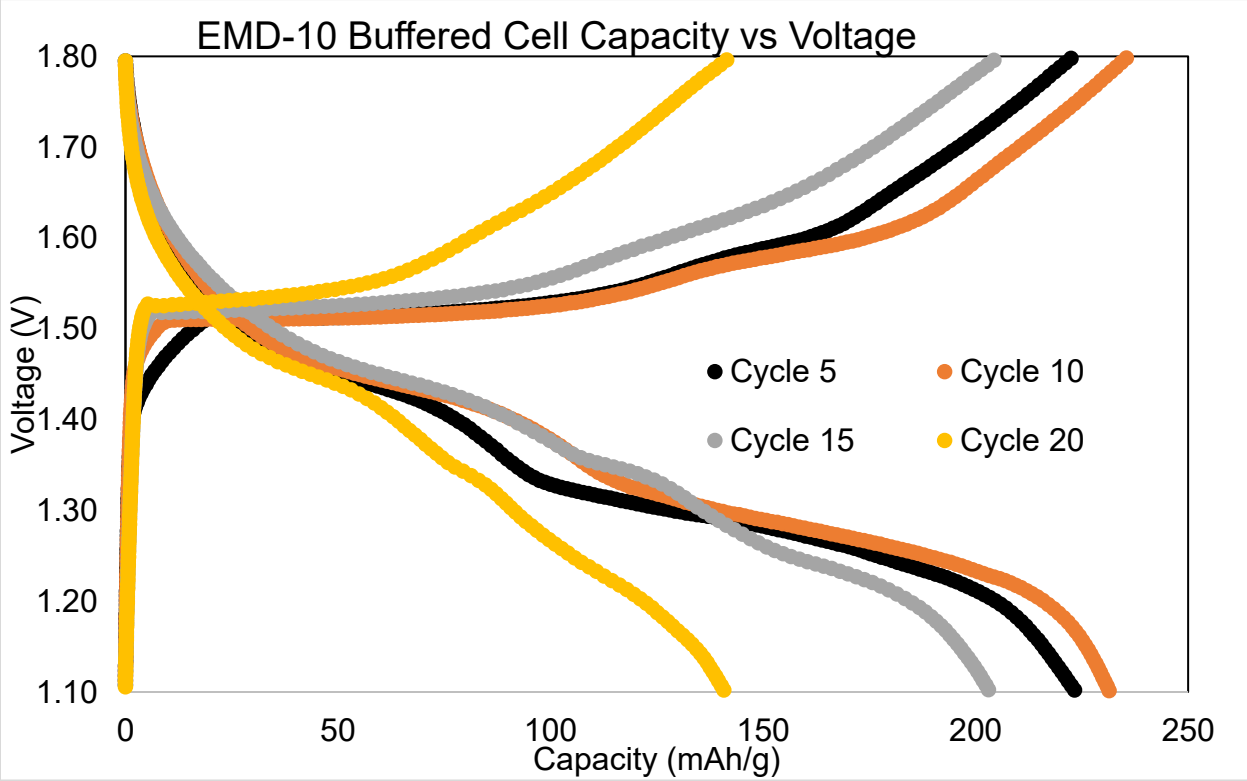

Figure 37 GCD plot of EMD-10 cell in buffer electrolyte.

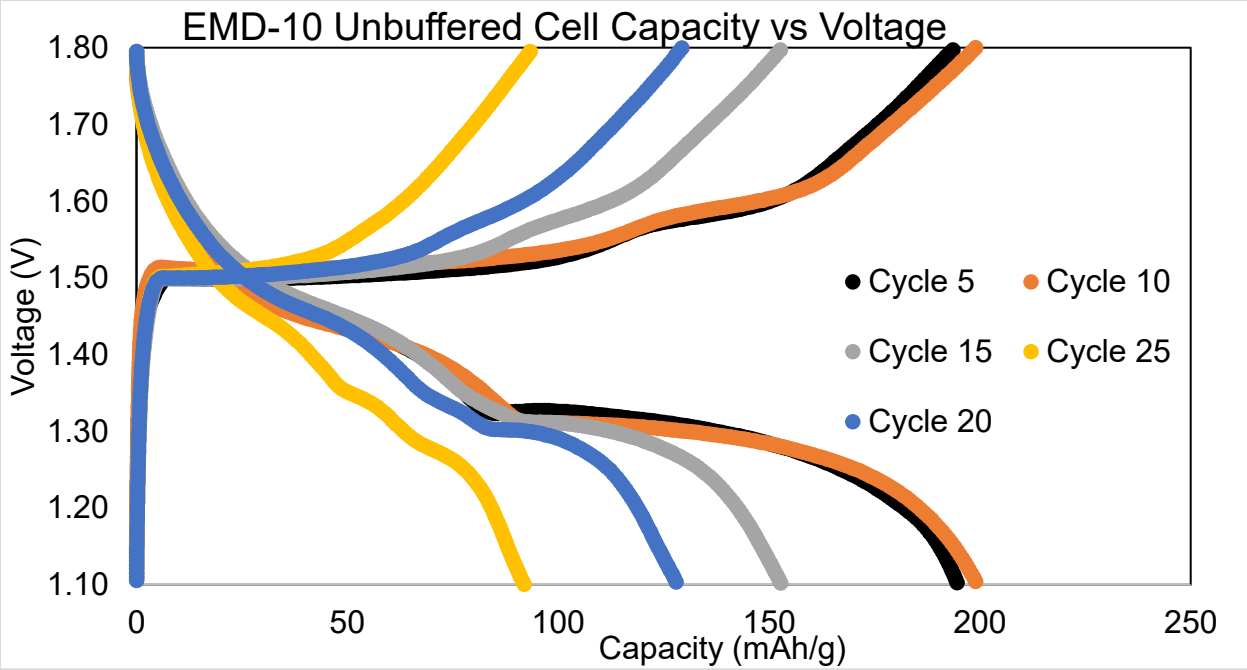

Figure 38 GCD plot of EMD-10 cell in unbuffered electrolyte.

Similar trends were observed in EMD-10 cells compared to EMD-1

Polarization was quantified in EMD-10 cells as well. In the unbuffered group, polarization increased from 0.21 V at 100 mAh g^{-1} (cycle 5) to 0.33 V at the same capacity in cycle 20. In contrast, the buffered group showed a smaller rise, from 0.18 V at 90 mAh g^{-1} (cycle 5) to 0.30 V in cycle 20. It is observed that there is a more modest increase in polarization with cycling than EMD-1 in EMD-10. Some effects of buffering are present and suppressed some polarization, but the effects are very limited due to the intrinsic dissolution drive is lower in the large-particle material.

In buffered electrolytes, EMD-10 cells exhibited relatively smooth and symmetric charge–discharge plateaus, with initial discharge capacities exceeding 200 mAh g^{-1}. Although polarization gradually increased and capacity declined with cycling, the overall curve shape remained stable, indicating preserved MnO_2 redox reversibility.

Even by cycles 15–25, buffered cells maintained well-defined discharge profiles, consistent with partial mitigation of Mn dissolution and structural distortion. In contrast, unbuffered cells showed accelerated polarization growth and rapid capacity fade. While their early cycles occasionally reached comparable capacities, the discharge plateaus became progressively disrupted, and by cycle 20 capacity often fell below 100 mAh g^{-1}. This deterioration reflects the destabilizing influence of local pH shifts and Mn^{3+} disproportionation in unbuffered systems.

Concluding these results, the buffered electrolytes consistently extend the stability window, reducing disruption and improving the reversibility of electrochemical reaction. These results reinforce the broader conclusion that electrolyte buffering is a critical design factor for sustaining long-term Zn–MnO_2 cell operation, that buffered environment favored stable operation. [15] [12]

4.3.2. Full Integration of CV

Cyclic voltammetry experiments were performed using the protocols detailed in Chapter 3, with the goal of tracking the electrochemical evolution of cells from their pristine to cycled states. To visualize time-dependent changes in redox behavior, CV profiles from selected cycles were superimposed for each group, allowing direct comparison of peak intensity, shape, and potential shift over repeated cycling.

For EMD-1 groups, CV plot of buffered electrolytes was repeated and shown in Figure 39.

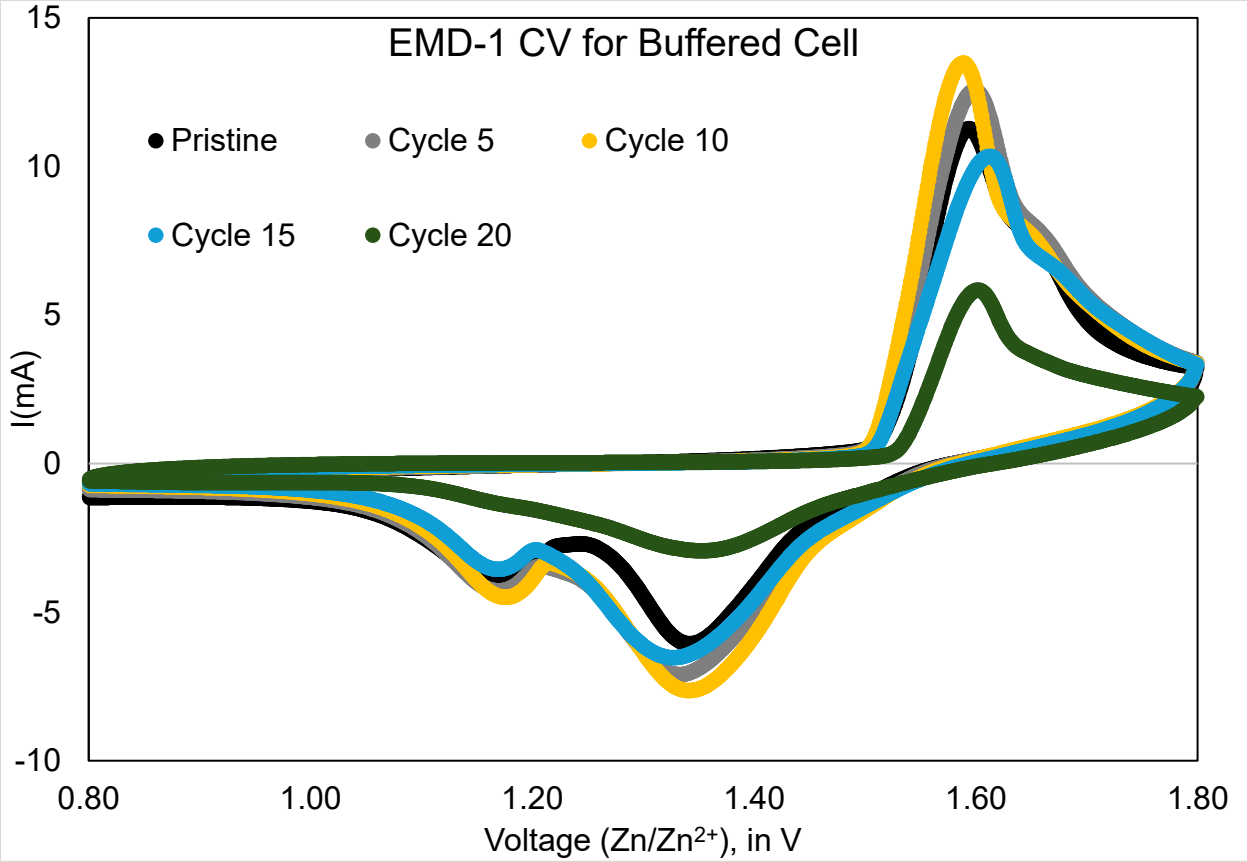

Figure 39 CV comparison of an EMD-1 cell with buffered electrolyte after certain cycles. Collected from pristine state to 25 cycles.

As observed, initial scans of pristine cells showed identical patterns that reduction of Mn is well-observed. However, over extended cycling, the two reduction peaks started to attenuate and eventually one of them disappeared. Similar trends to oxidation peaks that the intensity decreased over cycling. This might be because of several reasons such as (i) conversion of MnO_2 to non-Zn intercalation supporting side produces; (ii) blocks of active materials for subsequent conversion reaction; (iii) formation of different phase MnO_2 which requires confirmation of other experiments.

Compared with unbuffered samples, we can observe similar trends. The unbuffered EMD-1 cells results are shown in Figure 41.

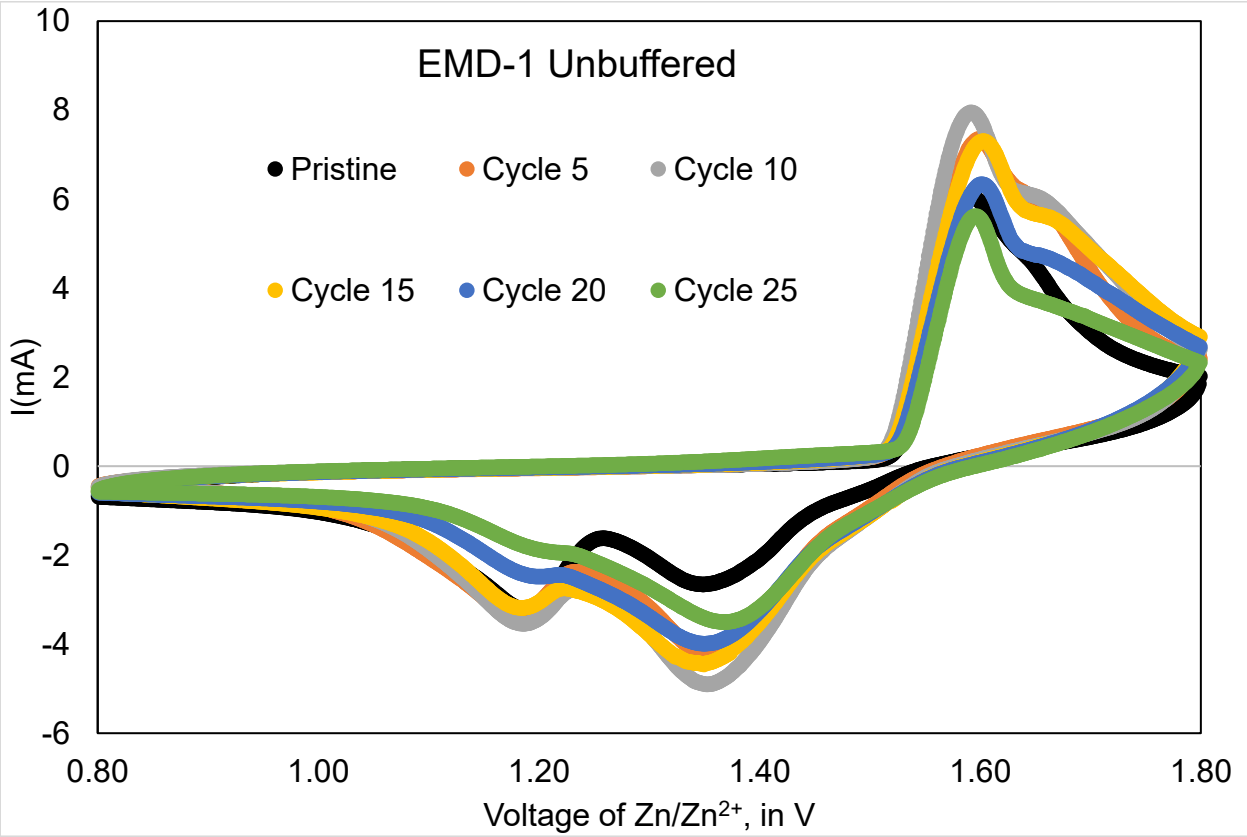

Figure 40 CV comparison of an EMD-1 cell with unbuffered electrolyte after certain cycles. Collected from pristine state to 25 cycles.

Comparing buffered and unbuffered CV scans versus cycles, the results indicated some underlying differences in chemistry. Despite peak attenuation occurred in

For EMD-10 cells, similar work has been done. For analysis, the respective buffered and unbuffered CV charts are placed, detailed results are shown as in Figure 41 and Figure 42.

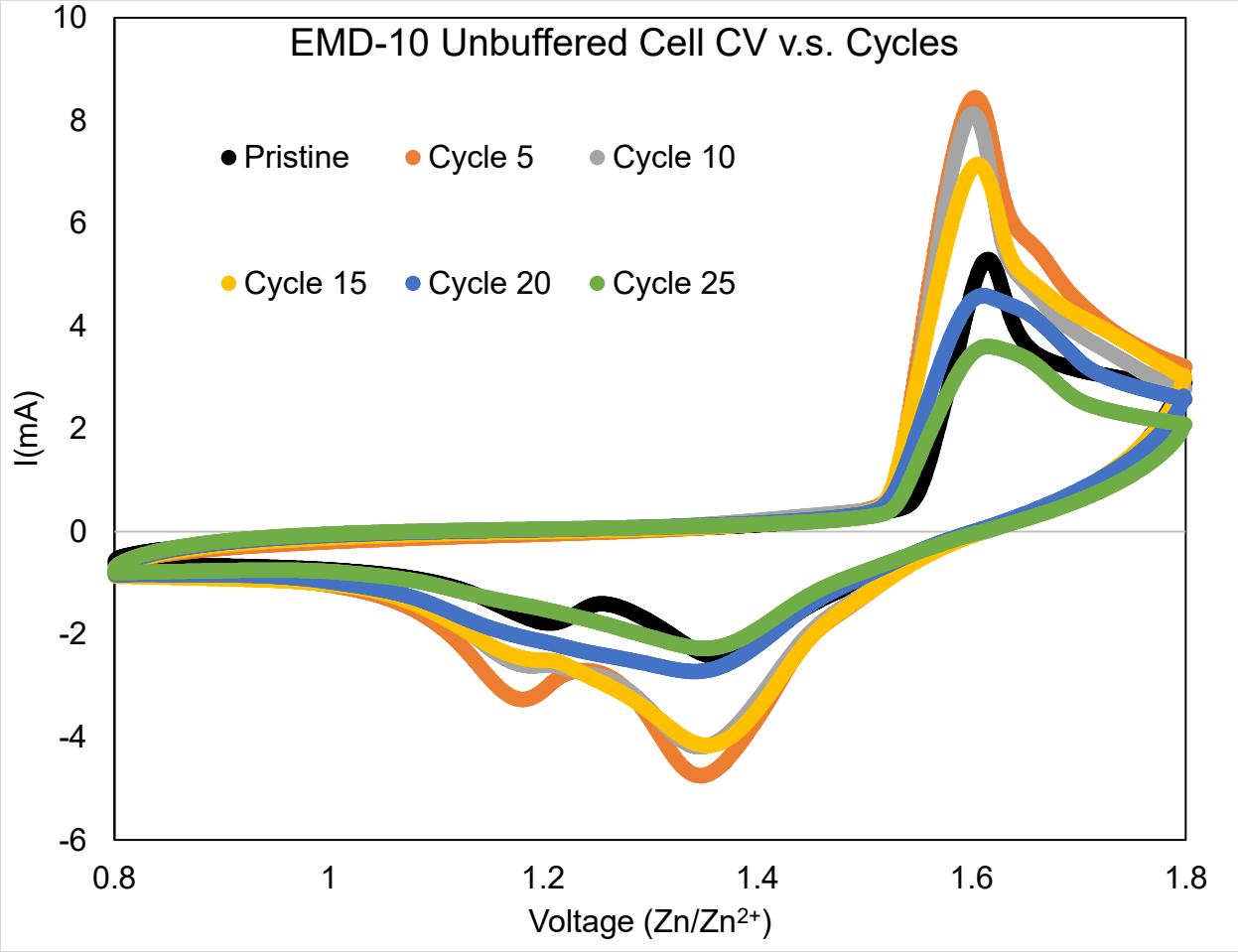

Figure 41 CV comparison of an EMD-10 cell with unbuffered electrolyte after certain cycles. Collected from pristine state to 25 cycles.

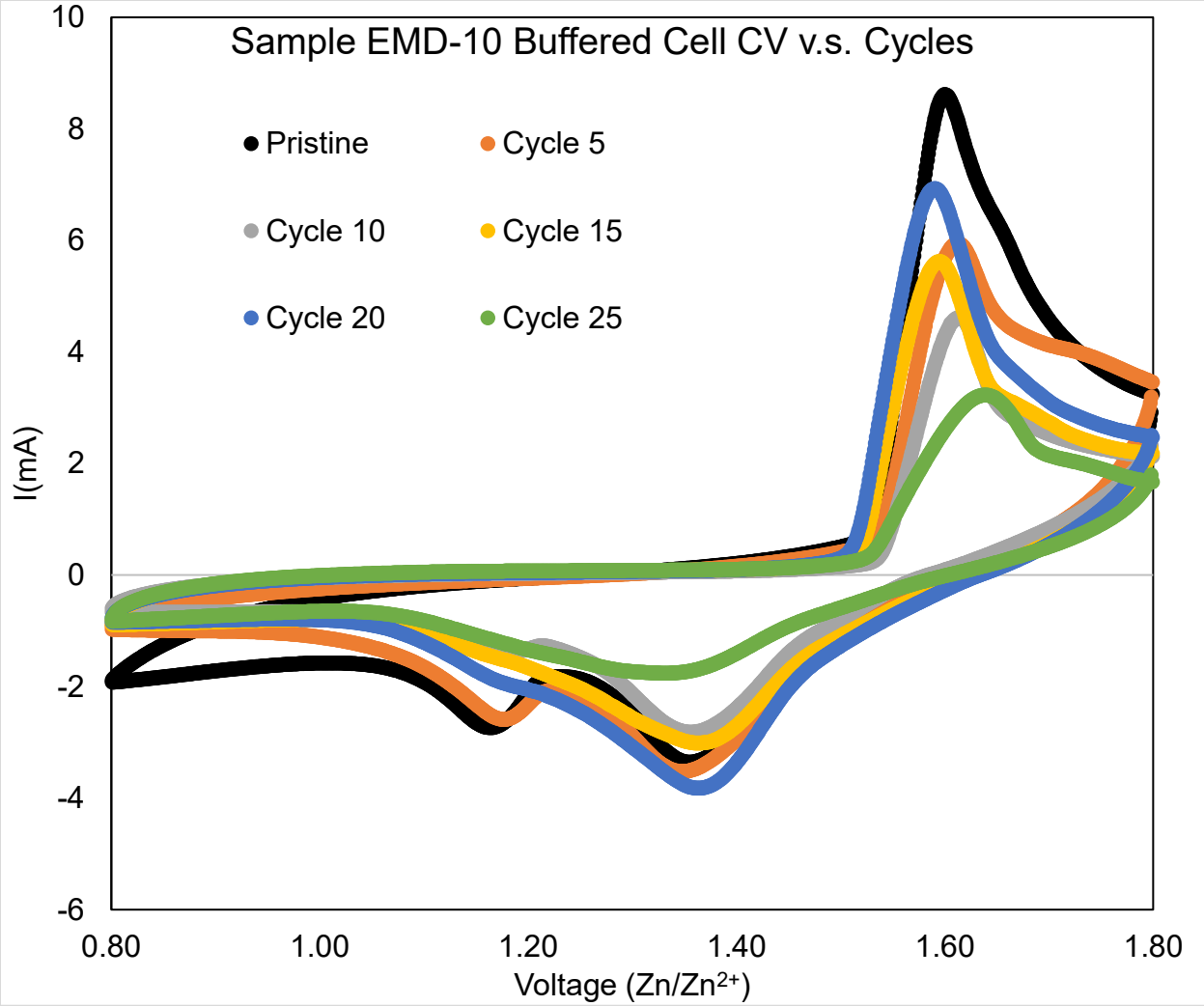

Figure 42 CV comparison of an EMD-10 cell with buffered electrolyte after certain cycles. Collected from pristine state to 25 cycles.

Comparing buffered and unbuffered EMD-10 cells, they are following a similar trend to their counterparts of EMD-1, that Mn loss became inevitable over cycling. However, we can see that the peak current is higher in the buffered group than unbuffered groups, while attenuation is slowed down. In order to fully interpret the CV results, deeper analysis is required.

4.3.3. Analyzing CV Information to Understand Internal Chemistry

From Chapter 3 we established that capacitance can be derived from cyclic voltammetry (CV) profiles. In addition to capacitance, CV analysis provides further electrochemical information that are indicators of underlying mechanisms and/or internal cell chemistry. Specifically, quantitative evaluation of reversible charge, coulombic efficiency, and areal capacity derived from integrated current responses enables a more complete assessment of electrode performance and its evolution during cycling. These parameters not only reflect the electrochemical reversibility of the system but also allow for comparisons of stability and retention across buffered and unbuffered electrolyte conditions.

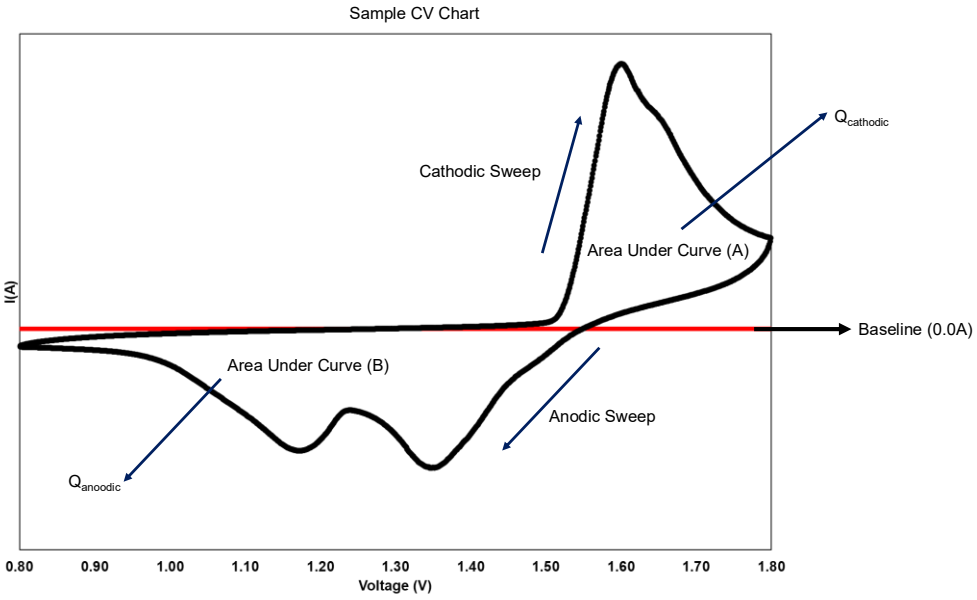

Figure 43 Sample CV plot interpretation for determining charge and capacitance in CV. The CV curve is integrated against baseline (current 0.0 A). Area under the curve and above baseline (A) is defined as cathodic charge. The counterpart below is defined as anodic charge.

Reversible and irreversible charges can be determined from CV data accounting for current response to potential.

The methods used to analyze CV in terms of charge and capacitance are adapted from both classical electrochemical analysis[4] and literature reports on pseudocapacitive and intercalation-type materials[7] [12] [13] [14] . Specifically, capacitance is determined from the integrated current response normalized by scan rate, a widely established approach in pseudocapacitor research. The concept of reversible charge, defined as the overlap between anodic and cathodic charges within a CV cycle, has been adopted in several recent studies as a qualitative descriptor of redox reversibility in electrode materials. While this parameter is not a formal substitute for coulombic efficiency in galvanostatic cycling, it provides useful comparative insights into interfacial stability and charge-storage reversibility.

The integration of anodic and cathodic current sweep over potential provides the values of charges. Taking those values into account, equation can be applied to unravel the reversible process. Given the defined values of anodic (Q_{ano}) and cathodic charges (Q_{cath}), the reversible charge is defined as:

$$Q_{rev} = (\min(|Q_{ano}|, |Q_{cath}|)$$

Equation 11 Definition of reversible charge obtained from CV.

Capacitance determination is conventionally applied to pseudocapacitive materials, while capacity from galvanostatic cycling remains the standard for batteries. Since MnO_2 exhibits mixed intercalation and pseudocapacitive behavior, capacitance was estimated from CV following established methods mentioned. Here, these values are treated as comparative indicators of interfacial charge storage rather than direct substitutes for galvanostatic capacity.

Based on the reversible capacitance, areal capacitance is determined by using the cell area. Reversible capacitance is defined as follows, given ΔV is 1V (0.8-1.8V range).

$$C_{rev} = \frac{Q_{rev}}{\Delta V}$$

Equation 12 Reversible capacitance calculation from reversible charge.

Areal capacitance is defined based on reversible capacitance, given using equation below:

$$C_{areal} = \frac{C_{rev}}{area}$$

Equation 13 Areal capacitance determination from reversible capacitance.

Clarification of capacitance used in this section is required for a deep understanding of the results. Two capacitance terms are used, equivalent capacitance and reversible capacitance. Equivalent capacitance ($C_{equivalent}$) considers the total integrated current from both anodic and cathodic sweeps, while the reversible capacitance (C_{rev}) is determined from the smaller of the anodic and cathodic charges and thus accounts only for the charge that can be recovered in subsequent cycles. While $C_{equivalent}$ gave an insight into total charge storage (capacitive + faradaic), it often overestimates the true capacitive contribution due to inclusion of irreversible processes such as side reactions. On the contrary, C_{rev} only considers reversible contributions, which can be accessed by the following cycles. In our work, calculated capacitance values may appear significantly higher than expected.

This is likely arising from pseudocapacitive behavior that MnO_2 exhibits.[7] **Error! Reference source not found.** In our aqueous system, fast and reversible proton/Zn^{2+} intercalation occurs across a wide potential window.

Following these terms, analysis of the CV data in full is presented here. First, we analyzed reversible charges in CV of EMD-1 cells, in fraction form (by normalizing pristine state to 1) and in actual amount form (using Columb as unit). The results are as follows.

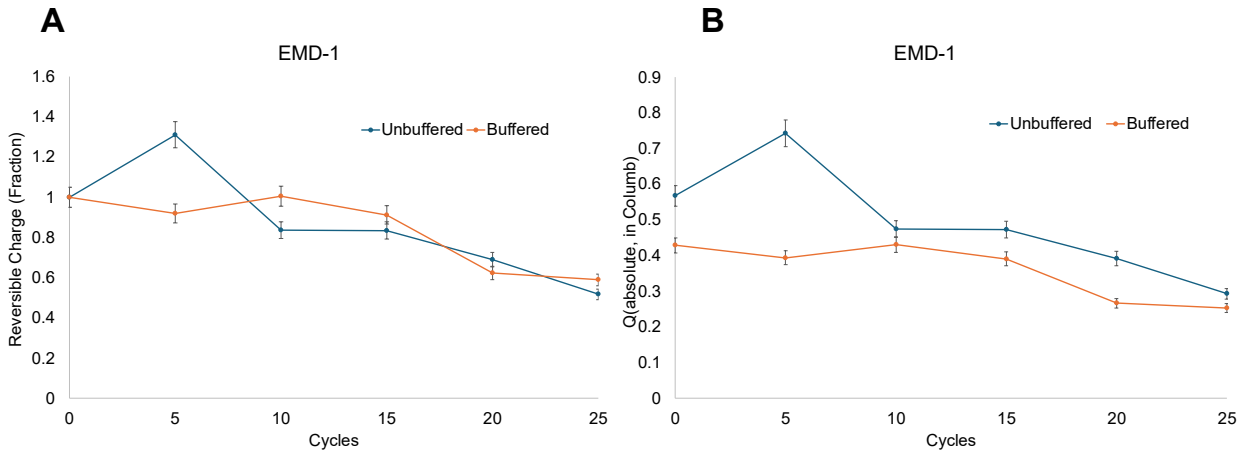

Figure 44 Reversible charge (Q_{rev}) of EMD-1 (panel A) is expressed in fractions by normalizing pristine stage charge to 1. Panel B illustrates the same results using absolute number of charges reversible, in Coulombs.

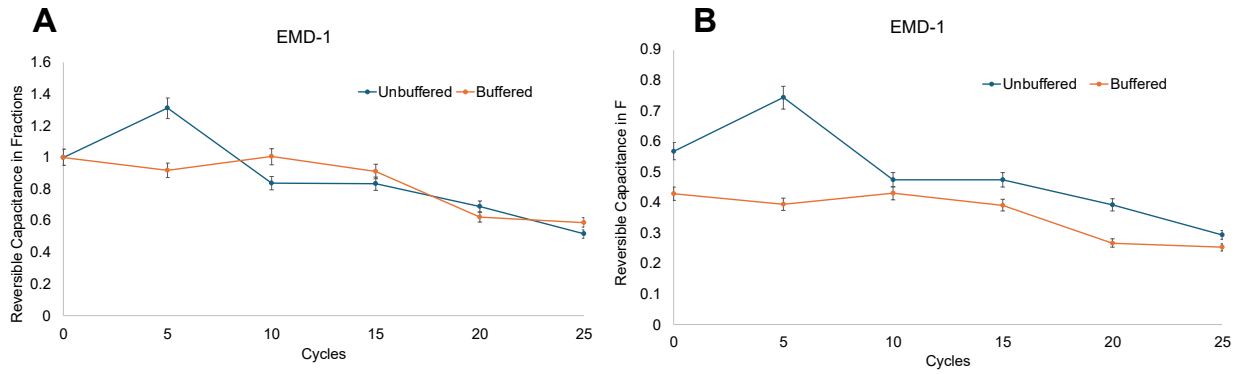

Figure 45 (Panel A): Reversible capacitance (C_{rev}) of EMD1 cells as a function of cycle number in buffered and unbuffered electrolytes, expressed in fractions by normalizing pristine stage charge to 1. (Panel B): Reversible capacitance (C_{rev}) of EMD1 cells as a function of cycle number in buffered and unbuffered electrolytes, expressed in actual values (F).

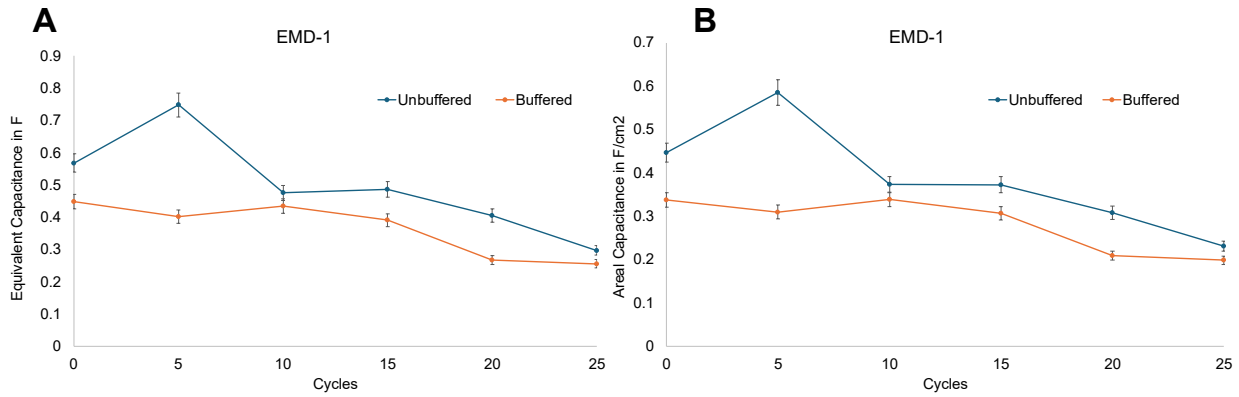

Figure 46 (Panel A): Equivalent capacitance (C_{rev}) of EMD1 cells as a function of cycle number in buffered and unbuffered electrolytes, expressed in actual values (F). (Panel B): Areal capacitance (C_{areal}) of EMD1 cells as a function of cycle number in buffered and unbuffered electrolytes.

For EMD-1 electrodes, unbuffered cells initially outperform buffered ones in reversible charge and capacitance, reaching as high as a factor of 1.3 to normalized reversible charge and ~0.73 F by cycle 5. However, these values collapse rapidly after 10–15 cycles, with capacitance falling below 0.30 F and charge retention dropping under 50% by cycle 25. Buffered cells, by contrast, maintain reversible

charge near 1.0 in early stages, retain ~65% of initial capacity by cycle 25, and show consistently higher coulombic efficiency after activation. Areal capacitance also decays more smoothly in buffered cells, reflecting reduced interfacial instability.

Thus, although unbuffered cells exhibit stronger early-cycle currents, buffered electrolytes ensure superior long-term electrochemical stability and reversibility, correlating with higher galvanostatic capacity retention observed in Chap. 3.

Similar to EMD-1, analysis returns a similar outcome for EMD-10 materials.

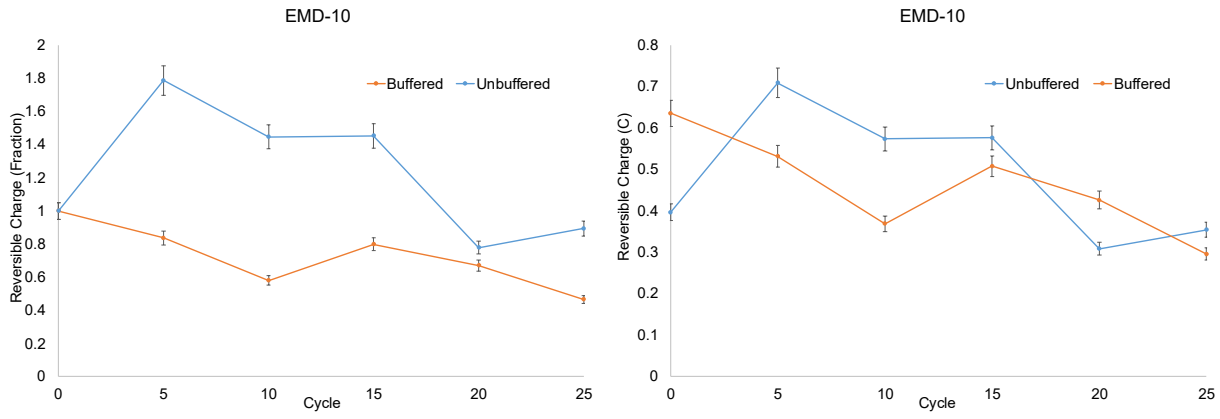

Figure 47 Reversible charge (Q_{rev}) of EMD-10 (panel A) is expressed in fractions by normalizing pristine stage charge to 1. Panel B illustrates the same results using absolute number of charges reversible, in Coulombs.

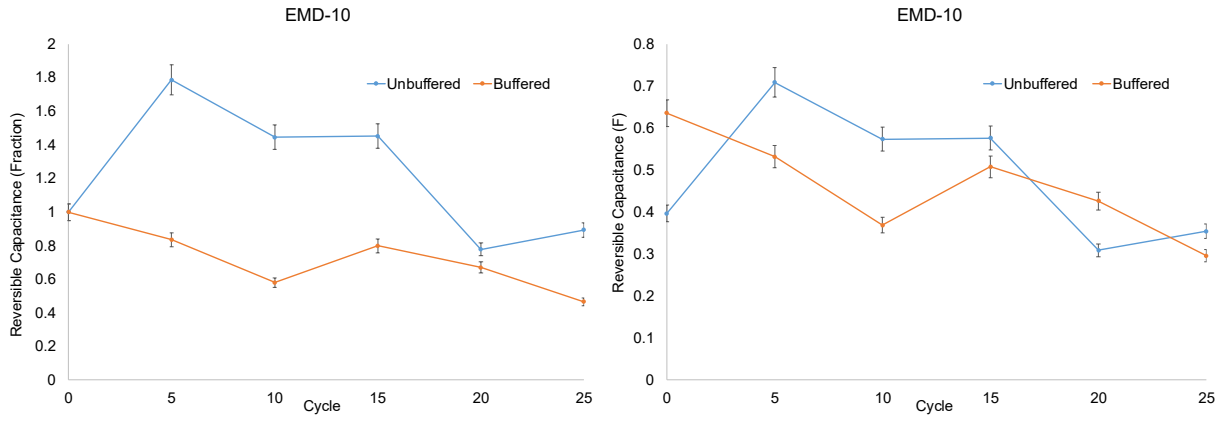

Figure 48 (Panel A): Reversible capacitance (C_{rev}) of EMD-10 cells as a function of cycle number in buffered and unbuffered electrolytes, expressed in fractions by normalizing pristine stage charge to 1. (Panel B): Reversible capacitance (C_{rev}) of EMD1 cells as a function of cycle number in buffered and unbuffered electrolytes, expressed in actual values (F).

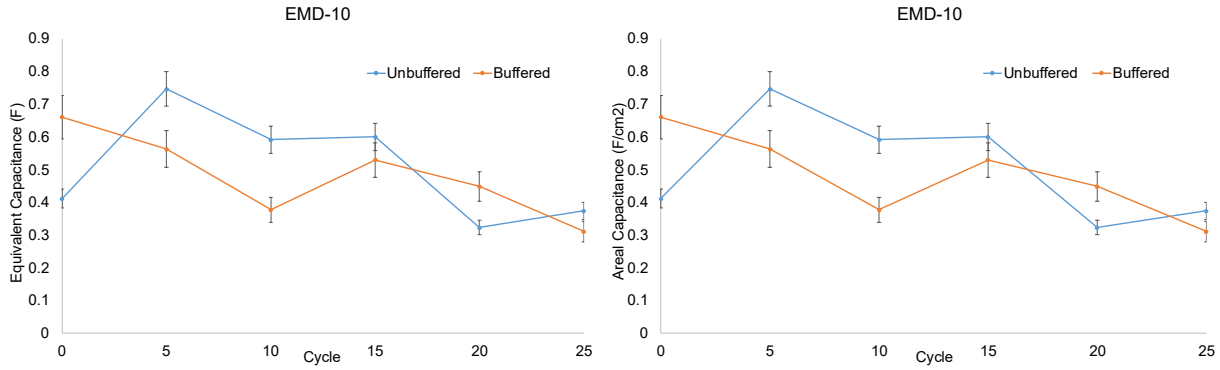

Figure 49 (Panel A): Equivalent capacitance (C_{rev}) of EMD-10 cells as a function of cycle number in buffered and unbuffered electrolytes, expressed in actual values (F). (Panel B): Areal capacitance (C_{areal}) of EMD1 cells as a function of cycle number in buffered and unbuffered electrolytes.

For EMD-10 cells, similar trend is observed to EMD-1 cells. The unbuffered cells demonstrated an early-cycle advantage, with reversible charge nearly doubling by cycle 5 and capacitance peaking at ~0.72 F, significantly higher than buffered. However, this decayed quickly after cycle 10. The unbuffered group started to decline, with both reversible charge and capacitance falling sharply and converging

to buffered values by cycles 20–25. Buffered cells, although initially lower in both absolute and normalized reversible charge (~0.45 F and ~1.0 normalized at cycle 0–5), displayed a more gradual decay, preserving ~55–60% of initial capacitance and maintaining higher stability in later cycles. Areal capacitance followed the same trend, with buffered cells exhibiting smoother decay profiles compared to the more erratic unbuffered response. Coulombic efficiency remained above 90% for both groups, but buffered cells showed less fluctuation and improved stability across the full cycle range. These observations indicate that while unbuffered cells undergo strong early activation, they suffer from accelerated interfacial degradation, whereas buffered electrolytes sustain more reversible charge and capacitance over extended cycling, aligning with their superior long-term capacity retention demonstrated in Chap. 3.

Correlating capacity decay and retention in Chap. 3, apparent discrepancies sometimes arise when CV-derived metrics suggest higher capacitance in unbuffered cells compared to buffered ones. While it is true that the total integrated charge from CV can be directly related to capacity under sufficiently slow scan rates and carefully chosen current densities, in practice CV is often performed at faster potential sweep rates where the response is dominated by pseudocapacitive processes and near-surface intercalation. Under such dynamic conditions, CV provides a sensitive measure of redox reversibility and coulombic efficiency trends, but it does not fully capture the long-timescale utilization of bulk active material that governs galvanostatic cycling performance. Thus, CV is most appropriately used here to highlight the stabilizing effect of buffer additives on redox processes

and interfacial reversibility, while quantitative assessment of capacity retention relies on galvanostatic cycling data. [4] [5] [7]

These CV calculations and analysis are mostly used for reference of cell charge-discharge activities and used to infer charge storage mechanisms. As mentioned in Chapter 1 and Chapter 2, MnO_2 electrodes store charge through a combination of diffusion-limited Zn^{2+} intercalation and surface-controlled pseudocapacitive processes. Buffer additives do not introduce new storage mechanisms, but they stabilize the electrode–electrolyte interface and prevent side reactions. This stabilizing role is reflected in the improved overlap of anodic and cathodic currents and the reduced polarization observed in buffered systems.

4.3.4. Analysis of EIS Spectra

Electrochemical impedance spectroscopy (EIS) experiments were conducted on assembled cells at different cycling stages to monitor changes in internal resistance and interfacial properties over time. The measurement conditions, including frequency range, AC amplitude, and stabilization time, are summarized in Table 6. These parameters were optimized through preliminary trials to ensure reproducibility and minimize noise.

Table 6 EIS experimental collection parameters

Parameter	Values
AC Voltage	10.0 mV
Frequency Range	10^{-2}-10^{4} Hz
Points/Decade	25
Optimize Mode	Low noise
Estimated Z	100 Ω
Drift Correction	ON

Using the established protocol, EIS spectra were collected at fixed intervals following cell assembly at respective resting potential, including the pristine state and subsequent cycles. This approach allowed for the evaluation of time-dependent impedance evolution, potentially associated with interfacial degradation, electrolyte decomposition, or accumulation of surface films.

For analytical purposes, the Nyquist plot of scanned EIS spectra is superimposed to view gradual changes for both EMD-1 and EMD-10 materials in buffered and unbuffered electrolyte.

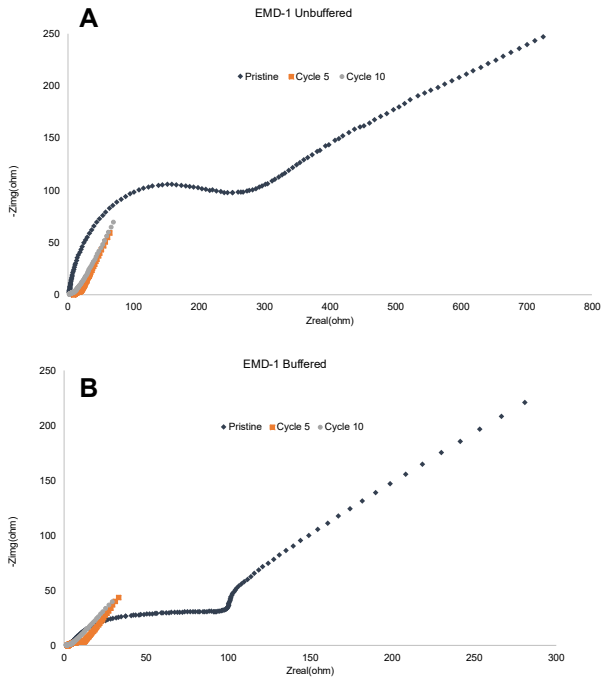

Figure 50 Nyquist plots of EMD-1 in (A) unbuffered electrolyte and (B) buffered electrolyte as a function of cycle.

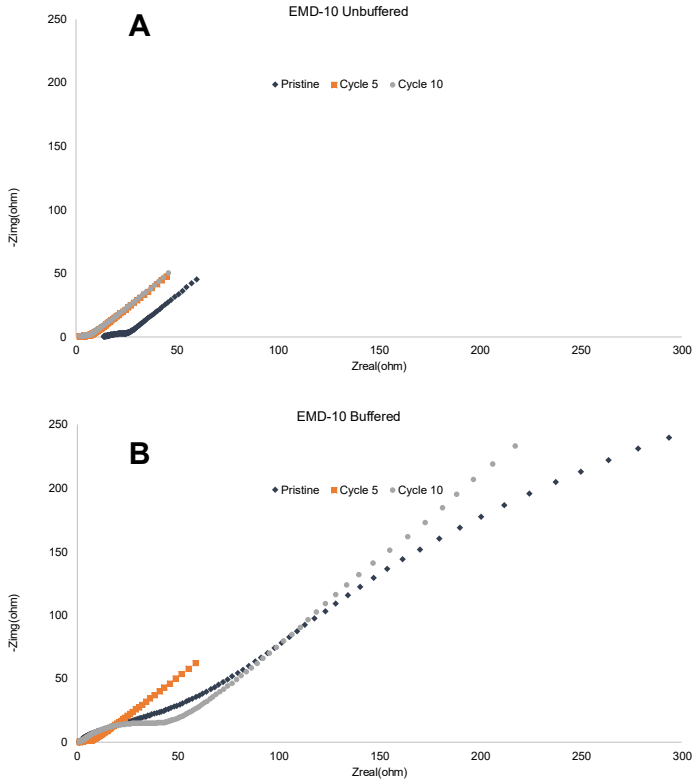

Figure 51 Nyquist plots of EMD-10 in (A) unbuffered electrolyte and (B) buffered electrolyte as a function of cycle.

As seen in Figure 50 and Figure 51, clear differences are seen in the way impedance evolves with cycling.

In unbuffered cells, both EMD-1 and EMD-10 exhibit resolvable semicircles in the pristine state that remain visible through early cycles. With cycling, the arcs enlarge or fluctuate, and the low-frequency diffusion tail becomes more dominant, consistent with increasing overall impedance. In buffered cells, the initial spectra contain smaller arcs, which diminish within the first few cycles and give way to long, slanted low-frequency responses. These observations suggested different impedance evolution trends between buffered and unbuffered groups. The tail changes showed that buffered cells shifted faster to transport-dominated responses.

The constancy of the high-frequency intercept across all cases suggests that electrolyte resistance remains stable. While these results are consistent with buffering influencing interfacial and transport processes, the present dataset does not permit a detailed mechanistic assignment. Preliminary equivalent circuit modelling (attached in appendix) has been attempted with some limitations; a deeper mechanistic overview requires more extensive modeling and complementary characterization.

4.4. X-Ray Diffraction Analysis

X-ray diffraction (XRD) analysis was conducted to investigate structural and phase changes in the MnO_2 cathodes before and after electrochemical cycling. The goal was to identify any crystalline transformations, formation of secondary phases, or structural changes associated with electrochemical system aging. [16] [8]

Reference diffraction patterns were first collected from pristine EMD (electrolytic manganese dioxide) powders to serve as a baseline. Both EMD1 and EMD10 were tested and overlayed for comparison. The resulting comparison is shown in Figure 52.

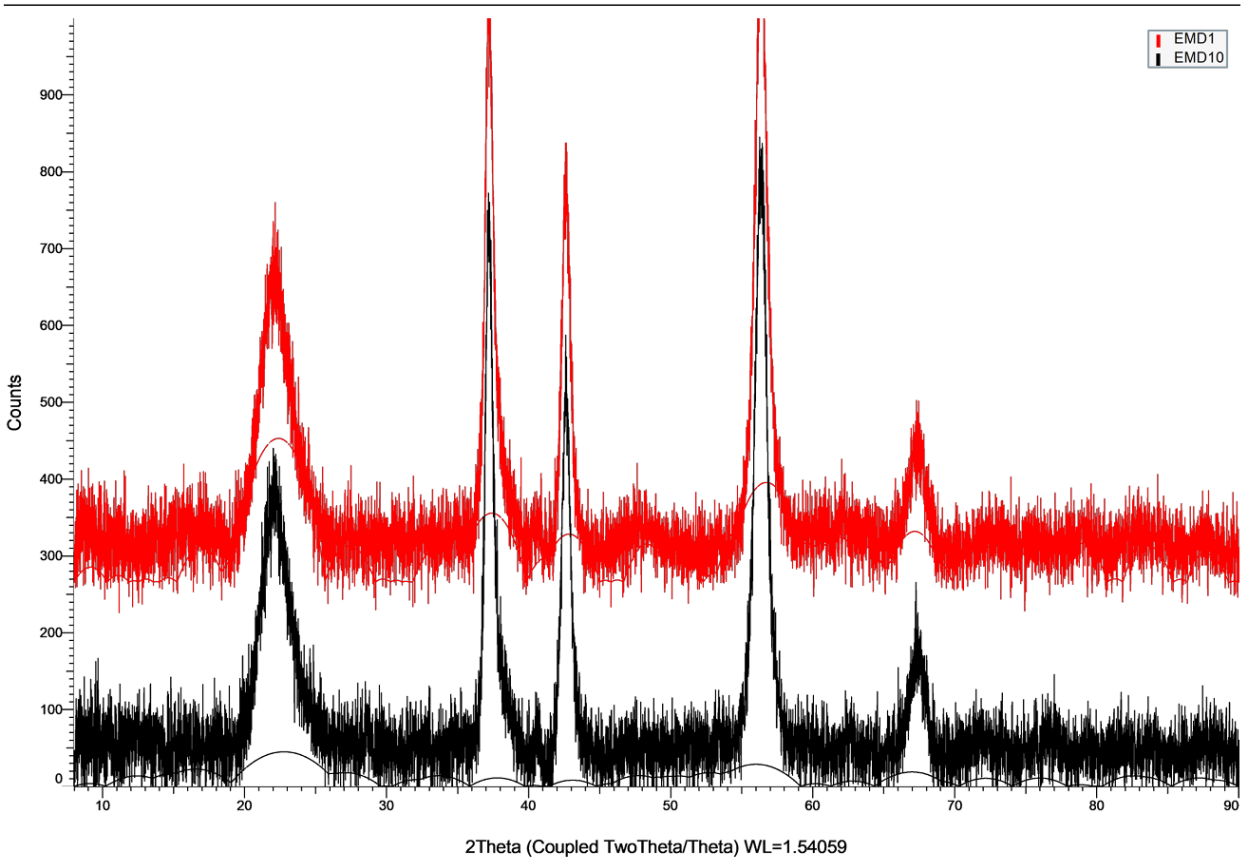

Figure 52 XRD diffraction pattern for EMD1 and EMD10 pure powder. Samples collected on Rigaku MAXfilm diffractometer with assistance from McMaster Analytical X-Ray Diffraction Facility (MAX). Radiation source used was Cu Kα radiation (λ = 1.5406 Å).

From the diffraction pattern, it can be observed that EMD1 and EMD10 powder exhibited identical diffraction angels. Both diffraction patterns exhibited similar peak intensity and location, with minimal variation observed. Component analysis of EMD1 powder (shown in Figure 53) and EMD 10 (shown in Figure 54) supported this claim.

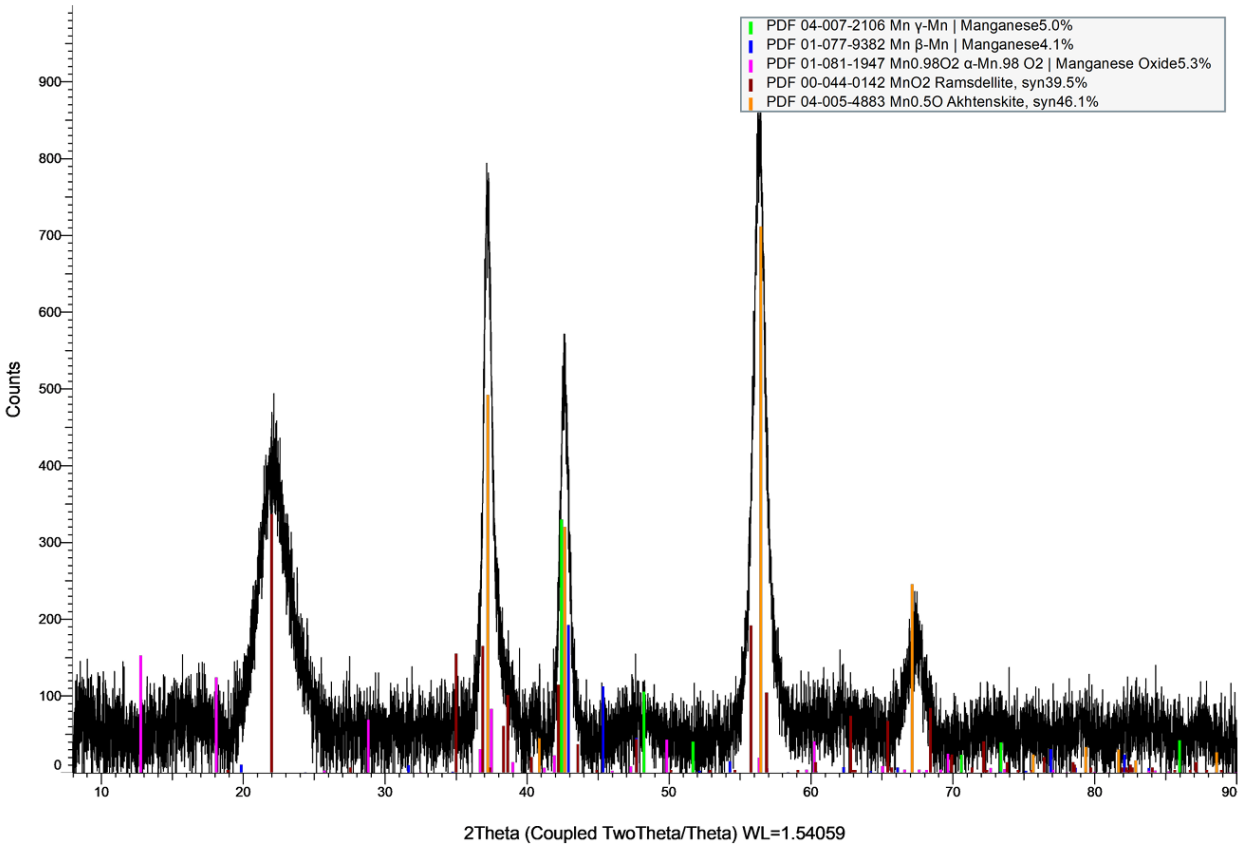

Figure 53 EMD1 pure powder diffraction pattern and component analysis. Component analysis was completed on Bruker Diffrac EVA software, with component assignment based on internal reference database.

Similarly, EMD10 powder diffraction pattern followed similar appearance.

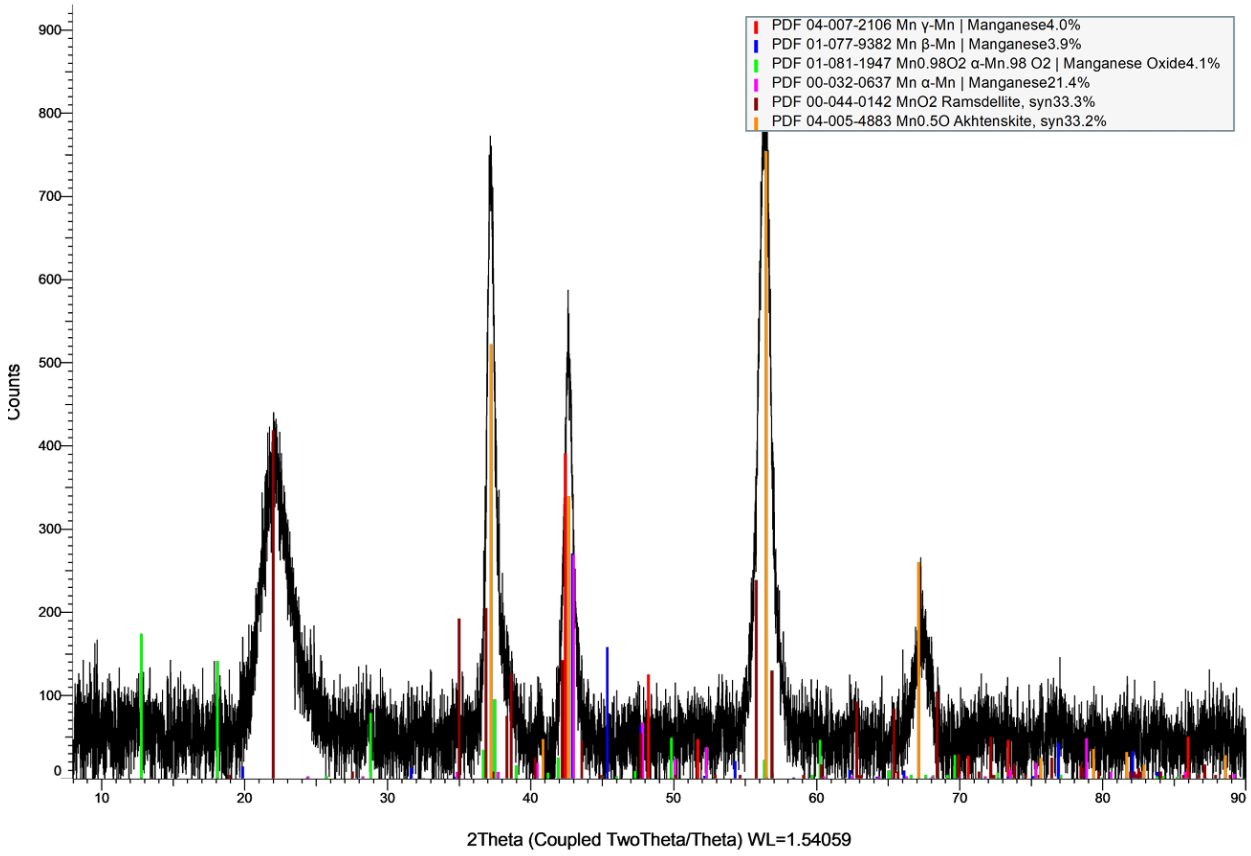

Figure 54 EMD10 powder diffraction pattern. Data collected and interpreted under same condition as EMD1.

As observed in Figure 53 and Figure 54, the XRD patterns of the pristine EMD-10 and EMD-1 powder showed prominent peaks observed at ~22°, 37°, 42°, 56°, and 66° (2θ) correspond well to multiple known manganese oxide phases.

Phase identification was performed using embedded reference databases in the analysis software, which matched the patterns to various Mn and MnO_2 polymorphs, including γ-Mn, β-Mn, α-Mn, and notably, Ramsdellite and Akhtenskite. The structure of each phase is shown as in Figure 55, each phase showed a similar tunnel and layered structure.

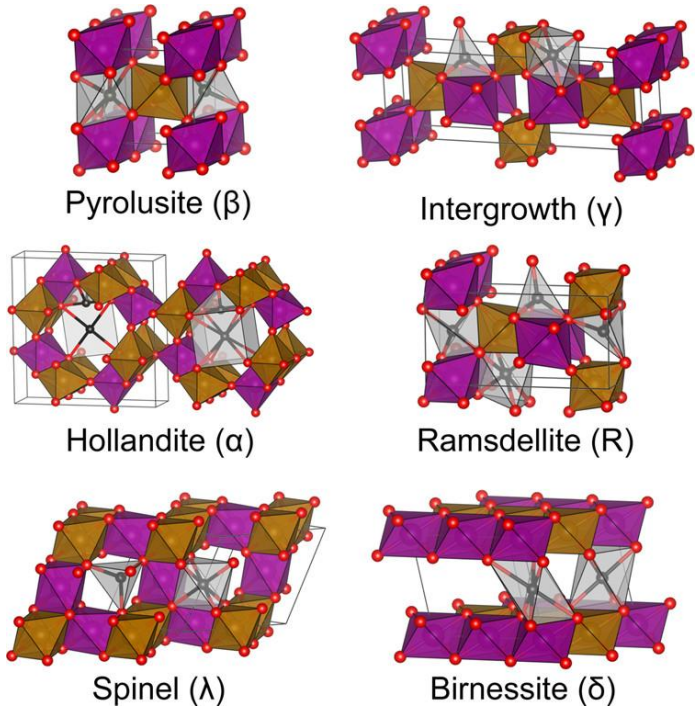

Figure 55 Various phases of manganese dioxide explained, adapted from J. Am. Chem. Soc. 2017, 139, 7, 2672–2681, reprinted with permission, Copyright © 2017 American Chemical Society

The identification of Ramsdellite—a tunnel-structured MnO_2 polymorph with a similar tunnel configuration as β-Mn indicated that pristine material may bear a high degree of tunnel ordering. Despite its similarity to with β-MnO_2, it is more accessible to Zn^{2+} insertion due to its larger tunnel size. This makes it especially favorable for reversible ion intercalation.

The presence of mixed tunnel-type phases, including γ- and ε-type MnO_2 (often viewed as intergrowths of β- and Ramsdellite domains), confirms that the pristine EMD material consists of a structurally diverse but electrochemically favorable.

Importantly, the diffraction profiles of EMD-10 and EMD-1 are nearly identical, with overlapping peak positions and comparable intensities. No significant differences were observed in terms of peak shifting, broadening, relative phase distribution, or minor phase

presence. This strongly suggests that the initial chemical phase composition is not a determining factor in any performance differences between the two materials.

To assess structural changes after prolonged operation, cathodes retrieved from cycled cells were examined under identical XRD conditions. All samples were scanned from 10° to 90° (2θ) using Cu Kα radiation (λ = 1.5406 Å). The post-cycling XRD patterns are shown in here using EMD-1 samples due to their similarity with EMD-10 materials. For EMD-1 cycled in buffered electrolytes, the attempt has been conducted and attached in appendix. The broad amorphous hump from SiO_2 (glass fiber) masked the low-angle region where MnO_2 reflections typically occur, while the intense graphite (002) peak at ~26.5° overshadowed nearby features. Additional sharp reflections from the Si holder further overlapped with Mn-oxide/spinel regions. As a result, any Mn-oxide peaks were diminished below the detection limit. The raw data are included in Appendix for completeness, but no structural conclusions are drawn from these measurements.

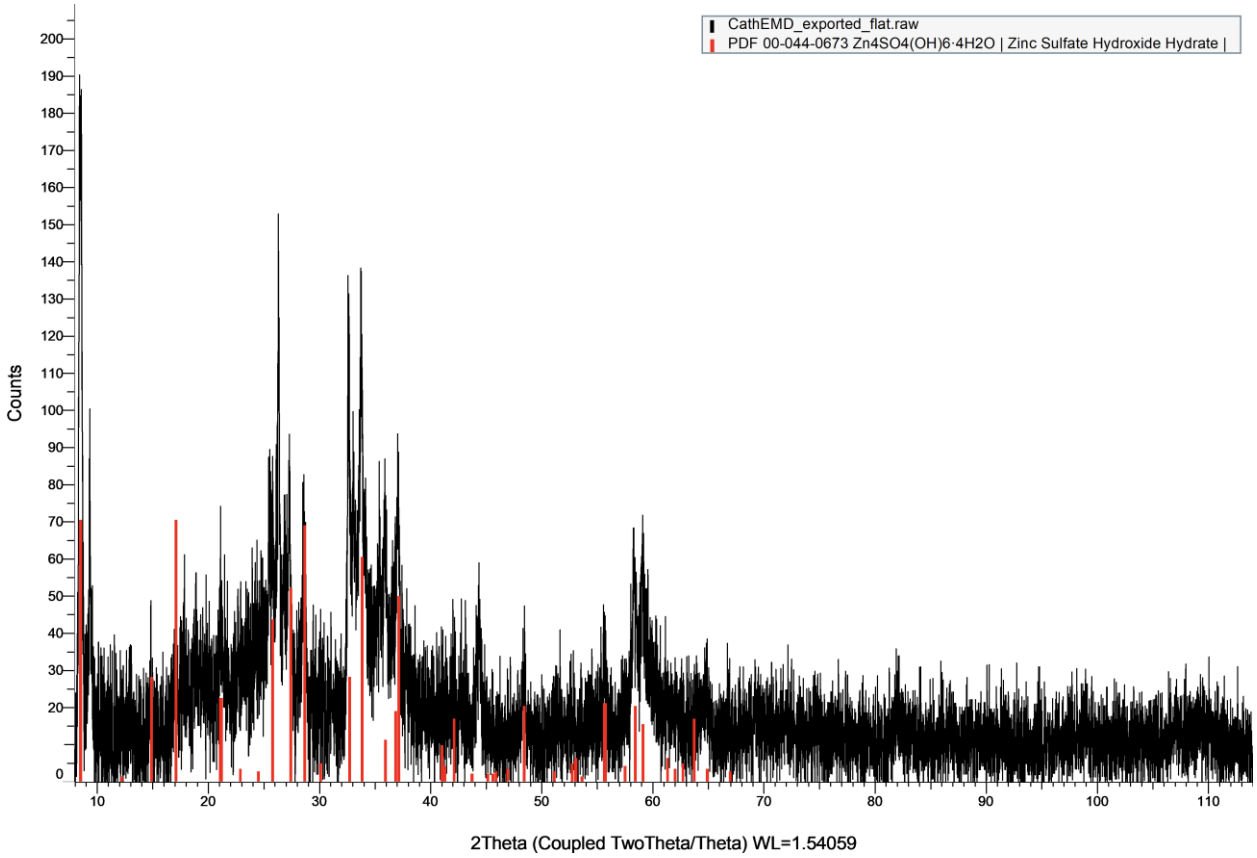

Figure 56 EMD-1 cathode collected after cycling in unbuffered electrolytes. Only zinc hydroxysulphate observed.

The cycled cathodes showed presence of silicon components and carbon, which comes from glass fiber residue and carbon paper base. The revolved diffraction pattern does not indicate any pure phase Mn or MnO_2, with completely different patterns as pure pristine materials. This result was expected due to electrochemical cycling is a dynamic process, with repetitive dissolution-redeposition of Mn-species around cathode surface. Over cycling, the redeposition of Mn-species, as a complex and dynamic process, would not generate identical species as initial pristine stage. However, observed difference in remaining residue indicated buffered and unbuffered groups may explain the difference in output performance.

4.5. Discussion of results

Based on the results interpretation, capacity enhancement by buffer addition is not strongly induced by suppressed cathode dissolution, however, it could be contributed to multiple other sources. Surface morphology characterization indicates that buffer may participate in retaining favorable structure after cycling, which is primarily achieved by preventing excessive precipitation and insoluble mass accumulation. Thus, ion transport remains at a sustainable level. Cyclic voltammetry results indicated that possible reaction mechanism changes occurred with buffer additives. EIS revealed that unbuffered EMD cells primarily degrade through increasing interfacial charge-transfer resistance, whereas buffered cells undergo an early transition to diffusion-dominated impedance, highlighting distinct degradation pathways that align with the observed cycling performance.

4.6. References

[1] Augustyn, V.; Simon, P.; Dunn, B. Pseudocapacitive Oxide Materials for High-Rate Electrochemical Energy Storage. *Energy Environ. Sci.* **2014**, *7*, 1597–1614.

[2] Barsoukov, E.; Macdonald, J. R. *Impedance Spectroscopy: Theory, Experiment, and Applications*; Wiley, 2018.

[3] Bischoff, C. F.; Fitz, O. S.; Burns, J.; Bauer, M.; Gentischer, H.; Birke, K. P.; Henning, H.-M.; Biro, D. Revealing the Local Ph Value Changes of Acidic Aqueous Zinc Ion Batteries with a Manganese Dioxide Electrode during Cycling. *Journal of The Electrochemical Society* **2020**, *167* (2), 020545.

[4] Conway, B. E. Electrochemical Supercapacitors; Springer Nature, 2013

[5] Dunn, B.; Kamath, H.; Tarascon, J. M. Electrical Energy Storage for the Grid: A Battery of Choices. *Science* **2011**, *334*, 928–935.

[6] Ernst, R. R.; Bodenhausen, G.; Wokaun, A. *Principles of Nuclear Magnetic Resonance in One and Two Dimensions*; Clarendon Press: Oxford, **1987**.

[7] Guillemet, Ph.; Brousse, Th.; Crosnier, O.; Dandeville, Y.; Athouel, L.; Scudeller, Y. Modeling Pseudo Capacitance of Manganese Dioxide. *Electrochimica Acta* **2012**, *67*, 41–49

[8] Kundu, D.; Adams, B. D.; Duffort, V.; Vajargah, S. H.; Nazar, L. F. A High-Capacity and Long-Life Aqueous Rechargeable Zinc Battery Using a Metal Oxide Intercalation Cathode. *Nature Energy* **2016**, *1* (10). DOI:10.1038/nenergy.2016.119.

[9] Lasia, A. *Electrochemical Impedance Spectroscopy and Its Applications Andrzej Lasia*; Springer, 2014.

[10] Levitt, M. H. *Spin Dynamics: Basics of Nuclear Magnetic Resonance*, 2nd ed.; Wiley: Chichester, **2008**.
[11] Orazem, M. E.; Tribollet, B. *Electrochemical Impedance Spectroscopy*; John Wiley & Sons, Inc, 2017.
[12] Pan, H.; Shao, Y.; Yan, P.; Cheng, Y.; Han, K. S.; Nie, Z.; Wang, C.; Yang, J.; Li, X.; Bhattacharya, P.; Mueller, K. T.; Liu, J. Reversible aqueous zinc/manganese oxide energy storage from conversion reactions. Nat. Energy 2016, 1, 16039.
[13] Simon, P.; Gogotsi, Y. Materials for Electrochemical Capacitors. *Nat. Mater.* **2008**, *7*, 845–854.
[14] Stoller, M. D.; Ruoff, R. S. Best Practice Methods for Determining an Electrode Material's Performance for Ultracapacitors. *Energy Environ. Sci.* **2010**, *3*, 1294–1301.
[15] Tang, B.; Shan, L.; Liang, S.; Zhou, J. Issues and opportunities facing aqueous Zn-ion batteries. Energy Environ. Sci. 2019, 12, 3288–3304.
[16] Zhang, N.; Cheng, F.; Liu, J.; Wang, L.; Long, X.; Liu, X.; Li, F.; Chen, J. Rechargeable Aqueous Zinc-Manganese Dioxide Batteries with High Energy and Power Densities. *Nature Communications* **2017**, *8* (1).

Chapter 5 Final Conclusions

5. Conclusion and Outlook

5.1. Summary of Previous Chapters

In this work, the role and functions of buffer additives and their impact on MnO_2 based cathodes in the working condition of aqueous-based zinc ion battery is explored. We discovered that buffer additives significantly function in terms of capacity and retention. The improved capacity does not compromise any other dissolution control which remains a persistent problem for Mn-based AZIB.

Chapter 1 provides an insight into the topic, illustrating the necessity of AZIB as an alternative to mass scale energy storage. While chapter 2 discusses experiments involved in the thesis and provides a theoretical explanation to that. The future of chapter

In this work, the role and functions of buffer additives (ammonium dihydrogen phosphate-acetate compound buffer) and their impact on MnO_2-based cathodes under the operating conditions of aqueous zinc–ion batteries (AZIBs) were systematically investigated. The study demonstrated that buffer additives substantially enhance both capacity and retention compared with unbuffered electrolytes in the early stages. Buffered cells retained ~60–65% of their initial capacity after 25 cycles without controlling dissolution of MnO_2 from cathode, whereas unbuffered cells decayed below 50% over the same period. Cyclic voltammetry further confirmed that buffered electrolytes maintain higher coulombic efficiency, smoother decay in reversible charge, and more stable Mn redox activity, even though unbuffered cells displayed transiently higher early-cycle capacitance.

Experiments leading towards mechanistic understanding revealed that the improved performance does not arise from suppression of Mn dissolution, which remained a persistent challenge for Mn-based AZIBs, as shown by NMR relaxometry. Instead, scanning electron microscopy and X-ray diffraction analyses indicated some other underlying effect that buffered electrolytes have. Electrochemical impedance spectroscopy and cyclic voltammetry suggested that buffer additives may have underlying effects in ion transport, electrolyte behavior and more.

Chapter 1 introduced the broader context of sustainable energy storage, highlighting the importance of AZIBs as an alternative to lithium-ion batteries for large-scale applications. Chapter 2 provided the theoretical background and detailed methodologies used throughout this work. Chapters 3 and 4 presented the experimental findings and mechanistic insights, respectively, establishing a coherent framework for understanding how buffer additives influence electrochemical behavior. This concluding chapter concludes these findings and proposes any future work necessary to understand the system.

5.2. Future Works

Although this study explored the performance of buffered electrolyte in AZIB systems and established buffering as an effective approach to combat some issues in AZIB. The precise mechanism remains incompletely unraveled by our experiments so far. The present work indicates that performance enhancement does not arise from suppressed cathode dissolution, but rather from other reasons.

Experimental results suggested morphological changes, deposition patterns or internal resistance changes may account for the phenomena changes.

To fully elucidate the role of buffer additives, future efforts should prioritize operando and in-situ characterization techniques capable of capturing dynamic structural and chemical changes during cycling. Approaches such as real-time X-ray diffraction, time-dependent SEM, or advanced NMR relaxometry would provide some more direct evidence.

Another important direction lies in probing electrochemical kinetics in greater depth. The present impedance results suggest that buffering has effect on resistance growth, yet the contributions of charge-transfer processes, diffusion pathways, and interfacial film formation remain only partly resolved. A more tailored experimental approach needs to be established. The equivalent circuit modelling also requires detailed work, so that the spectrum can be more supportive towards understanding.

Exploration of buffer chemistries beyond phosphate–acetate systems is also practical. While the studied formulation effectively stabilizes performance, alternative buffering agents may offer additional advantages in conductivity, solubility, or compatibility with other cathode chemistries. Systematic screening of new additives could therefore broaden the applicability of buffering strategies across different classes of aqueous batteries.

Finally, translating the observed benefits to long-term and practical conditions remains essential. Extended cycling over thousands of cycles, along with scale-up from coin cells to pouch cells, will determine whether buffering can deliver durable improvements under realistic energy-storage scenarios. Complementary computational studies may further assist in rational electrolyte design, providing atomic-level insights into electrolyte–electrode interactions.

In summary, this work provides an initial framework showing that buffer additives enhance capacity retention by preserving electrode morphology and interfacial stability, but it also opens the door to a wide range of deeper mechanistic and application-oriented investigations. Continued efforts in these directions will be crucial for advancing buffered aqueous zinc–ion batteries toward practical, sustainable energy storage solutions.

Appendix

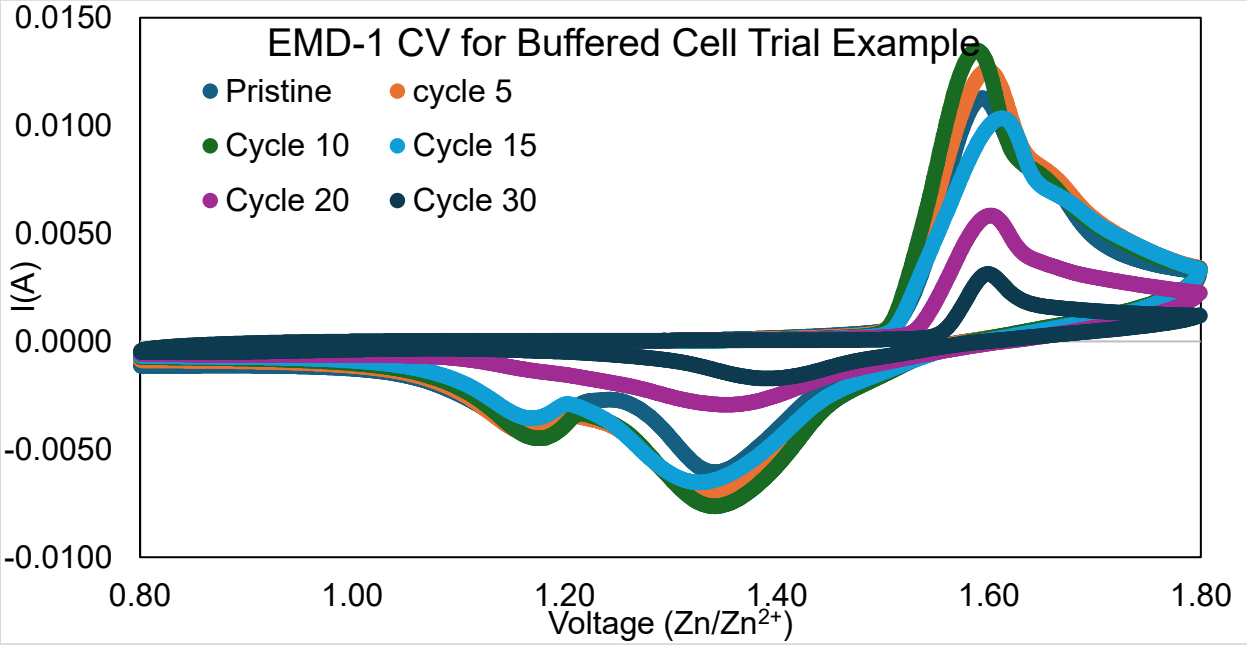

A-1 CV comparison of a similar EMD-1 cell with buffered electrolyte after certain cycles. Collected from pristine state to 25 cycles. Raw data attached for illustration.

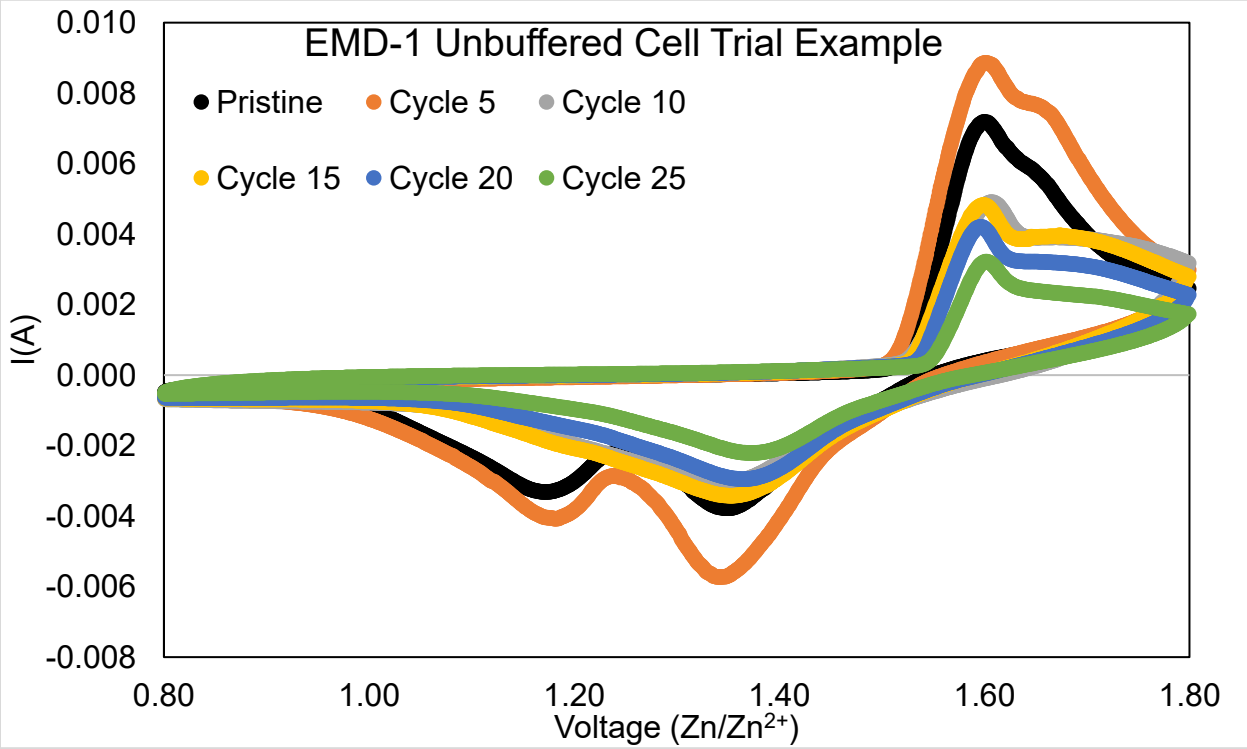

A-2 CV comparison of a EMD-1 cell with unbuffered electrolyte after certain cycles. Collected from pristine state to 25 cycles. Raw data shown here for illustration.

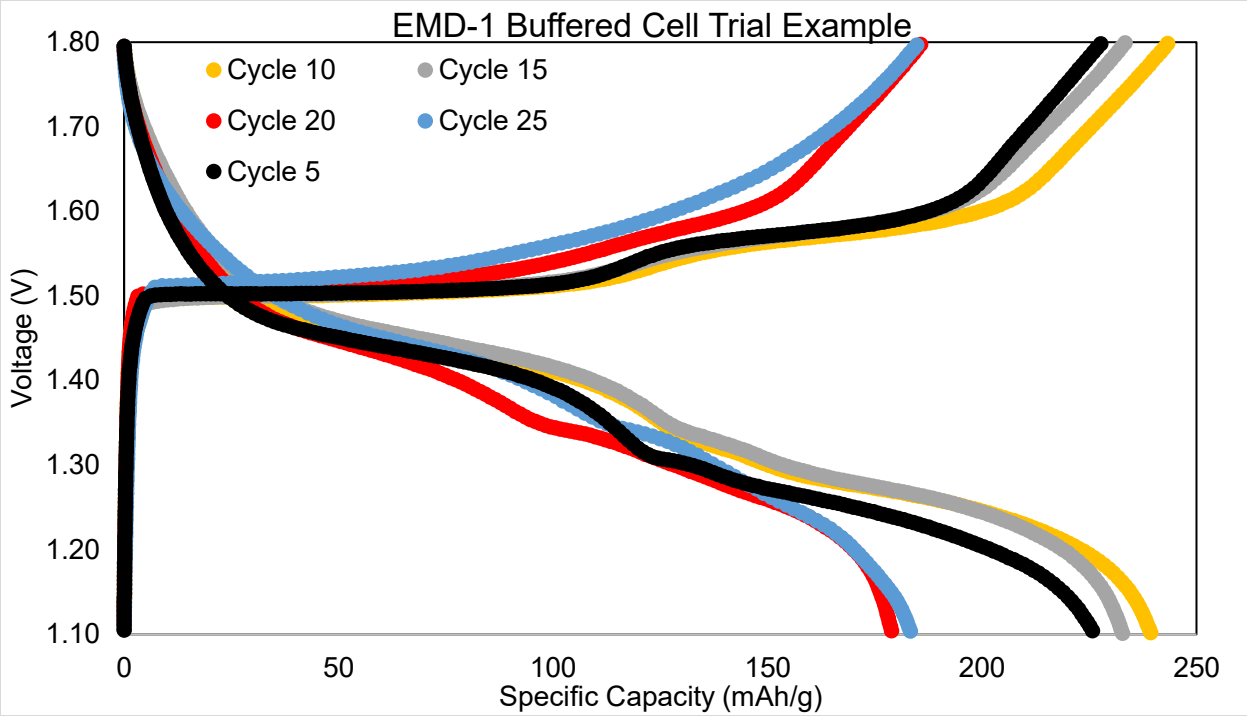

A-3 GCD plot of EMD-1 cell in buffered electrolyte.

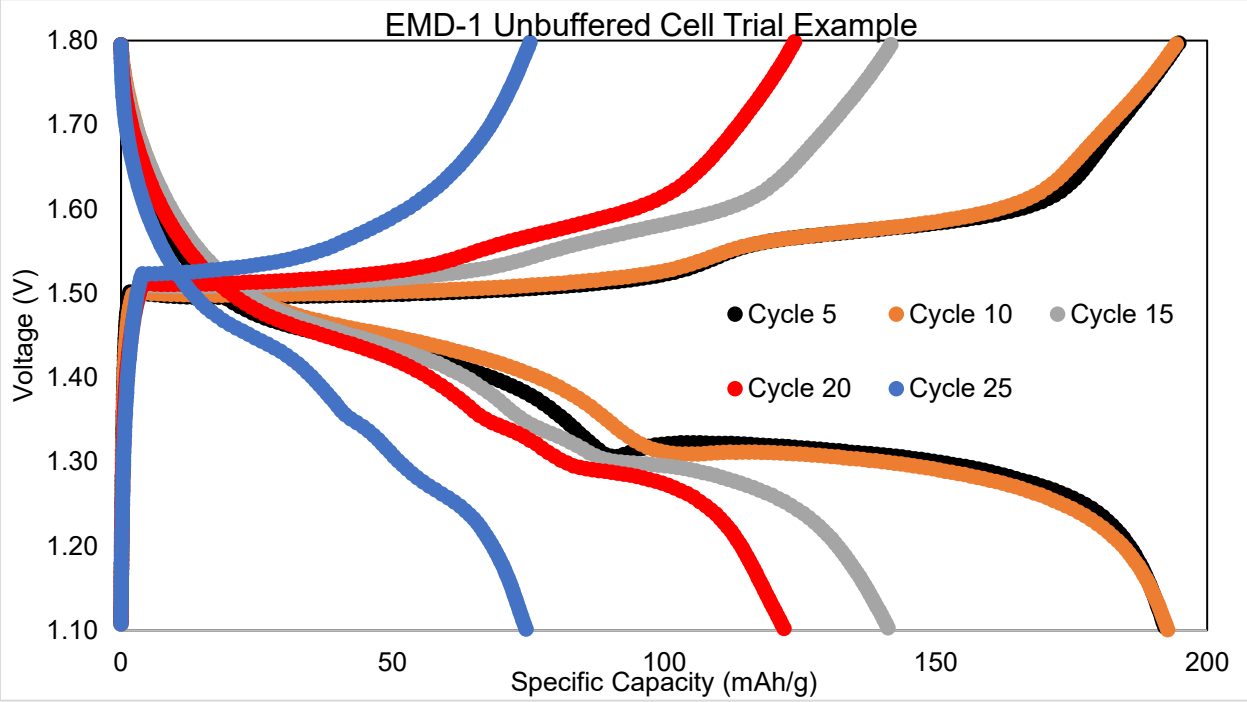

A-4 Capacity-voltage plot of EMD-1 cell in unbuffered electrolyte.

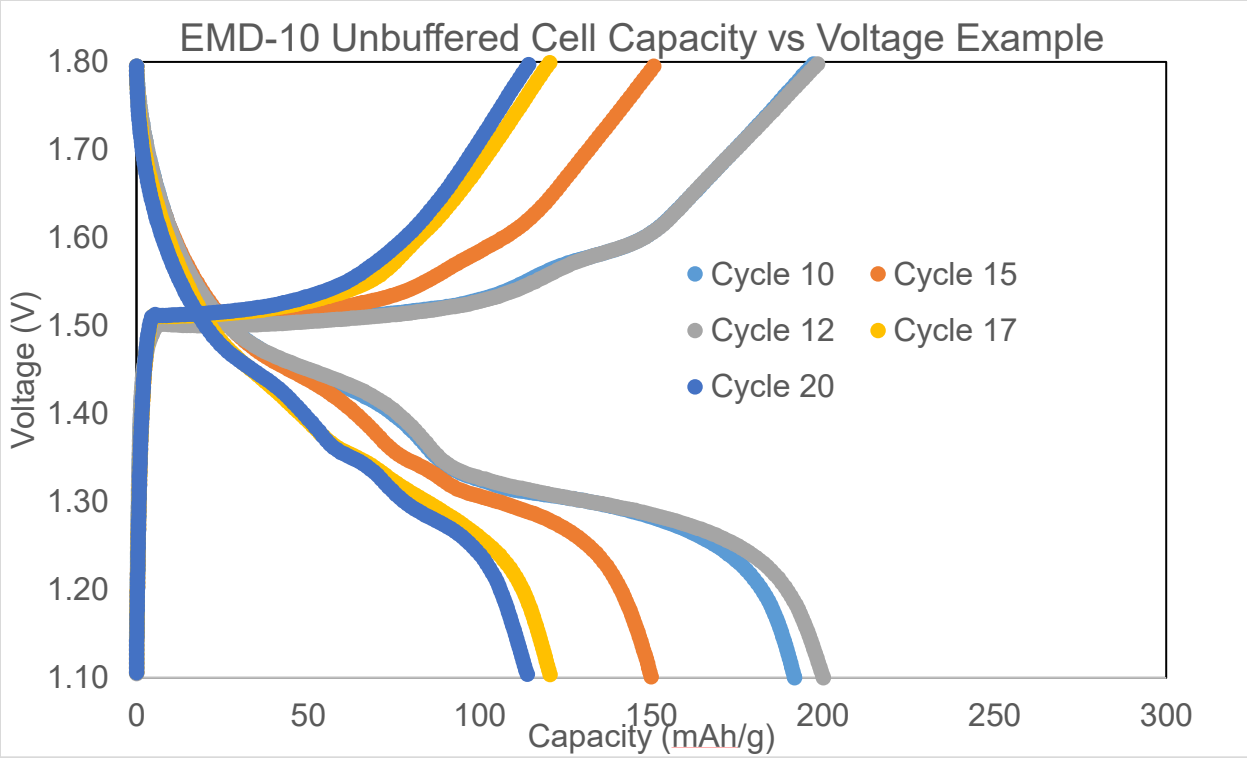

A-5 GCD plot of EMD-10 cell in unbuffered electrolyte. This plot showed different cycle number with similar trends.

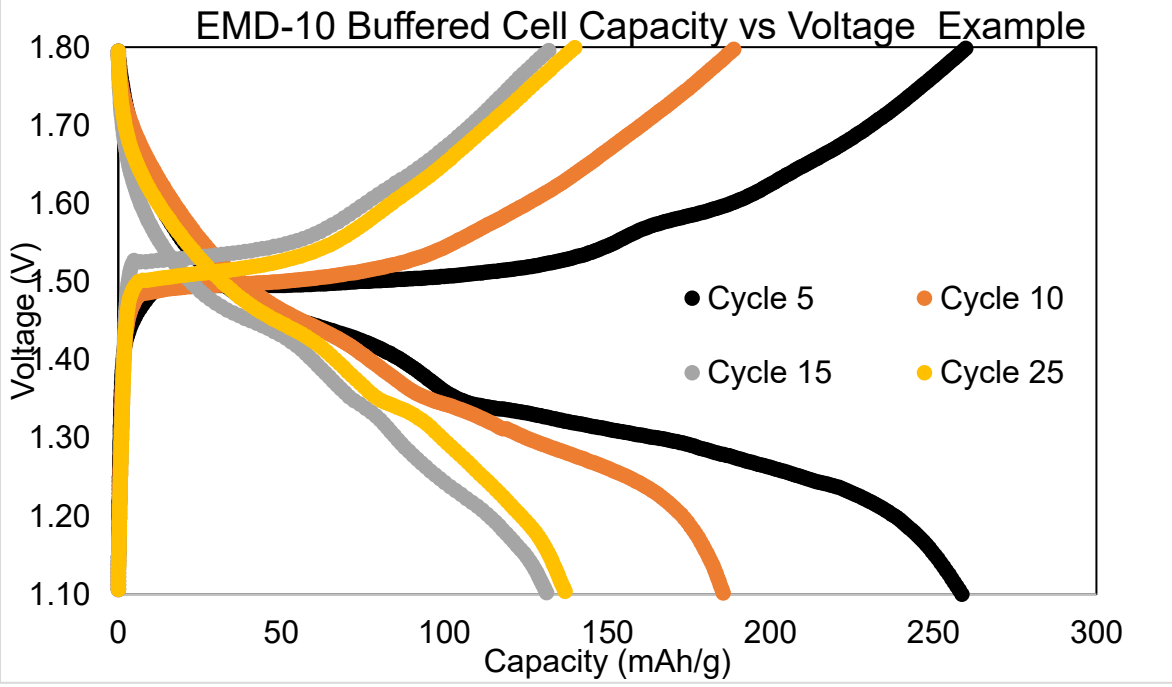

A-6 GCD plot of one testing EMD-10 cells in buffered electrolytes.

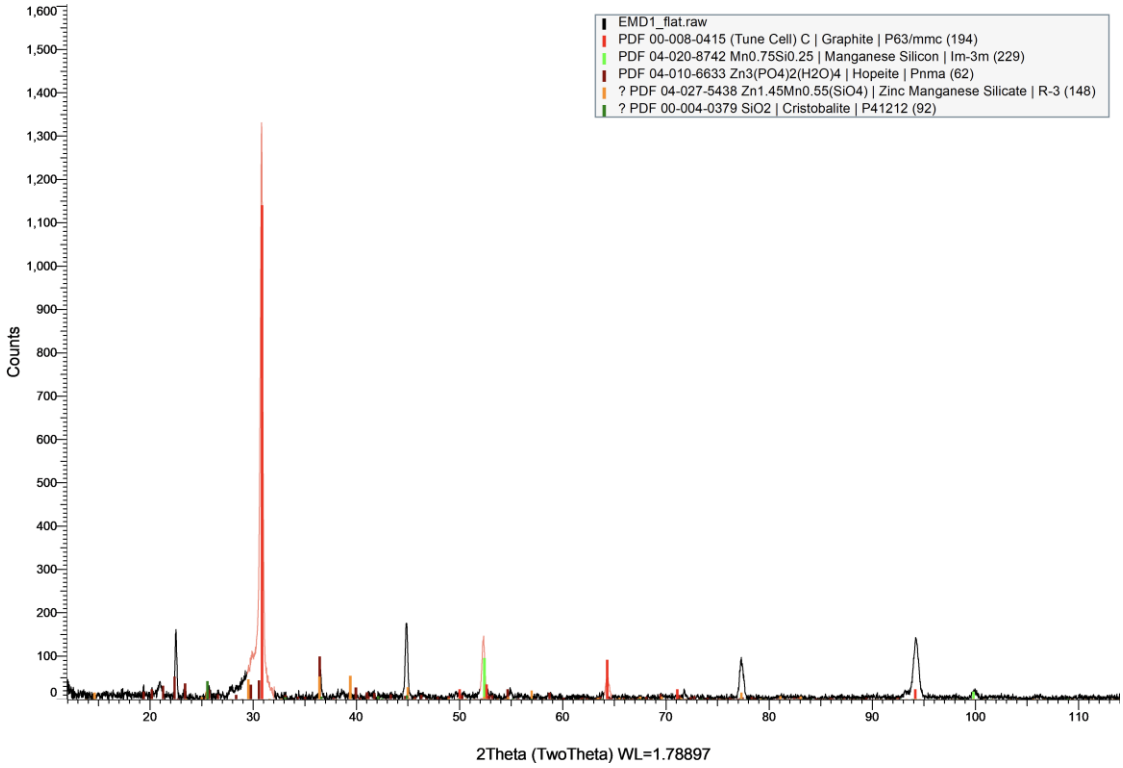

A-7 EMD-1 cathode collected after cycled in buffered electrolyte. Attempted analysis has been conducted.

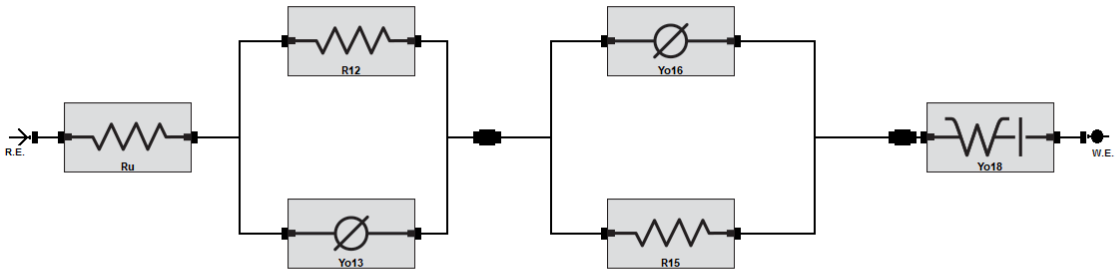

A-8 Equivalent circuit diagram used for EIS analysis, the circuit diagram is used for mere comparison, not used for consolidation purposes. Further development of equivalent circuit diagrams is required for interpretation.